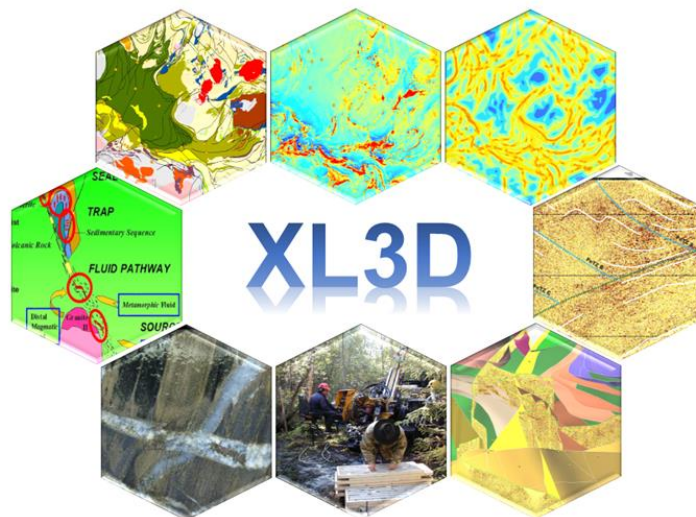


EXPLORATION LAPLAND 3D (XL3D) – AN INTEGRATIVE GEOMODELING WORKFLOW TO SUPPORT EXPLORATION



Niiranen T., Heinonen S., Karinen T., Lahti I., Leväniemi H., Madetoja J.,
Nykänen V.



European Union
European Regional
Development Fund

Leverage from
the EU
2014–2020

30.9.2020

GEOLOGICAL SURVEY OF FINLAND

DOCUMENTATION PAGE

Date / Dnro

<p>Authors Tero Niiranen, Suvi Heinonen, Tuomo Karinen, Ilkka Lahti, Hanna Leväniemi, Jaakko Madetoja, Vesa Nykänen</p>	<p>Type of report Open File Work Report</p>
	<p>Commission by Business Finland EAKR, Agnico-Eagle Finland Oy, Anglo American Sakatti Mining Oy, Astrock Oy, Aurion Resources Oy, Boliden FinnEx Oy, Geovisor Oy, GTK, Magnus Minerals Oy, Palsatech Oy, and Rupert Finland Oy</p>
<p>Title of report Exploration Lapland 3D (XL3D) – An integrative geomodeling workflow to support exploration</p>	
<p>Abstract Exploration Lapland 3D (XL3D) project generated a scalable workflow for data mining and data integration with emphasis on extracting the critical parameters of different mineral systems. The aim was to improve the efficiency of data handling and geomodelling in situations where vast data sets of various types are available. The XL3D project tested the workflow in Sodankylä area which covers the eastern part of the Paleoproterozoic Central Lapland Greenstone belt. The study area is currently under active mineral exploration and is considered highly prospective for new deposits.</p> <p>The generated workflow starts with data compilation, quality assessment and subsequent first pass data processing. Data processing includes data interpolation, the interpretation of seismic data, and generation of 1-3D unconstrained geophysical inversion models. After these phases the data is clustered using the Self Organized Maps (SOM) method and an initial 3D geomodel is generated using the 1st phase processed and clustered data sets. The initial 3D geomodel is used in the next phase as a constraint in generating geophysical inversion models. Both the geomodel and constrained geophysical models are adjusted iteratively until the final model provides a holistic representation of the available data sets. In the final step the critical parameters for the relevant mineral system are extracted from the models and used in prospectivity modeling together with the processed data and data clusters generated in the previous steps. With sufficient data the clustering and prospectivity modeling can also be done in 3D.</p> <p>The goal of the XL3D project was to utilize the workflow in extracting key exploration parameters for orogenic gold and magmatic Ni-Cu-PGE mineral systems from the data sets. The parameters are used in generating updated prospectivity models for these deposit types. High resolution low altitude airborne geophysics, regional gravity data, high resolution reflection seismic data, audiomagnetotelluric data, regional till geochemistry, petrophysics, and bedrock observation data comprise the data sets used in the work. Final 3D geomodels consist of a broader model covering the whole study area and a sub-model whereby the iterative constrained modeling was tested.</p> <p>The geological models generated outline the structural framework of the study area including several significant thrusts and faults, 3D topology of the main lithostratigraphic units and intrusives. Based on the model, the deformation features of the study area are controlled by thrust tectonics that took place in multiple phases. The tectonic zones acted as pathways to the hydrothermal fluids related to the formation of the orogenic gold deposits and as such they are gold potential. Some of the thrusts were very likely initially generated as extensional rift zones and as such were pathways for the primitive magmas related to the magmatic Ni-Cu-PGE deposits. The prospectivity maps generated outline relatively well the known orogenic gold and Ni-Cu-PGE deposits and occurrences. In addition, several highly prospective orogenic gold and Ni-Cu-PGE domains are highlighted by the new prospectivity maps including areas where previous exploration activity has been relatively low.</p> <p>Based on the work the presented workflow works in different scales and areas with different data density. The workflow requires input from a number of experts from different fields of geoscience. Active discussions between the experts throughout the process is required for successful result.</p>	

30.9.2020

Keywords Geomodelling, Reflection seismics, Audiomagnetotellurics, Potential fields, Inversion modeling, Self Organized maps, Prospectivity modeling, Central Lapland Greenstone belt, Orogenic gold, Magmatic Ni-Cu			
Geographical area Sodankylä and Kittilä, northern Finland			
Map sheet UTM U44, U52, V43, V51			
Other information EURA2014 Project code A73339			
Report serial Open File Work Report		Archive code 47/2020	
Total pages 85	Language English	Price -	Confidentiality Open access
Unit and section Mineral Economy Solutions		Project code 50403-301002	
Signature/name Vesa Nykänen Accountable Project Leader		Signature/name Tero Niiranen Project Manager	

Contents

Documentation pages

1	Introduction	1
2	Overview of the geology and mineral deposits of the XL3D study area	2
2.1	Sedimentation and magmatism in the project area	5
2.2	Deformation and metamorphism	7
2.3	Mineral deposits and occurrences	8
2.3.1	Koitelainen	8
2.3.2	Kevitsa	9
2.3.3	Sakatti	9
2.3.4	Suurikuusikko	10
2.3.5	Pahtavaara	11
2.3.6	Occurrences along the Sirkka Thrust Zone	11
3	data	11
3.1	Regional potential fields and electromagnetic data	11
3.1.1	Potential field datasets	11
3.1.2	Airborne electromagnetic (AEM) data	14
3.1.3	Audiomagnetotelluric data	14
3.1.4	Petrophysical data	15
3.2	Reflection seismic data	16
3.3	Regional geological and geochemical data	24
4	Workflow	25
4.1	General XL3D workflow	25
4.2	Self-organizing maps	27
4.2.1	SOM process	27
4.2.2	SOM results	29
4.3	Potential field inversions	33
4.3.1	Inversion methodology	33
4.3.2	Linking geology to petrophysics	35
4.3.3	Inversions and results	36
4.4	AMT inversions	52
4.5	3D Geomodeling	53

30.9.2020

4.6	Prospectivity modeling	54
4.6.1	Orogenic gold prospectivity model	56
4.6.2	Magmatic Ni–Cu prospectivity model	62
5	Results	66
5.1	3D geological models	66
5.1.1	Modeled elements	66
5.1.2	N–S-trending thrust zones	69
5.1.3	E–W-trending thrust zones	70
5.1.4	NE–SW-trending shear zones	72
5.1.5	The Nuttio thrust system	72
5.1.6	Discussion	73
5.2	Prospectivity models	74
6	Discussion and conclusions	76
6.1	Implications for regional geology and ore potential	78
7	Acknowledgements	79
8	References	80

1 INTRODUCTION

The overall goal of the Exploration Lapland 3D (XL3D) project is to increase the probability of finding new mineral deposits in the future and create new jobs in Lapland. To achieve this goal, the project has developed a scalable workflow for the mineral exploration-related data mining and data integration procedure. Vast digital geoscientific datasets exist in districts with a long history of geological research and exploration. The exploration and mining industry uses these datasets to define the locations of mineral deposits in many ways. Large and constantly accumulating datasets necessitate the development of new, more efficient data mining and modeling techniques. The XL3D project has provided solutions for these problems. We have conducted research on the integration and modeling of digital geoscientific data aiming to identify signals and vectors indicating mineral systems from these vast datasets.

This type of work requires a team of various experts, including geologists, geophysicists, and data analysts. The final outcomes of this project will be helpful for enterprises operating within the mineral exploration business, not only within the Europe's most active mineral exploration terrain in Finnish Lapland, but in the global mineral exploration business. The concept provided by the XL3D project is based on the integration and modeling of all the existing digital and deep-penetrating geoscientific exploration data. The data used in this project include regional potential fields and electromagnetic data, reflection seismic data, regional geological data, till geochemical data, and their derivatives. These data were explored using a data mining technique called self-organizing maps or SOMs (Kohonen 2001) and used to conduct prospectivity modeling (Bonham-Carter 1994) in order to produce an assessment of the potential for orogenic gold deposits and Ni–Cu deposits in the project study area within the Central Lapland Greenstone Belt. In addition, a geological 3D model was constructed using the available data. The results of the project are all publicly available for industry, SMEs, and academia.

In this report, we first describe in detail the geology and mineral deposits of the study area, the Central Lapland Greenstone Belt. We then provide a detailed overview of the datasets used in this project, starting with the regional potential fields and electromagnetic data, followed by the reflection seismic data, and finally a description of the geological datasets. The core of the report consists of elaborations of the key elements of the workflow, which is the main outcome of the project. This includes the data mining method of self-organizing maps, geophysical inversion modeling techniques, geological 3D modeling, and finally prospectivity modeling, which integrates all the information into a predictive model that delineates the most favorable areas for orogenic gold and Ni–Cu exploration within the study area. Finally, we discuss the best practices, the strengths and limitations of the workflow, and how it could be implemented in regional geological interpretations or considered in future mineral exploration.

This project was funded by the Business Finland ERDF Sustainable Growth and Jobs 2014–2020 program and also by private companies, including AA Sakatti Mining Oy, Agnico Eagle Finland Oy,

Boliden Finnex Oy, Aurion Resources Oy, Rupert Finland Oy, Magnus Minerals Oy, Astrock Oy, Geovisor Oy, and Palsatech Oy. The total funding received was €504 00, of which Business Finland covered 88% and the private companies 12%. The project was carried out solely by the Geological Survey of Finland. The team was composed of economic geologists, geophysicists, and data analysts. The project duration was from January 1st, 2018 to June 30th, 2020.

2 OVERVIEW OF THE GEOLOGY AND MINERAL DEPOSITS OF THE XL3D STUDY AREA

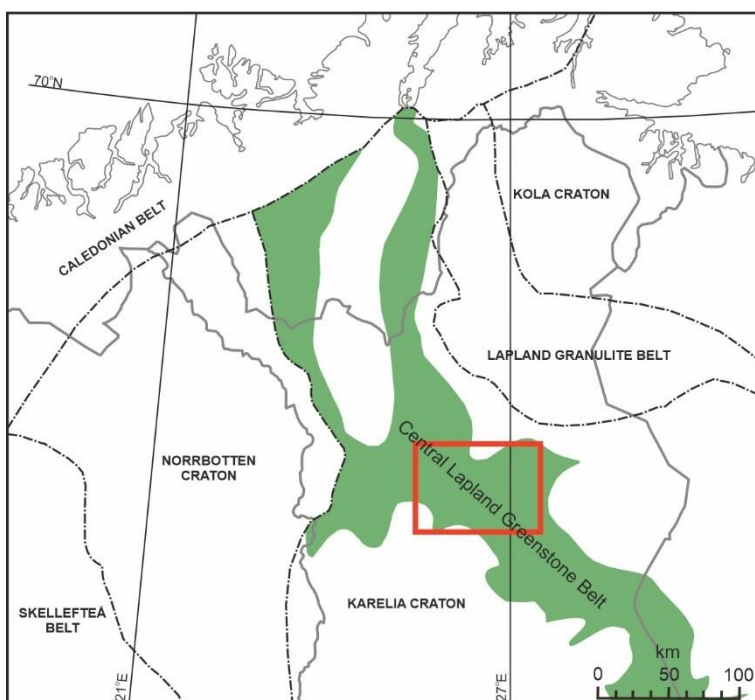


Figure 2.1. Location of the study area in the Central Lapland Greenstone Belt.

The Central Lapland Greenstone Belt (CLGB) in the Fennoscandian Shield area is a part of the Paleoproterozoic schist and greenstone belts that extend 450 km from northern Norway through Finnish Lapland to the western part of Russian Karelia (Fig. 2.1). The geological evolution of these belts initiated at around 2.5 Ga by rift-related sedimentation and magmatism, but during the Lapland–Kola (1.94–1.86 Ga) and Svecofennian (1.92–1.79 Ga) orogenies, the evolution turned into compressional tectonics and was from then on accompanied by emplacements of syn- and post-orogenic felsic igneous rocks (Hanski & Huhma 2005; Lahtinen et al. 2018). A recent study of the CLGB (Köykkä et al. 2019) interpreted the depositional systems, tectonic settings, and main lithologies of the different metamorphic belts in northern Fennoscandia. The study divided the Paleoproterozoic basin evolution

of northern Finland into five stages: (1) initial rifting/early syn-rift, (2) syn-rift, (3) syn-rift to early post-rift at 2.5–2.1 Ga, (4) a passive margin (post-rift) at 1.94–1.92 Ga, and 5) a foreland basin system from 1.94–1.92 to 1.88 Ga.

The rocks of the project area span in age almost the whole evolutionary and deformation history of the CLGB. A general lithological map of the project area is presented in Figure 2.2. The lithostratigraphic units of the project area are shown in Figure 2.3, which also illustrates the depositional systems and tectonic settings according to Köykkä et al. (2019). The use of the prefix 'meta-' is omitted for simplicity in this report when discussing the different lithologies, although the rocks of the study area, except for the youngest granites, have undergone metamorphism.

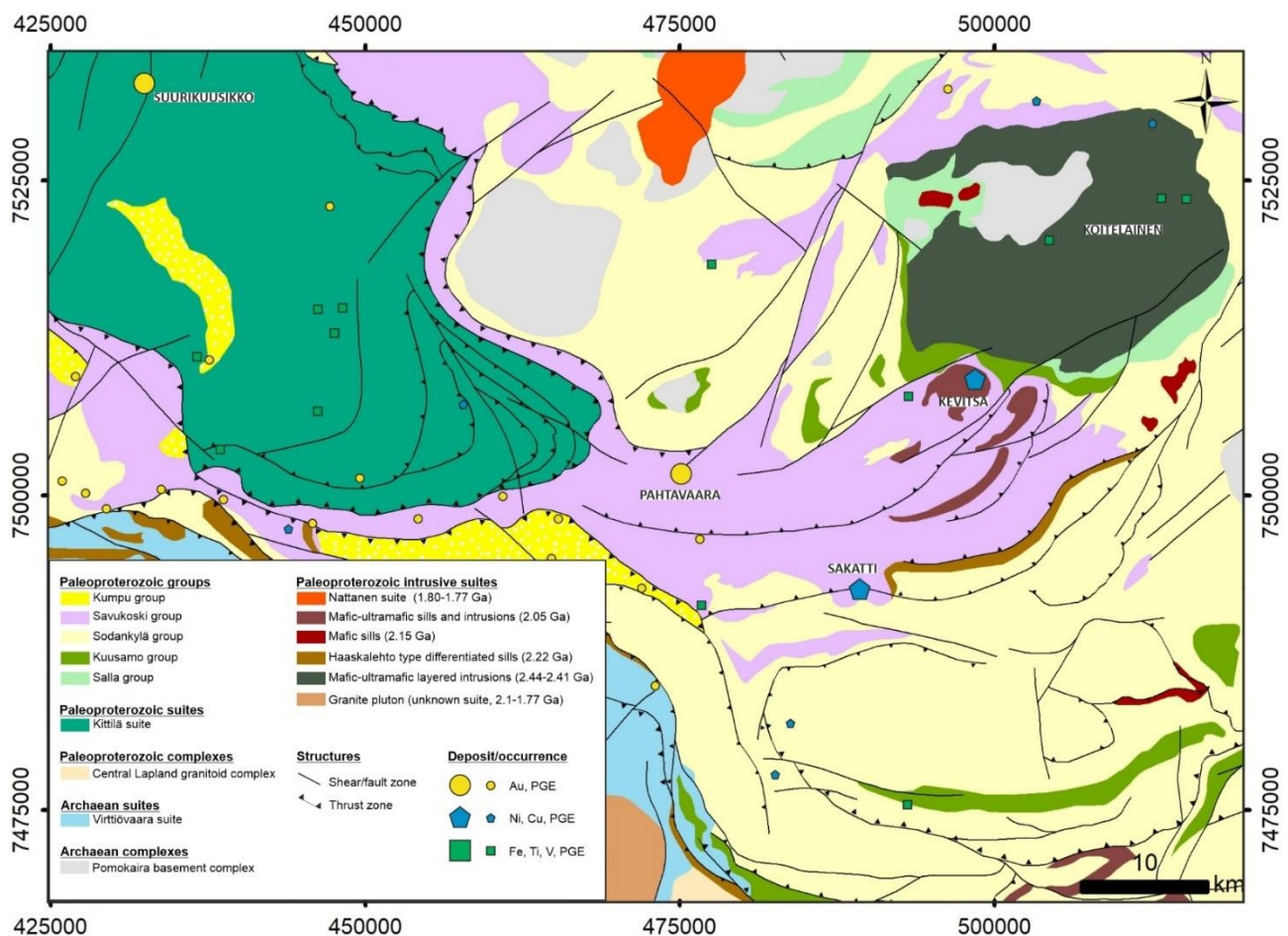


Figure 2.2. Location of the study area on a simplified geological map modified after the Bedrock of Finland – DigiKP. The location of the mineralized sites and their classification is based on the Mineral Deposit and Exploration service of GTK.

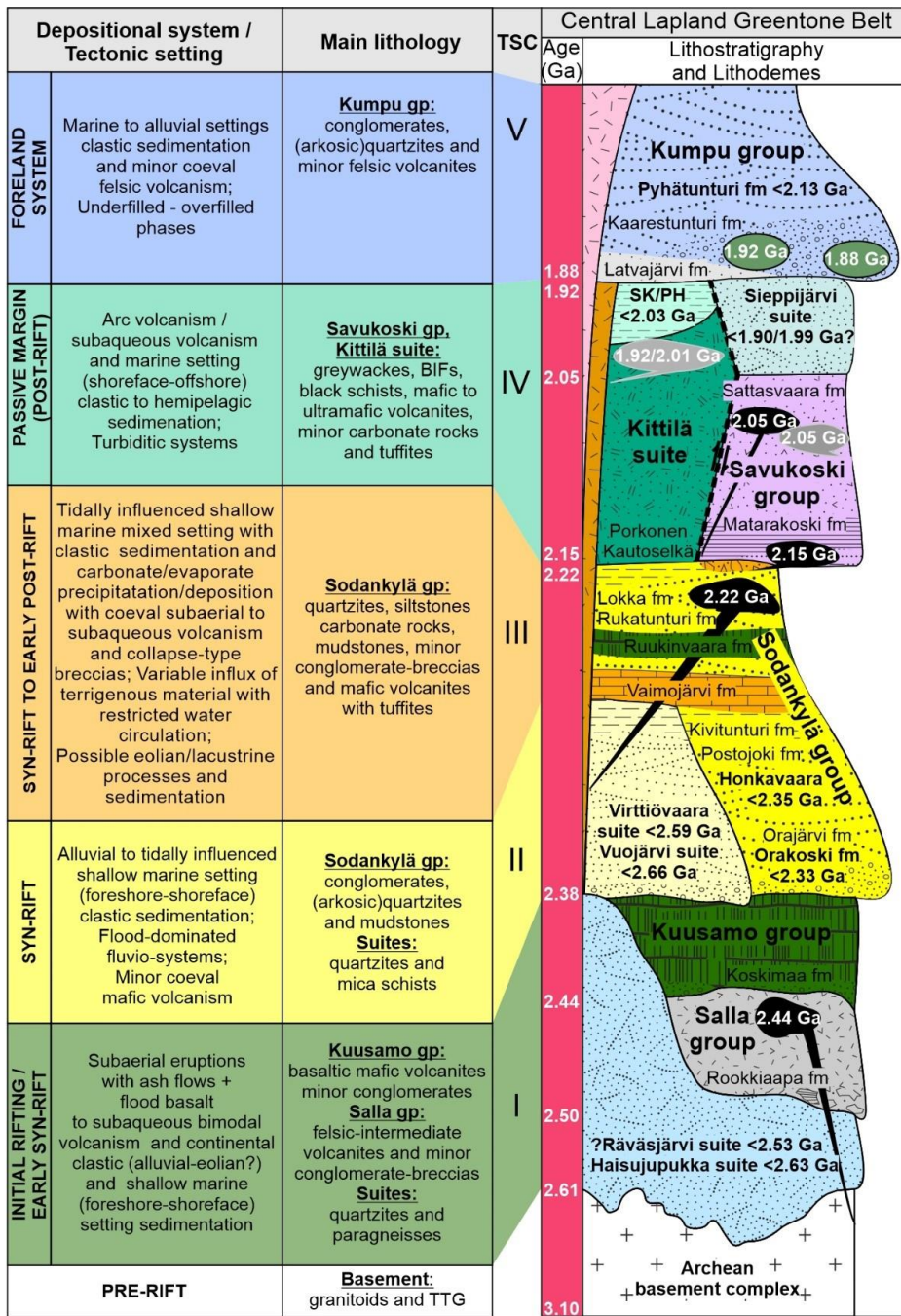


Figure 2.3. The stratigraphic column of the CLGB with the depositional systems, tectonic settings, and main lithologies (modified after Köykkä et al. 2019).

2.1 Sedimentation and magmatism in the project area

Tonalitic and granodioritic gneisses of the Archean Pomokaira basement complex comprise the oldest rocks, which in the study area are best exposed in round, dome-shaped structures in the Soasjoki, Möykkelmä, and Tojottamanselkä areas. A reddish tonalitic gneiss from Tojottamanselkä was dated at 3.1 Ga (Manninen et al. 2001; Hanski & Huhma 2005).

In the classification of Köykkä et al. (2019), the initial rifting/early syn-rift phase includes early sedimentation followed by volcanites of bimodal magmatism. The sediments belong to the Räväsjärvi and Haisujupukka suites, which are both located in the Central Lapland Granitoid Complex (CLGC) area. These minor migmatitic supracrustal rock units (mica/arkose gneisses, quartzites and minor amphibolites) display a similar maximum age to the Virttiövaara and Vuojärvi suites, which have been assigned according to their lithological features to the Sodankylä group representing the syn-rift stage (Köykkä et al. 2019).

The bimodal magmatism of the initial rifting/early syn-rift phase is represented by the 2.52–2.44 Ga Salla and Kuusamo groups. In the Tojottamanselkä area, the Salla group was deposited on the Archean basement. In the Tojottamanselkä area, the Salla volcanic rocks occur as a succession that begins with basal volcanoclastic conglomerate/breccia with a variety of rock clasts, including cobbles of Archean gneisses. In the Peurasuvanto area, the Salla group volcanic rocks are represented by feldspathic gneisses deposited directly on the Archean basement. In the Koitelainen intrusion area, the Salla group rocks consist of a thin succession of andesitic to dacitic lava flows and rhyolitic pyroclastic rocks deposited on the roof contact of the Koitelainen layered intrusion complex (Peltonen et al. 1988; Manninen et al. 2001). The rocks of the Kuusamo group are best exposed in the Möykkelmä area, where they occur directly on the Archean basement gneiss and form a 250-m-thick unit of sheets of amygdaloidal komatiitic basalts, basalts, basaltic andesites, and andesites (Räsänen et al. 1989; Hanski & Huhma 2005).

The Salla and Kuusamo groups display relatively clear signatures of interaction with sialic crust and they have therefore been attributed to the intracratonic rifting that produced some of the largest layered mafic ultramafic intrusions in northern Finland, such as the Koitelainen intrusion (2.44–2.41 Ga; Mutanen & Huhma 2001; Huhma et al. 2018). Diamond drilling at the Koitelainen intrusion has revealed that the intrusion is a sheet-like antiformal-shaped body. This suggests that the magma chamber of the intrusion crystallized along a lateral continuity. The maximum stratigraphic thickness of the Koitelainen intrusion is almost 3 km, and it is capped by a layer of granophyre (up to 350 m thick), which is geochemically similar to the felsic volcanites of the Salla group (Mutanen 1997; Hanski & Huhma 2005).

The sediments and minor volcanites of the Sodankylä group cover large areas in the CLGB area. In the classification scheme of Köykkä et al. (2019), the group represents a depositional history spanning from the syn-rift to syn-rift to early post-rift phases. The Sodankylä group lithologies were deposited in a

deepening depositional basin of a craton or a craton margin and either on Archean basement or on volcanic rocks of the Salla and Kuusamo groups. The sedimentary rocks of the Sodankylä group consist of arkositic quartzites. Herringbone and mud crack textures indicate that the depositional environment was at least locally tidal and that the rift basin was considerably widened after the cessation of volcanism related to the Salla and Kuusamo groups (Lehtonen et al. 1998; Hanski & Huhma 2005). In addition to clastic sediments, the Sodankylä group includes minor carbonaceous sedimentary rocks and amygdaloidal tholeiitic basalts and basaltic andesites. The volcanites are likely coeval with the 2.22 Ga differentiated ultramafic–mafic sills referred to as Haaskalehto type (Rastas et al. 2001; Huhma et al. 2018), thus giving the minimum depositional age for the lower and middle part of the Sodankylä group. A conspicuous feature in the sediments of the Sodankylä group rocks is their high albitization and carbonatization. This is observed in the upper part of the group, in which the alteration appears to be spatially related to Haaskalehto-type sills (Lehtonen et al. 1998).

In the classification of Köykkä et al. (2019), the deposition of the Savukoski group lithologies begins in the passive margin (post-rift) phase. Black schists and greywackes comprise the lower part of the group, and although these rocks represent a new group in stratigraphy, they form a continuum with the sedimentary sequence of the Sodankylä group (Lehtonen et al. 1998; Köykkä et al. 2019). A minimum depositional age of 2.05 Ga for the sedimentary lower part of the Savukoski group is indicated by the cross-cutting diabase dykes (Huhma et al. 2018). This age also marks the stage of extensive magmatism of the komatiite–picrite association, which has been attributed to a large-scale plume event that initiated at 2.15–2.10 Ga and was followed by continental break-up at 2.10–2.05 Ga. In the study area, komatiites predominate in the southern part (Sattasvaara-Kersilö areas), whilst picrites predominate in the northern part (Sotkaselkä) (Hanski & Huhma 2005, Vuollo & Huhma 2005; Huhma et al. 2018).

The lower part of the Kittilä suite represents the syn-rift to early post-rift phase and the upper part represents the passive margin stage in the scheme of Köykkä et al. (2019). Recent 3D modeling indicates that the suite extends down to a depth of 9 km (Niiranen 2015). The suite is considered allochthonous. The southern margin of the suite is bounded by the E–W-trending Sirkka line and the eastern margin is thrust on the basement gneisses and its autochthonous supracrustal part (Lehtonen et al. 1998; Hanski & Huhma 2005). Another feature that may indicate an allochthonous origin is the occurrence of serpentinitic bodies, which are found near the eastern contact of the suite. These bodies belong to the Nuttio suite, which Hanski (1997) interpreted as a piece of the mantle part of an ophiolite.

Two volcanic formations comprise the main part of the suite. The stratigraphically lower one, the Kautoselkä formation, has geochemical characteristics of passive margin tholeiites, whilst the volcanites of the upper Vesmajärvi formation have geochemical affinity with oceanic basalts. These formations sandwich the Porkonen formation, which consists of graphitic tuffs, tuffites, carbonate rocks, and oxide facies banded iron formations (Lehtonen et al. 1998; Hanski & Huhma 2005). The upper part of the Kittilä suite consists of two lithodemic units, the Seurukarkea and Pyhajarvi

lithodemes (SK and PH in Fig. 2.3), of which the former is composed of graphite-bearing phyllites, mica schists, and sericite quartzites, whereas the latter is mostly composed of graphite-bearing parashists. The stratigraphic position of these lithodemes straddles the boundary between the Kittilä suite and Rovaniemi supersuite (represented by the Sieppijärvi suite in the CLGB area), with a maximum depositional age of ca. ≤ 2.03 Ga (Köykkä et al. 2019). The maximum age for the Rovaniemi supersuite marine depositional system is between 1.99 and 1.97 Ga, and it is considered to have a partly bimodal volcanic and epiclastic origin (Hanski et al. 2005; Köykkä et al. 2019).

The Kumpu group represents the foreland system. It is the youngest supracrustal unit in the CLGB, predominantly consisting of clastic sedimentary rocks that display features of alluvial depositional environments (Köykkä et al. 2019). Minor amounts of intermediate to felsic volcanites occur in the unit in the western part of the CLGB (Hanski & Huhma 2005). The minimum age of this group is defined by a U–Pb zircon age of 1.89 Ga from a monzonitic conglomerate cobble (Hanski et al. 2005).

Most of the felsic plutonic rocks in northern Finland belong into the following main broad groups: syn-orogenic (1.89–1.86 Ga), late orogenic (1.84–1.77 Ga), and post-orogenic (1.80–1.77 Ga) (Hanski et al. 2001; Nironen 2005; Heilimo et al. 2009). The Tenniövaara stock, located in the northern part of the study area, belongs to the post-orogenic group, as it is one of the Nattanen suite intrusions.

2.2 Deformation and metamorphism

The geological evolution of the CLGB culminated during the multi-stage deformation and metamorphism related to Svecofennian orogenic events at 1.92–1.79 Ga. According to earlier interpretations by Ward et al. (1989), Lehtonen et al. (1998), Väisänen (2002), Hölttä et al. (2007), and Patison (2007), the deformation history of the CLGB included earlier thrust-dominated ductile deformation phases, which were followed by brittle stages. For example, Väisänen (2002) and Hölttä et al. (2007) recognized three main deformation stages, of which the two earliest were regarded as a superimposed D_{1-2} stage. Both of the stages were attributed to nearly orthogonal thrusting that took place at the southern and northeastern margins of the CLGB. The northward-directed thrusting at the southern margin was linked to the generation of the south-dipping Sirkka (STZ) and Venejoki thrust zones (VTZ). In the northeastern margin of the CLGB, the S–SW-vergent thrusting was attributed to collision of the Karelian and Kola cratons and thrusting of the Lapland Granulite Belt to the SW. The D_3 stage was linked to refolding of the earlier structures with highly variable directions. In contrast to the earlier stages, the D_3 stage was attributed to most of the strike-slip shear zones in the CLGB, of which the N- to NE-striking shear zones were noted to dominate.

The most recent interpretations of the tectonic evolution in the northern part of the Fennoscandian shield have been presented by Lahtinen et al. (2018) and Sayab et al. (2019), who identified five deformation stages in the area. The stages are nearly orthogonal to each other and are divided into

pre-1.88–1.87 Ga (D_1 and D_2) and 1.87–1.76 Ga (D_3 , D_4 , and D_5) periods. The earliest deformation stage is characterized by west-vergent thrusting and stacking at ca. 1.92 Ga. This was followed by a period of N–S-trending shortening at 1.90–1.89 Ga in the D_2 stage, which is comparable to the superimposed D_{1-2} of Väisänen (2002) and Hölttä et al. (2007). During this stage, most of the regional strain was taken up along the southern and northern margins of the CLGB. The D_3 stage at 1.88–1.87 Ga was characterized by NE–SW-directed shortening, which caused a dextral strike-slip regime along the N–S-trending older thrust planes, such as the Kiistala Shear Zone (KSZ) hosting the Suurikuusikko Au deposit. By the D_4 stage at 1.84–1.81 Ga, the stress field remained near-orthogonal but it had changed to a NW–SE direction, and the kinematics in the pre-existing D_3 shear zones therefore turned opposite. The D_5 stage at ca 1.77–1.76 Ga is characterized by broadly E–W-directed shortening.

The most comprehensive metamorphic study concerning the CLGB is that of Hölttä et al. (2007), who observed that the peak metamorphic conditions in the Kittilä suite reached mid-greenschist facies, and the metamorphic grade is higher in its surroundings. In the south and west of the Kittilä suite, the peak metamorphic grade reached mid- to upper-amphibolite facies, but towards the NE, the grade increases considerably, from amphibole to granulite facies near and in the Lapland granulite complex.

2.3 Mineral deposits and occurrences

The project area and its vicinity includes several mineralized occurrences and smaller amounts of deposits (Fig. 2.2). The most prominent deposits are briefly described below.

2.3.1 Koitelainen

The 2.44 Ga Koitelainen layered intrusion hosts a number of layers and zones enriched in various metals, including two PGE-bearing chromitite occurrences (LC, UC), V-PGE-enriched magnetite gabbro, and some minor PGE-enriched occurrences, which are described in detail in the reports of Mutanen (1976, 1979, 1989). The intrusion is 26 × 29 km in its areal extent and it has a maximum stratigraphic thickness of ca. 3.2 km. The footwall rocks are exposed in the anticlinal area in the middle of the intrusion, whereas the upper parts of the intrusion are exposed at its outer margins. The intrusion is subhorizontal, with a 0–10° dip away from the central dome of the footwall Archean gneisses (Mutanen 1997; Mutanen & Huhma 2001; Huhma et al. 2018). According to Mutanen (1997), the intrusion was formed from a single batch of mafic magma, with a low TiO_2 basaltic parental magma composition. Regarding the classification of Köykkä et al. (2019), the intrusion is a product of the bimodal magmatism of the initial rifting/early syn-rift phase at 2.52–2.44 Ga. The vanadium resources of the Koitelainen intrusions have recently been estimated by Pursuit Minerals Ltd (2019). The current inferred resources are 116.4 Mt of oxide ore containing 5.8 Mt of vanadiferous oxide @ 2.3 wt% V_2O_5 (1.3 wt% V) in concentrate. This estimate has been calculated at cut-off values of 5.0% mass recovery and 0.5 wt% V of concentrate.

2.3.2 Kevitsa

The Kevitsa deposit was discovered in 1987 by GTK (Mutanen 1997). The disseminated Ni–Cu–PGE sulfide mineralization is hosted by the Kevitsa intrusion, which represents the same product of a large-scale plume event to which the magmatism of the Savukoski group has been attributed. Zircons from the intrusion have been dated by the U–Pb method at 2057 ± 5 Ma (Mutanen & Huhma 2001). The intrusion is funnel shaped, 4×4 km in its horizontal extent, and it consists of ultramafic, gabbroic, and granophyric parts with locally developed igneous layering. The mineralization is hosted by the ultramafic part, located in the NE part of the intrusion. The mineralization extends from the surface down to a depth of 400 m and is irregular in its grade and shape. It includes at least two distinct ore types: regular ore and Ni–PGE ore. The former constitutes ~95% of the resource and contains 2–6 vol% sulfides (pyrrhotite, pentlandite, and chalcopyrite), with Ni and Cu contents of 0.30 and 0.41 wt%, respectively. In addition, the intrusion contains so-called “false ore” (pyrrhotite-rich with minor pentlandite and chalcopyrite), which has low Ni tenors of 2–3% (Mutanen 1997; Santaguida et al. 2015).

The pre-mining resource of the Kevitsa deposit was 272 Mt @ 0.30 wt% Ni, 0.40 wt% Cu, 0.015 wt% Co, 0.19 g/t Pt, 0.24 g/t Pd, and 0.11 g/t Au (Eilu 2015). Mining in the deposit commenced in 2012 and presently, after 8 years of mining, the current proven and probable reserves sum to 140.3 Mt @ 0.24 wt% Ni, 0.32 wt% Cu, 0.010 wt% Co, 0.14 g/t Pt, 0.22 g/t Pd, and 0.11 g/t Au. In addition, the deposit includes 317.4 Mt of mineral resources (including measured, indicated, and inferred) with a similar grade of the ore (Boliden AB 2020).

2.3.3 Sakatti

The Sakatti Ni–Cu–PGE-deposit was discovered during a regional exploration project by Anglo American in 2009. Currently, three separate mineralized ultramafic bodies are known to occur in the area: the main body, NE body, and SW body. The bodies are irregular in shape and generally plunge steeply north and northwest. For example, the main body subcrops in a ca. 250×500 m area and forms a tubular shaped 200–400-m-wide, NW-plunging serpentinite body with a known depth extent of approximately 1200 m. The deposit is surrounded by metapelitic rocks of the lower part of the Savukoski group and quartzites of the Sodankylä group. However, the immediate wall rocks of the mineralized ultramafic bodies are not easily classified into either of the aforementioned groups. Most of the immediate wall rocks, of which the most prominent one is a fine-grained aphanitic unit, are assumed to be volcanogenic in origin (Brownscombe et al. 2015).

The parental magma composition of the Sakatti deposit has been estimated to be komatiitic, and the deposit is therefore probably of the same age as the Kevitsa intrusion. There are at least two alternative petrogenetic models to explain the genesis of the deposit. It has been attributed to a shallow-level conduit- or tube-like intrusion (chonolith) or a cumulate portion of picritic-komatiitic lava flows forming the aphanitic rocks surrounding the mineralized serpentinites (Brownscombe et al. 2015).

The mineralization consists of disseminated sulfides, sulfide veins, and semi-massive to massive sulfides. The chalcopyrite-dominated disseminated mineralization predominantly occurs in the serpenitic rocks of the main body, whereas the other types are also found extending into fine-grained aphanitic rocks in the footwall and hanging wall in all the mineralized bodies.

The Cu content of the disseminated mineralization increases towards the upper part of the mineralization. In DDH 08MOS8007, typical grades along a 62.70-m intersection of this mineralization are 0.51 wt% Cu, 0.23 wt% Ni, 0.22 g/t Pd, 0.44 g/t Pt (the Pt/Pd value is 2), and 0.13 g/t Au. The sulfide veins and massive sulfides predominantly occur in the shallow and central parts of the mineralized bodies. Massive sulfides occur as stacked lenses in the central part of the bodies, extending into the aphanitic sidewall. The lenses are up to 25 m thick in the central part, thinning to 0.5 m towards the NW and SE. A 26.5-m interval of massive sulfides (DDH 11MOS8049) contained 3.69 wt% Cu, 4.16 wt% Ni, 0.18 wt% Co, 1.10 g/t Pt, 1.27 g/t Pd, and 0.24 g/t Au. The vein type in the main body has been interpreted to represent fractionated 5–20-cm-thick apophyses of the semi-massive to massive sulfides and they predominantly occur in the main body. The massive and veined sulfide mineralization shows a distinct fractionation in Ni–Cu values. This is observed between the mineralized bodies and along the plunge of the main body, in which the massive sulfides evolve up-plunge to become increasingly chalcopyrite-dominated (Coppard et al. 2013; Brownscombe et al. 2015). The mineral resources of Sakatti consist of indicated 3.5 Mt @ 3.45 wt% Cu, 2.47 wt% Ni, 0.11 wt% Co, 0.98 g/t Pt, 1.18 g/t Pd, and 0.33 g/t Au, accompanied by inferred resources of 40.9 Mt @ 1.77 wt% Cu, 0.83 wt% Ni and 1.37 g/t Pd+Pt+Au (Anglo American 2019).

2.3.4 Suurikuusikko

The Suurikuusikko gold deposit was discovered by GTK in 1986. In 2000–2001, a preliminary estimate of the combined inferred and indicated mineral resource of the deposit, calculated using a cut-off of 1 g/t Au, amounted to 8.3 Mt @ 6.1 g/t Au (Riddarhyttan Resources 2001). Construction of the mine in the deposit began in June 2006 (Agnico Eagle Mines Ltd), and the mine was named after the municipality of Kittilä. According to Agnico Eagle (2020), the present proven and probable reserves of the deposit sum to 4.096 Moz of gold (28.925 Mt @ 4.40 g/t Au). The additional mineral resources (including measured, indicated, and inferred resources) are 31.966 Mt @ 3.16 g/t Au (1.38 Moz Au).

The Suurikuusikko deposit is an orogenic gold deposit hosted by intensively metasomatized (carbonatization and albitization) tholeiitic mafic volcanic rocks of the Kittilä suite. Structurally, the mineralization is hosted by the sub-vertical to steeply east-dipping KSZ. Mineralized rocks related to the deposit have been found for about 4 km along the strike of the shear zone, and from the surface to a depth of over 1.5 km. Most of the gold in the deposit is refractory, predominantly occurring (73.2%) in the lattice of arsenopyrite and in smaller amounts (22.7%) in the lattice of pyrite. A minority (4.1%) of the gold occurs in micro-inclusions in sulfide grains. A Re–Os age of 1916 ± 19 Ma has been obtained from gold-bearing arsenopyrite (Wyche et al. 2015). This age allowed Sayab et al. (2019) to link the

Suurikuusikko deposit to the D₁ stage, in which a west-vergent thrust splay provided the primary structural controls on the localization of the deposit.

2.3.5 Pahtavaara

The Pahtavaara gold deposit was discovered in regional exploration by GTK in 1985. The deposit is hosted by an altered sequence of komatiitic rocks of the Savukoski group and is composed of a swarm of subparallel lodes, which plunge steeply to the W or WSW. The gold is mostly in a free native form, and occurs between silicate, carbonate, and barite grains. The mineralization is structurally controlled, and it was therefore originally classified as an orogenic deposit (Korkiakoski 1992). However, alternative genetic interpretations have been suggested (e.g. Patison et al. 2013), including that Pahtavaara represents an Au-rich VMS system.

Pahtavaara was intermittently mined between 1996 and 2014 by different companies. Currently, the deposit is maintained by Rupert Resources. Geological modeling utilizing over 500,000 m of drilling available for the deposit has indicated that the mineralization is located within an envelope up to 500 m in width and up to 1500 m in length, and it remains open at depth and along strike. The present inferred resource of the deposit is 4.6 Mt @ 3.2g/t Au (474 Koz), calculated using a 1.5g/t cut-off (Rupert Resources 2018).

2.3.6 Occurrences along the Sirkka Thrust Zone

More than 30 gold deposits and occurrences have been discovered in the proximity of the STZ and subsidiary faults branching from this south-dipping crustal-scale thrust zone. The majority of these have been classified as orogenic gold deposits (Eilu et al. 2007). Most of the known deposits and occurrences are hosted by altered Sodankylä group phyllites, mica schists, and mafic and ultramafic volcanic rocks. In a number of the known deposits and occurrences, base metals (Cu, Co, Ni) occur in elevated concentrations together with gold (e.g. Eilu et al. 2007). Mineralization is typically linked to quartz-carbonate alteration, which typically occurs as veins and breccia infill and hosts the gold and sulfides. Host rocks are commonly variably albitized prior to the main mineralization stage. The mineralization along the more than 100 km-striking STZ is clearly structurally controlled. In many of these occurrences, the mineralization was controlled by the intersection of two faults or a fault running along lithological units of different competences (Patison 2007; Eilu et al. 2007).

3 DATA

3.1 Regional potential fields and electromagnetic data

3.1.1 Potential field datasets

The potential field data in the study area consists of airborne total magnetic field intensity and regional ground gravity data.

The magnetic data are a combination of several survey areas in GTK's fixed-wing country-wide airborne mapping program concluded in the mid-2000s (Hautaniemi et al. 2005). The study area has been

surveyed roughly during two time periods: in the late 1970s and between the mid-1990s and mid-2000s (Table 3.1). The flight line spacing is 200 m, the flight direction either north–south or east–west, and the survey altitude 30–40 m.

Table 3.1. Flight area specifications. NS = north–south, EW = east–west, VCA = vertical-coaxial coils, VCP = vertical-coplanar coils. Fixed-wing aircraft: VKB = DC-3, KOG = Twin Otter.

Flight area	Year	Flight direction	Aircraft	Mean altitude (m)	Magnetometers	EM system (frequency domain)
Tanhua	1975	EW	VKB	31	Proton	VCA, 3220 Hz
Tepsa	1976	NS	VKB	32	Proton	VCA, 3220 Hz
Sodankylä	1977	NS	VKB	38	Proton	VCA, 3220 Hz
Kiistala2	1979	EW	VKB	38	Proton	VCA, 3220 Hz
Kiistala3	1979	EW	VKB	38	Proton	VCA, 3220 Hz
Kelujärvi	1987	NS	KOG	36	Proton	VCP, 3113 Hz
Peurasuvanto	1994	NS	KOG	34	Cesium	VCP, 3113 Hz
Kittilä_96	1996	NS	KOG	32	Cesium	VCP, 3125 / 14,368 Hz
Kumputunturi	1999	EW	KOG	34	Cesium	VCP, 3125 / 14,368 Hz
Vintilänkaira	2000	NS	KOG	31	Cesium	VCP, 3125 / 14,368 Hz
Pomokaira	2004	EW	KOG	31	Cesium	VCP, 3125 / 14,368 Hz

The gravity data originate from the ‘regional gravity register’ of GTK, which covers approximately 25% of the country with a varied spatial station density of 1–6 stations/km². The data represent the complete Bouguer anomaly, i.e. with topographic correction applied (S. Elo, pers. comm. 2009). The central part of the study area is covered with a station density of 3–4 stations/km², but the data are sparser in the east.

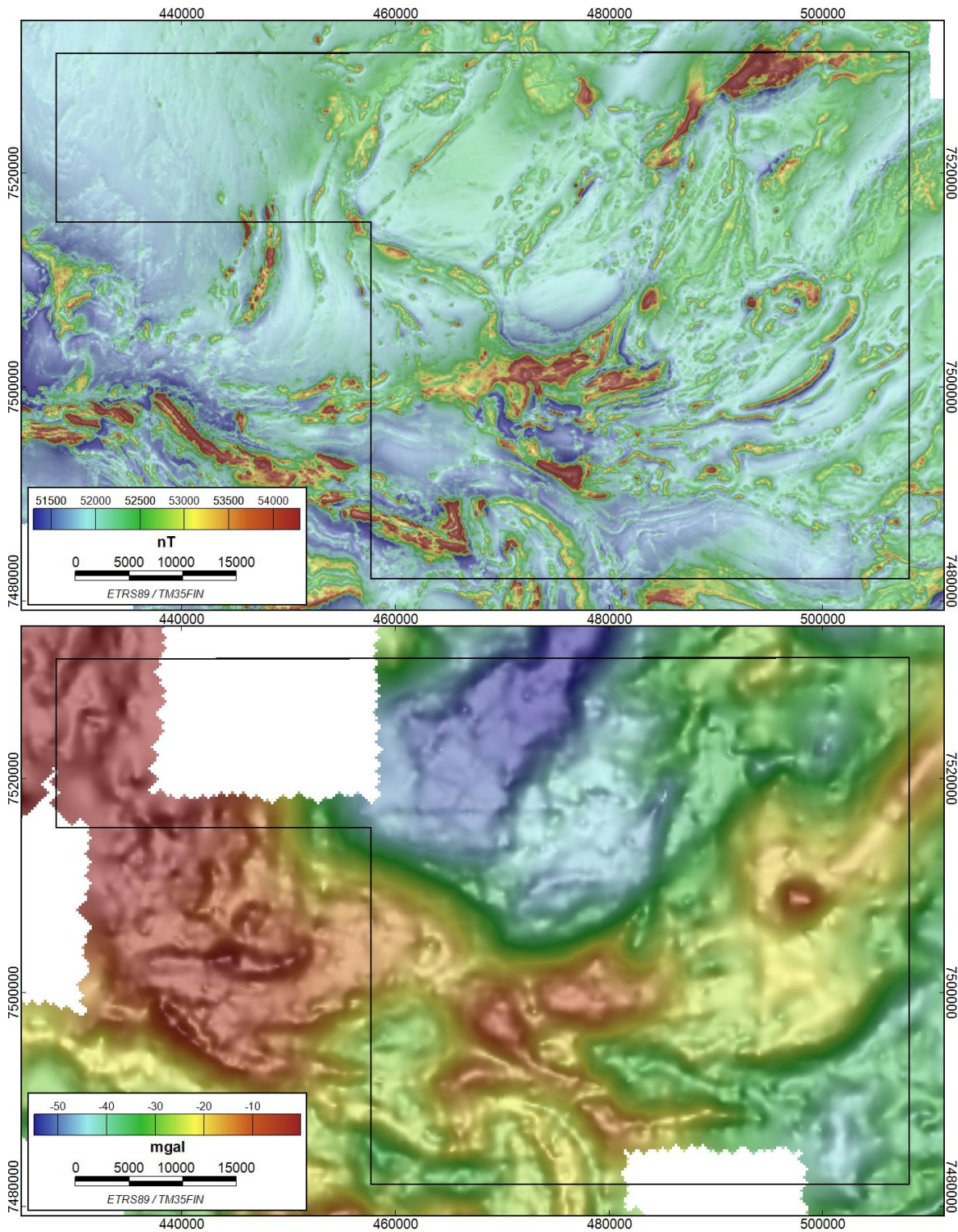


Figure 3.1. Top: airborne magnetic data (total field intensity reduced to pole, shaded with pseudogravity transformation). Bottom: regional gravity data (complete Bouguer anomaly, shaded with the magnitude of the horizontal gradient). The study area is outlined with a polygon.

3.1.2 Airborne electromagnetic (AEM) data

The airborne data include frequency-domain electromagnetic data measured with three different coil/frequency configurations (Table 3.1). The 3 kHz data were combined and manually re-leveled for the whole study area. The data consist of in-phase (real) and quadrature (imaginary) components (the former shown in Figure 3.2). The depth of investigation is generally <50 m.

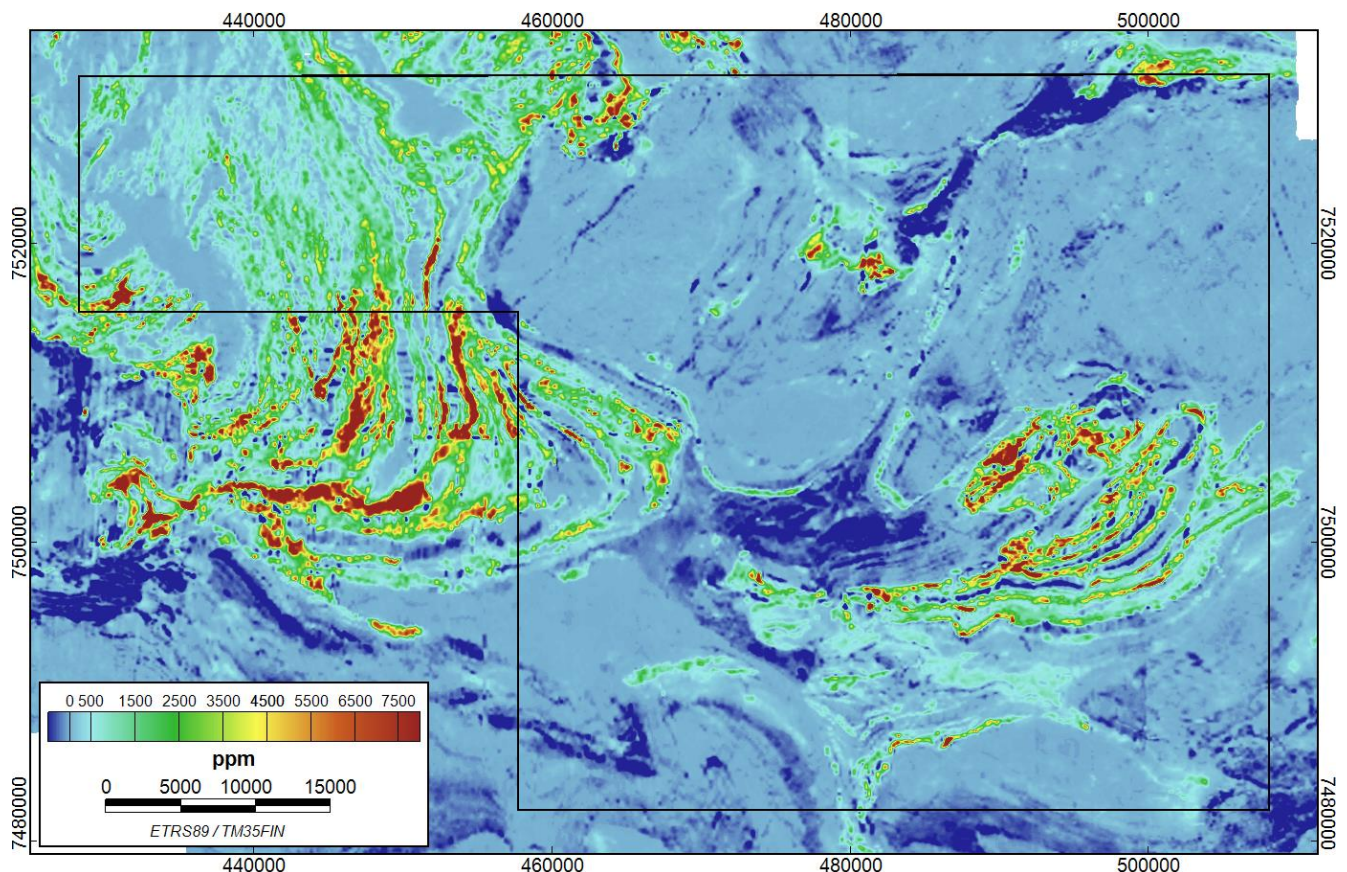


Figure 3.2. AEM 3 kHz in-phase data. High positive values imply good bedrock conductors and negative values resistive bedrock with a high magnetic susceptibility. The study area is outlined with a polygon.

3.1.3 Audiomagnetotelluric data

The audiomagnetotelluric (AMT) method images the electrical conductivity structure of the subsurface using the Earth's natural EM fields as a source (e.g. Berdichevsky and Dmitriev 2008). An AMT survey was carried out in 2017–2018 to study the electrical conductivity structure of the area. Altogether, 33 AMT soundings were carried out with a station spacing of 400 m to 4 km (Fig. 3.3). Metronix ADU-07e broadband electromagnetic receivers, MFS-07e induction coils, and EPF-06 (PbPb-Cl₂) electrodes were used in data acquisition. Electric dipole lengths of 60–90 m were used in the survey. One instrument was installed at a permanent location, providing a noise-free reference signal (H_x, H_y), and another instrument was used for AMT soundings (H_x, H_y, E_x, E_y). AMT impedance tensor data were processed using Mapros software (Friedrichs 2007). Figure 3.3(a) shows the location of AMT stations on the airborne EM map. Figure 3.3(b) displays an example of processed data.

Larger station spacing was used along profile 1 due to minor conductivity anomalies indicated by airborne EM data. In turn, the area of profile 2 is characterized by highly conductive elongated graphite-bearing rocks. EM anomalies of the conductive rocks are seen in airborne data from profile 2 (Fig. 3.3a). Therefore, shorter AMT station spacing was used in the area. AMT inversion results are presented in chapter 4.3.

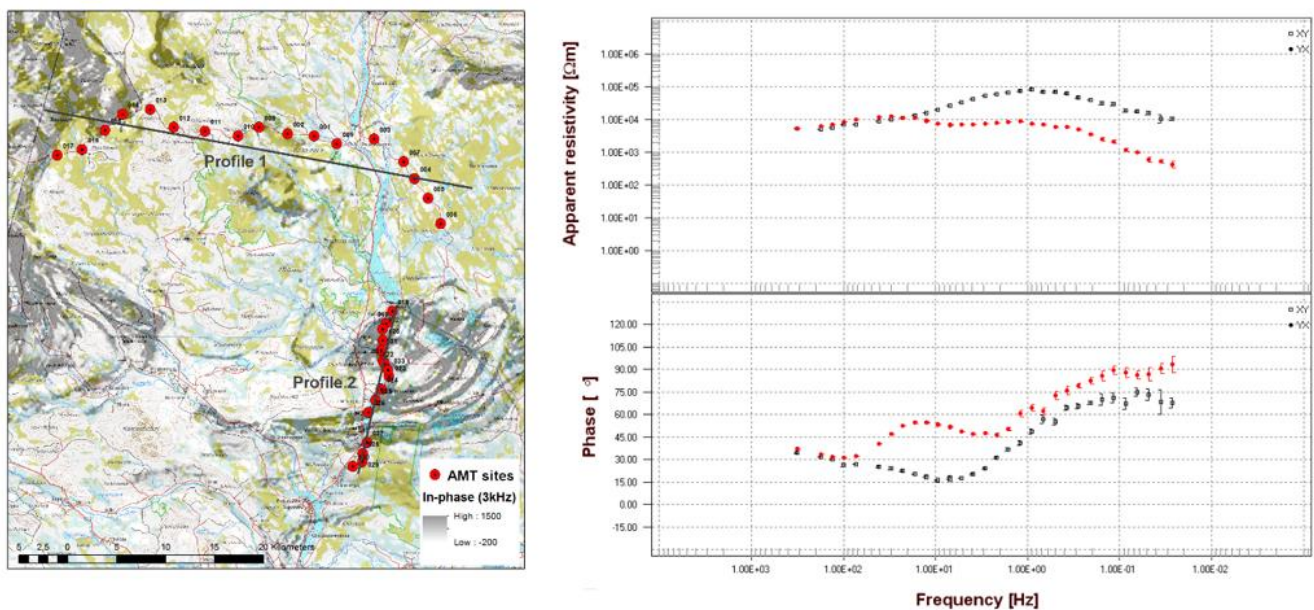


Figure 3.3 a) Location of AMT stations and inversion projection profiles. The background gray-shaded image is GTK airborne EM data. b) Example sounding curves from station X05.

3.1.4 Petrophysical data

We have used petrophysical surface sample data from three separate databases to support geophysical modeling in the Alaliesintie area (see chapter 4.3): 1) the GTK national petrophysical data register (NPDR), 2) the GTK Rock Geochemical Database (RGDB), and 3) additional sampling conducted along the seismic profiles by GTK in 2017. Petrophysical data are also available from a few drill holes on the southern side of the Koitelainen gabbro. However, this area is also well covered by surface petrophysics. All data have been recorded at the GTK geophysical laboratory, where density is determined by weighing the samples in air and water (Archimedes' principle), magnetic susceptibility with an in-house low-frequency (1025 Hz) AC bridge (Puranen & Puranen 1977), and the intensity and direction of remanent magnetization (the latter only for the 2017 oriented samples) with an in-house fluxgate magnetometer (Puranen et al. 1972).

The nationwide NPDR database consists of ca. 130,000 samples (Airo & Säävuori 2013; Korhonen et al. 1992). Each sample has a unique ID such that the main part of the ID identifies the sampling site and a subsequent letter separates samples taken from the same location (if several). Each sample has been assigned a lithological unit name; however, the naming is not systematic. The sample ID also reveals

the sample type, which includes outcrop, boulder, and block field samples, as well as samples of an unidentified type.

Petrophysical data have been determined for the samples in the RGDB dataset (Rasilainen & Lahtinen 2007), but they are not part of the database and have not therefore been published. The data are sparse in comparison with the NPDR, but its strength is the systematic lithological unit classification. The samples were taken either with a portable drill or a rock hammer, and each data entry includes the sample type classification (outcrop, boulder, block field).

The petrophysical sampling along the seismic profiles (Leväniemi et al. 2018) was conducted from outcrops with a rock hammer. The samples were oriented, which enabled the determination of the direction of remanent magnetization. Measurements were taken from 1–3 pieces of each sample, and the sub-sample data were averaged.

The data from these three sources (excluding boulder samples) were combined and quality assessed. Most notably, duplicate data rows and boulder samples were removed. The final dataset comprises 493 data entries.

3.2 Reflection seismic data

The project XSoDEx (eXperiment of Sodankylä Deep Exploration) acquired seismic reflection data in the Central Lapland region in 2017. The reflection seismic data were acquired in co-operation with the TU Bergakademie Freiberg from Germany and GTK. The xSoDEx dataset comprises over 80 km of seismic reflection profiles (Fig. 3.4). The data were acquired using 10-m receiver spacing and 20-m or 40-m source spacing, resulting in high-resolution data imaging bedrock structures down to 5 km depth. The survey utilized a 32-ton Vibroseis truck as a seismic source. These data have been utilized in the 3D geological modeling within the XL3D project.

Two different processing flows have been used to process the xSoDEx data. The first results were produced by TUBAF using their in-house-developed Coherency-Based Fresnel Volume Migration algorithm (Buske et al. 2009; Hlousek et al. 2015). The FVM method was successfully used earlier for seismic reflection data from the Kylylahti mining area in Eastern Finland (Heinonen et al. 2019). The receivers and source points are not along a straight line in the field geometry, and the FVM was calculated in a 3D volume taking the true source and receiver locations into account. The dimensions of the migration volume are larger than the actual profile length in order to preserve the reflection energy originating from the dipping features outside the receiver line. The method is based on coherency, which means that only the amplitude of the reflection is taken into account while the phase is neglected in order to enhance reflectivity. The FVM results form the basis for the 3D geological modeling of Sodankylä deep geology. The Pomokairantie profile (Figure) is connected to the Petäjäseltä HIRE seismic profiles in the west and extends to Peurasuvanto through Paistipuolet and Kaita-aapa. The Alaliesintie profile (Fig. 3.6) starts from the east side of the river Kitinen and extends

to the river Yläliesijoki through Rookkiaapa. The Kuusivaarantie profile (Figure) is the most southern of the XSoDEx survey lines located north of Sodankylä town. The Sakatti seismic reflection profile (Fig. 3.8) starts from the northern side of the Kenttäaapa swamp, which is inaccessible to seismic sources and receivers, thus preventing the acquisition of Kuusivaarantie and Sakatti data as one long continuous profile. The Sakatti profile runs along the roads Viiankiaavantie and Mataraojantie.

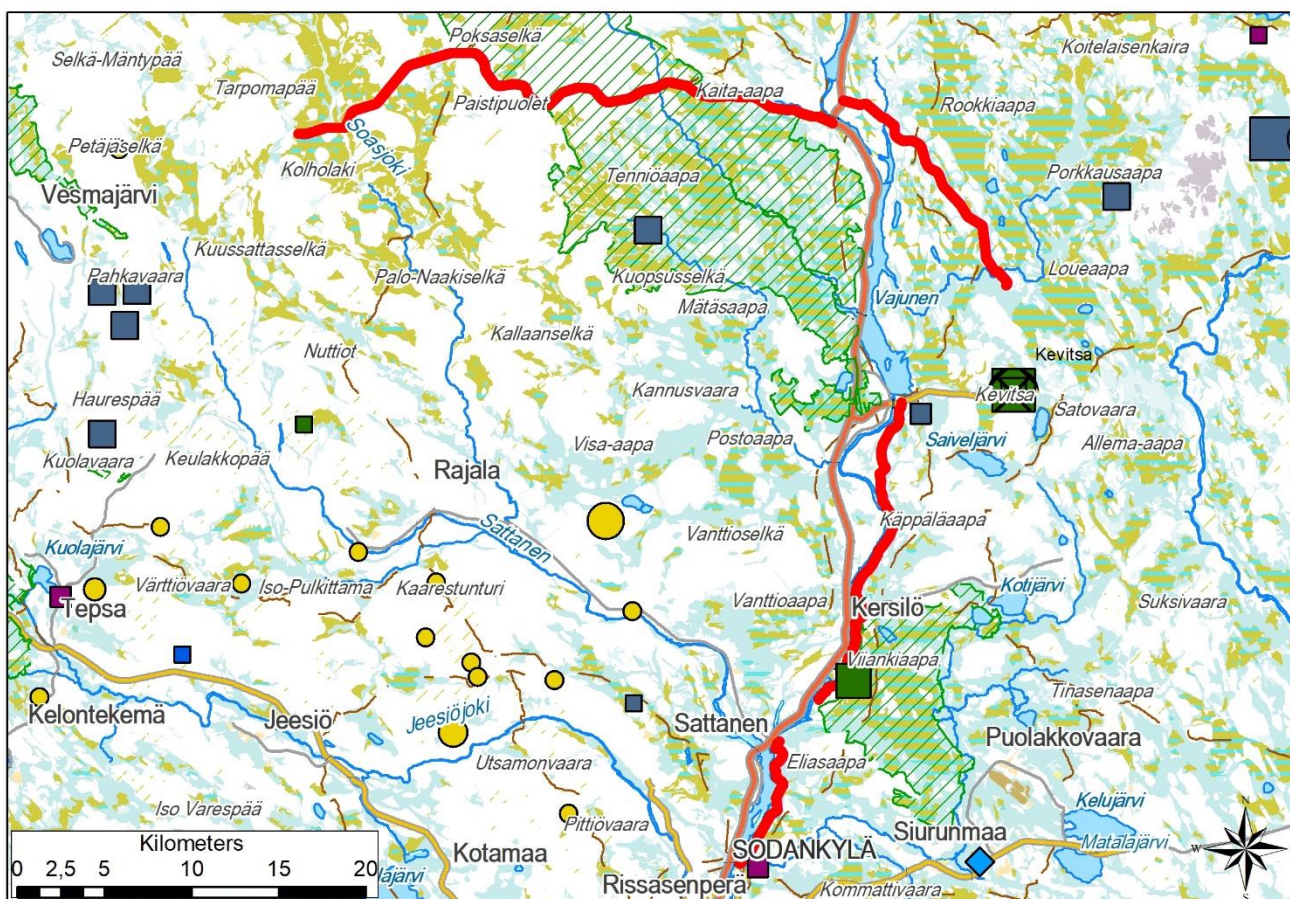


Figure 3.4. The XSoDEx survey lines in the central Lapland region. The survey was conducted along the roads. The known mineral deposits are marked on the map.

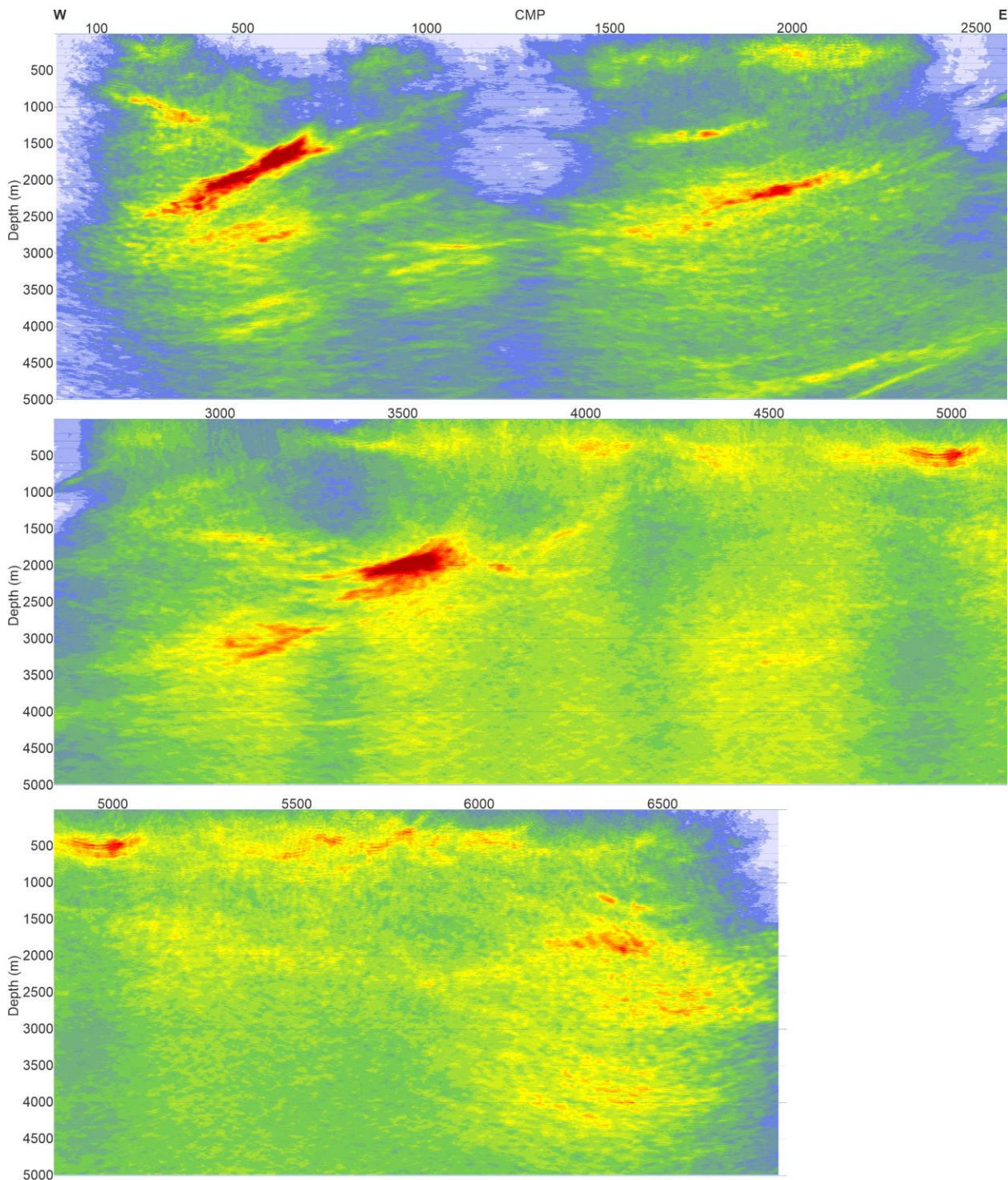


Figure 3.5. CBFVM processed seismic reflection data profile from Pomokairantie.

All of the CBFVM results share the same characteristics in that the shallow reflectivity is basically absent (upper 500 m or even 1000 m). This can partly be due to subvertical lithological contacts and faults that a seismic reflection survey is not able to directly detect because of the survey geometry. However, part

of the lacking reflectivity can be attributed to the data acquisition issues, especially to source-induced noise (ground roll), and also to data processing. The FVM processed data lack a data processing step called static corrections, which are used to correct the influence of overburden and surface topography on the travel times of the seismic waves. If the overburden is thicker in one place than another, it takes more time for a seismic reflection to reach the geophone at that particular location. In the stacking phase, this causes reflections to stack incoherently, and especially shallow reflectors that are seen with a higher frequency can be missed completely. Deep reflectors usually have lower frequency characteristics and they are not therefore as sensitive to small miss-alignments in the travel times.

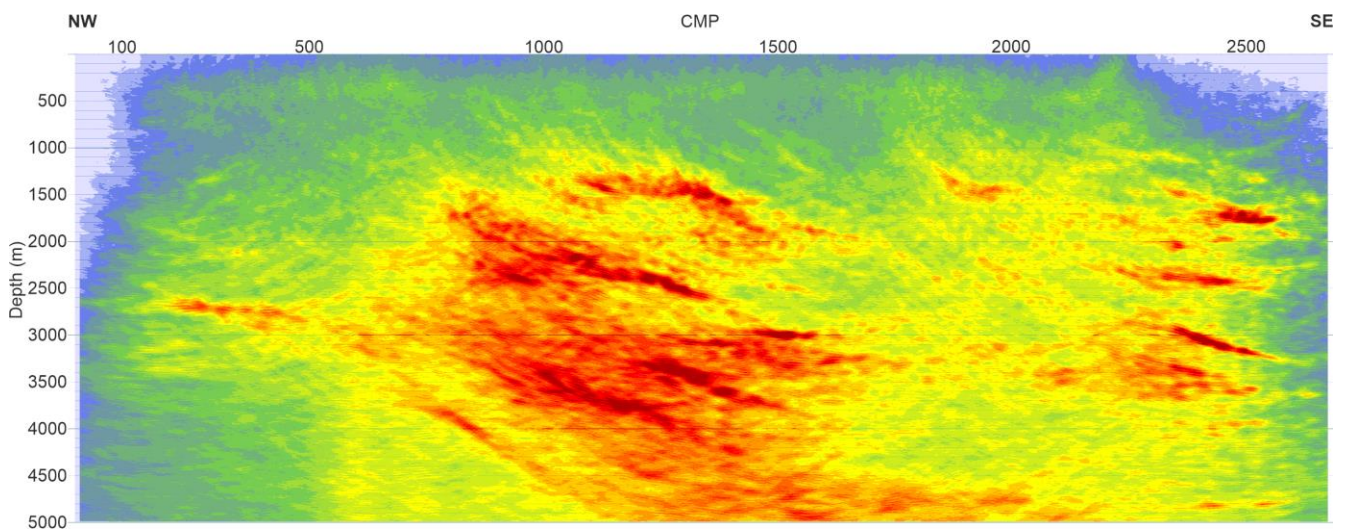


Figure 3.6. CBFVM processed seismic reflection profile from Alaliesintie.

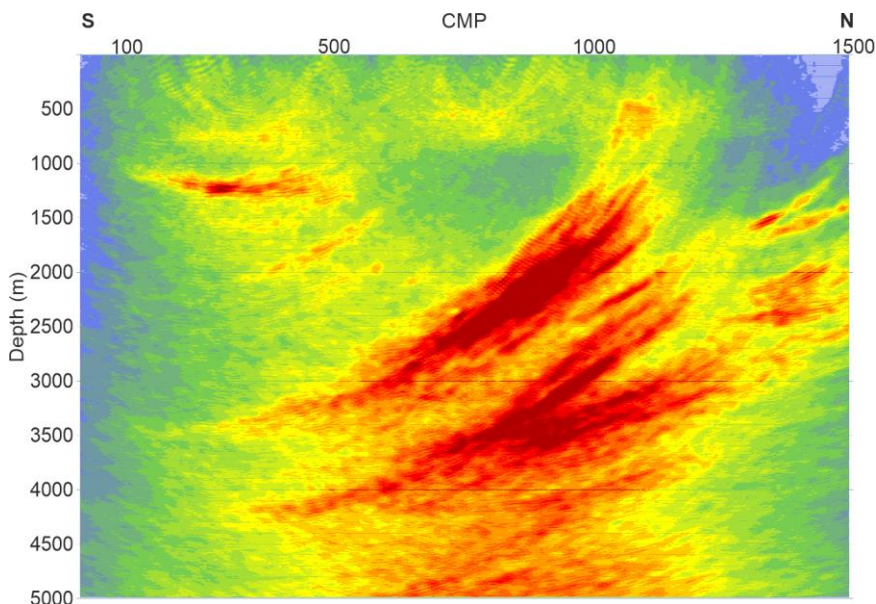


Figure 3.7. CBFVM processed seismic reflection profile from Kuusivaarantie.

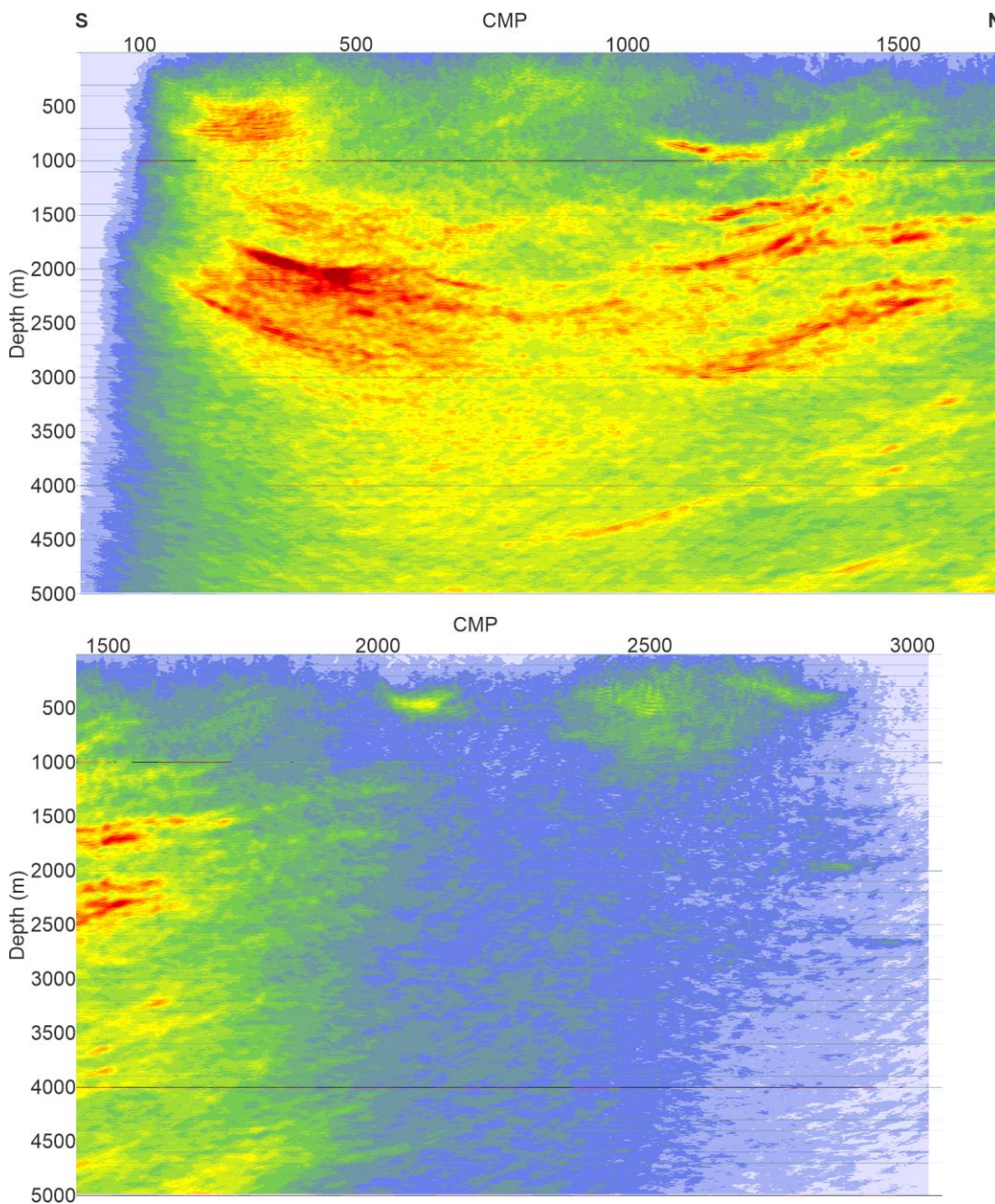


Figure 3.8. CBFVM processed seismic reflection profile from Sakatti.

In addition to CBFVM processing performed at TUBAF, the XSoDEx seismic reflection data were processed with a standard hardrock seismic data processing workflow using the software GNS Globe Claritas at GTK. These seismic sections, which have undergone standard data processing, are directly comparable to the HIRE seismic processing results, because they are processed in a similar manner. The processing flow included the following steps and parameters:

- Geometry setup: choice of a CMP line that smoothly follows the data acquisition road, 5-m CMP spacing
- Automatic gain control (AGC) with a 250-ms window
- Bandpass frequency filtering with corner frequencies 32–36–175–200 Hz
- Deconvolution
- FX deconvolution
- Airwave mute (333 m/s)
- Static corrections
- NMO corrections
- Stacking without normalization
- Stolt migration with velocity increasing with depth
- Time-to-depth conversion with the same velocity function as migration

Static corrections require tedious first-break picking of each shot gather, meaning thousands of picks for each seismic profile, and there was no time to perform this for the Kuusivaarantie and Sakatti profiles. Processing results using the standard workflow are presented in Figures 3.9–3.12. Details of the data processing are available in Heinonen and Keskinen (*in prep.*).

The XSoDEX seismic reflection data reveal subsurface reflectivity down to 5 km depth with a high resolution. The majority of reflections are near-horizontal or gently dipping, as seismic reflection surveys have a limited ability to image steep structures. Reflectors represent lithological contacts and fracture or fault zones that have caused changes in acoustic impedance in the bedrock. Interpretation of the seismic sections is presented in this report in the form of a 3D geological model.

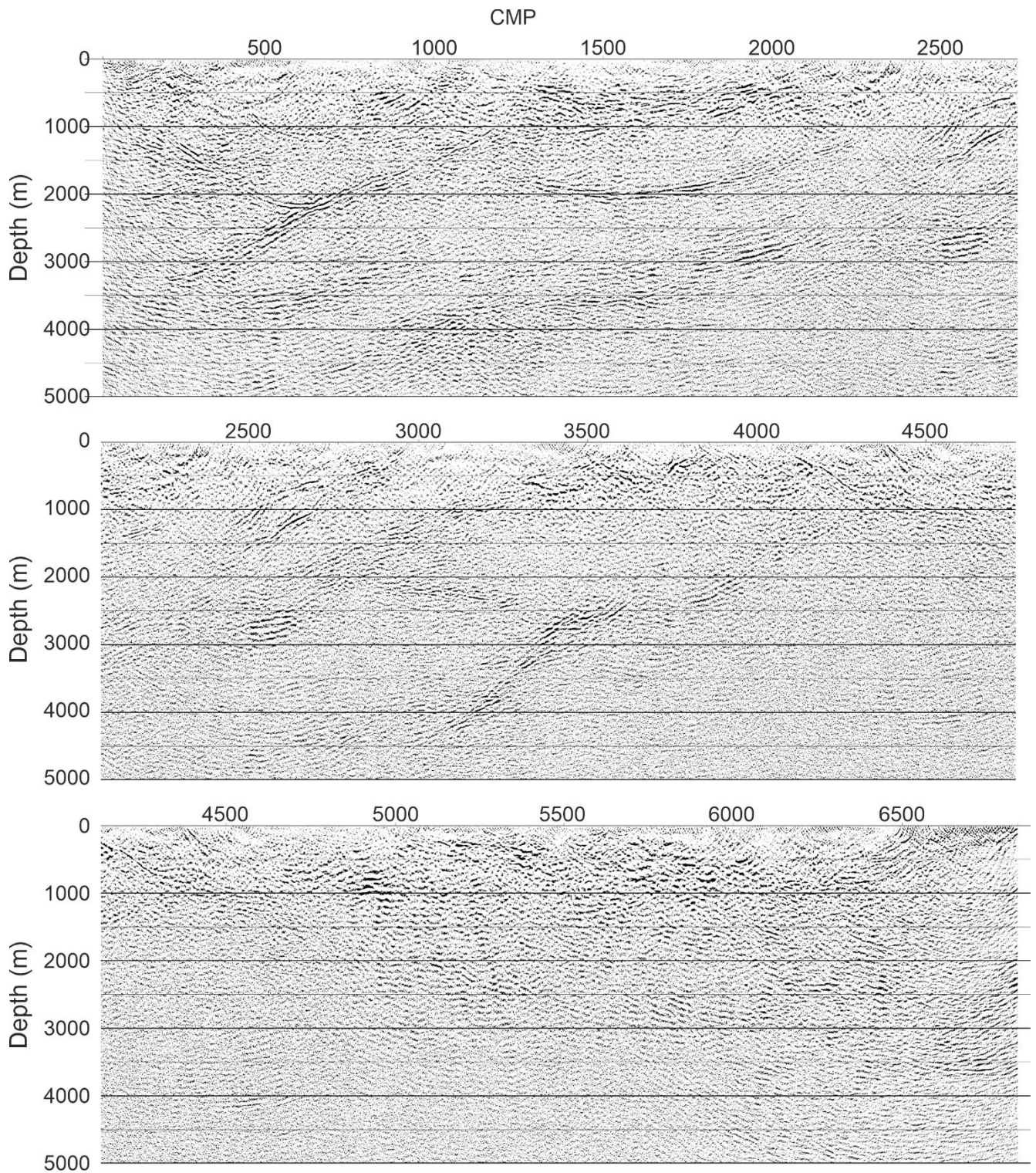


Figure 3.9. Pomokairantie seismic reflection profile processed with a standard hardrock seismic processing workflow including static corrections. CMP spacing is 5 m, so 500 CMP corresponds to a distance of 2500 m

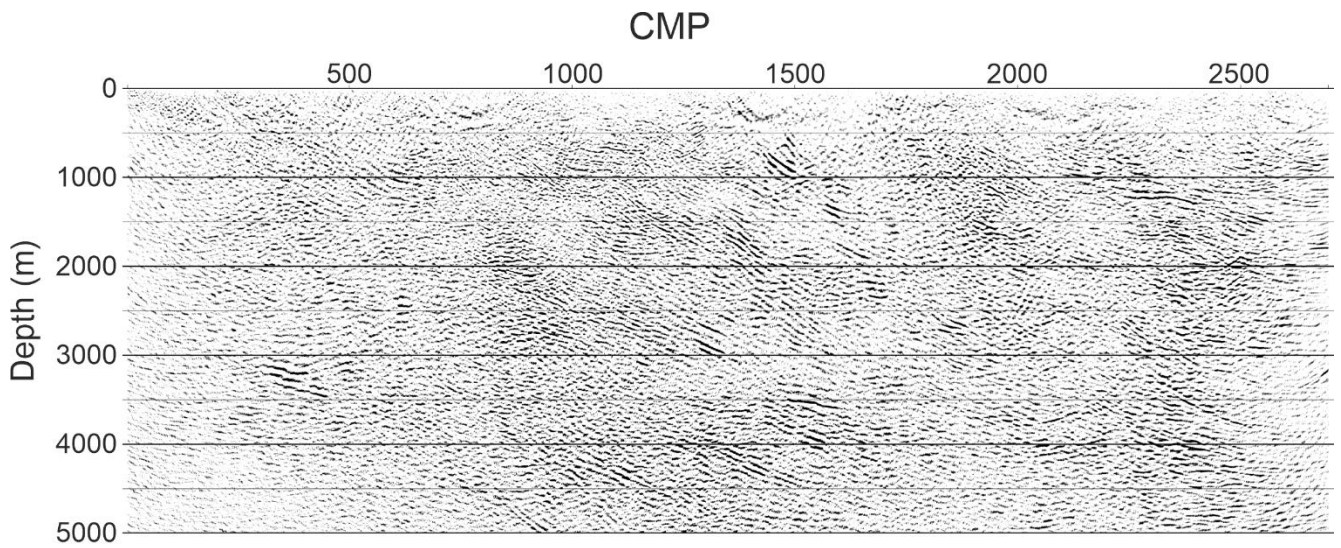


Figure 3.10. Alaliesintie seismic reflection profile processed with a standard hardrock seismic processing workflow including static corrections. CMP spacing is 5 m, so 500 CMP corresponds to a distance of 2500 m.

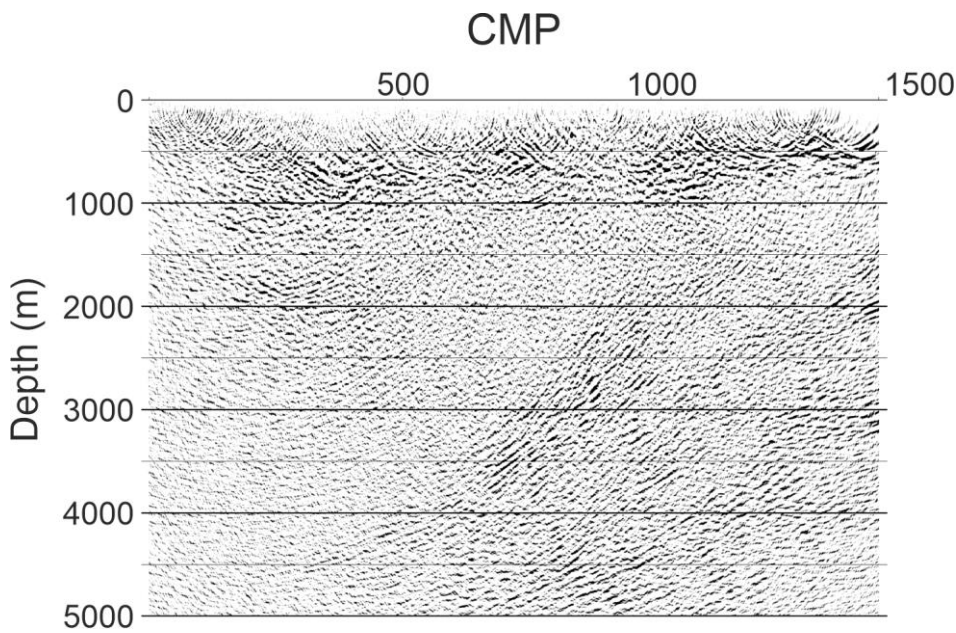


Figure 3.11. Kuusivaarantie seismic reflection profile processed with a standard hardrock seismic processing workflow excluding static corrections. CMP spacing is 5 m, so 500 CMP corresponds to a distance of 2500 m.

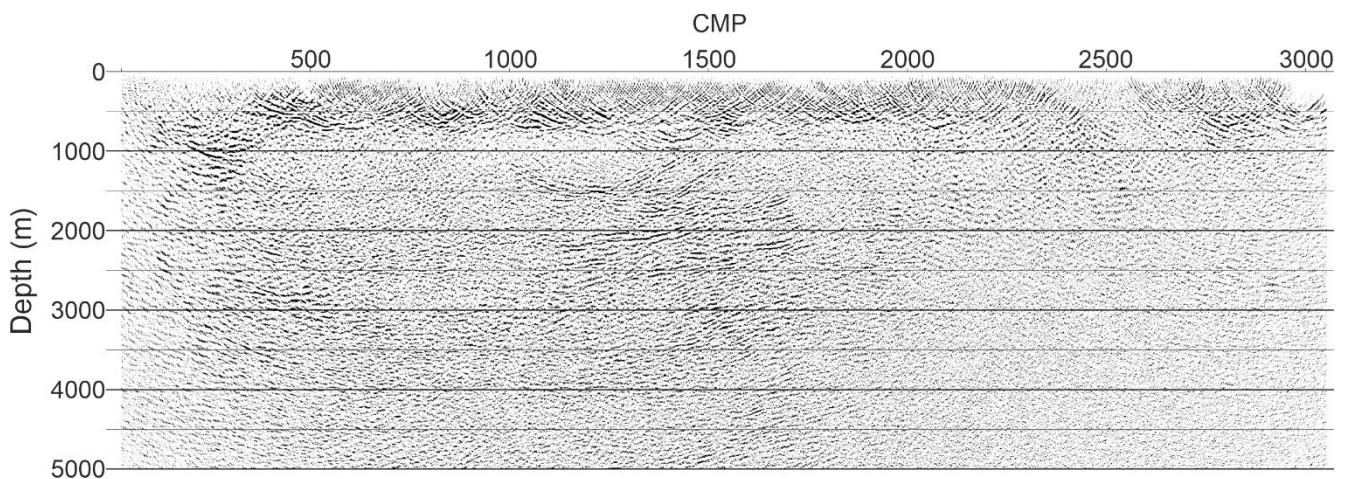


Figure 3.12. Sakatti seismic reflection profile processed with a standard hardrock seismic processing workflow excluding static corrections. CMP spacing is 5 m, so 500 CMP corresponds to a distance of 2500 m.

3.3 Regional geological and geochemical data

The regional geological data consist of a 2D bedrock map database (Bedrock of Finland – DigiKP) and its non-spatial unit database (Finstrati database). These databases are based on international vocabularies and are compatible with the international standards, and the naming of geological units follows the accepted guidelines and international stratigraphic codes recognized by the Stratigraphic Commission of Finland.

Table 3.2. The 3D modeled stratigraphic units and their geophysical characteristics.

Unit	Geophysical signature
Tenniövaara stock of the Nattanen suite	Gravity low, resistive
Kevitsa intrusion	High gravity and magnetic anomaly, non-reflective
Koitelainen intrusion	Varying response in gravity and magnetism; resistive, non-reflective
Kittilä Suite	High gravity and conductivity anomaly in parts, reflective
Sattasvaara formation of Savukoski group	High gravity and magnetic anomaly, resistive, non-reflective
Matarakoski formation of Savukoski group	Main rock type (graphite schist) highly conductive and reflective
Sodankylä group	Mainly low gravity and magnetic anomaly, resistive, reflective
Kuusamo group	Reflective, resistive, moderate gravity and magnetic anomalies
Salla group	Reflective, low gravity
Basement complex	Non-reflective, low gravity and magnetic anomaly, resistive

Due to the studied workflow of this project, in which 3D geophysical data play important role, special emphasis was placed on the geophysical characteristics of the modeling units (Table 3.2).

In addition to these units, the bedrock map database includes structural lines, which were used in the interpretation. No data of a smaller scale were directly used, i.e. no drill core or bedrock observation databases were used because their data are already included in the 2D bedrock map database and non-spatial unit database.

A regional till geochemical survey of the study area was conducted between 1971 and 1991 with a sampling density of one sample per 4 km² (Salminen 1995). The samples were taken from undisturbed till. Each sample consisted of 3 to 5 subsamples taken from an average depth of 1.5 m. The <0.06 mm fraction of the samples was assayed for Al, Ba, Ca, Co, Cr, Cu, Fe, K, La, Mg, Mn, Mo, Ni, P, Pb, Sc, Sr, Th, Ti, V, Y, Zn, and Zr using the ICP-AES analytical method after aqua regia digestion. In addition, Au, Te, and Pd were assayed using a graphite furnace AAS method.

4 WORKFLOW

4.1 General XL3D workflow

The XL3D project generated a general workflow for the process in which geological data are used in constructing a 3D geomodel and utilizing the data in prospectivity modeling. The workflow presents the various steps required in the compilation of the processed data into a common earth model (Fig. 4.1). The workflow excludes the data acquisition steps and is focused on the various data processing phases. The XL3D workflow is a general guideline presenting an ideal approach in this type of work. The various phases of the workflow are further explained in the following subchapters.

For the success of a project, it is necessary to be clear on the goals and define the parameters that are possible to extract from the available data. In the XL3D project, the aim was to generate a 3D geological model of the study area with key parameters related to magmatic Ni–Cu and orogenic gold mineral systems. Therefore, all the relevant data were collected and their quality was assessed. In the first processing phase, the data were processed into meaningful sets. This stage involved, for example, the interpolation of till geochemistry, extraction of various derivatives from the geophysical data, reprocessing and interpretation of seismic data, and generation of unconstrained 1-3D inversions of potential fields and AMT data. The aerogeophysical data and gravity data were clustered in the data integration phase into SOM clusters. The products of this first data processing and integration phase were used in the next phase, which was the generation of the initial 3D geomodel. The idea of the initial 3D geomodel is that it acts as a first-pass model that tests the existing 2D geological interpretation and provides constraints for second-phase inversion modeling. The constrained inversion modeling was conducted using available petrophysical data to test how well the initial 3D geomodel matched the measured geophysics. The testing focused on finding differences between the

constrained inversion model and measured data, which were corrected iteratively by adjusting the models until they matched the data with reasonable accuracy. The last phase carried out in the XL3D project was prospectivity modeling. This utilized the data generated in the first processing phase, the data integration phase, and parameters from the final 3D geomodel. In a data-rich environment (e.g. a mine site or near mine areas), the vast amount of 3D data may include, for example, 3D geochemical models. Data integration in 3D may be also included, as the methods (e.g. SOM) are usually not dependent on the dimensions. Similarly, prospectivity modeling can be conducted in 3D if the data are sufficient for this.

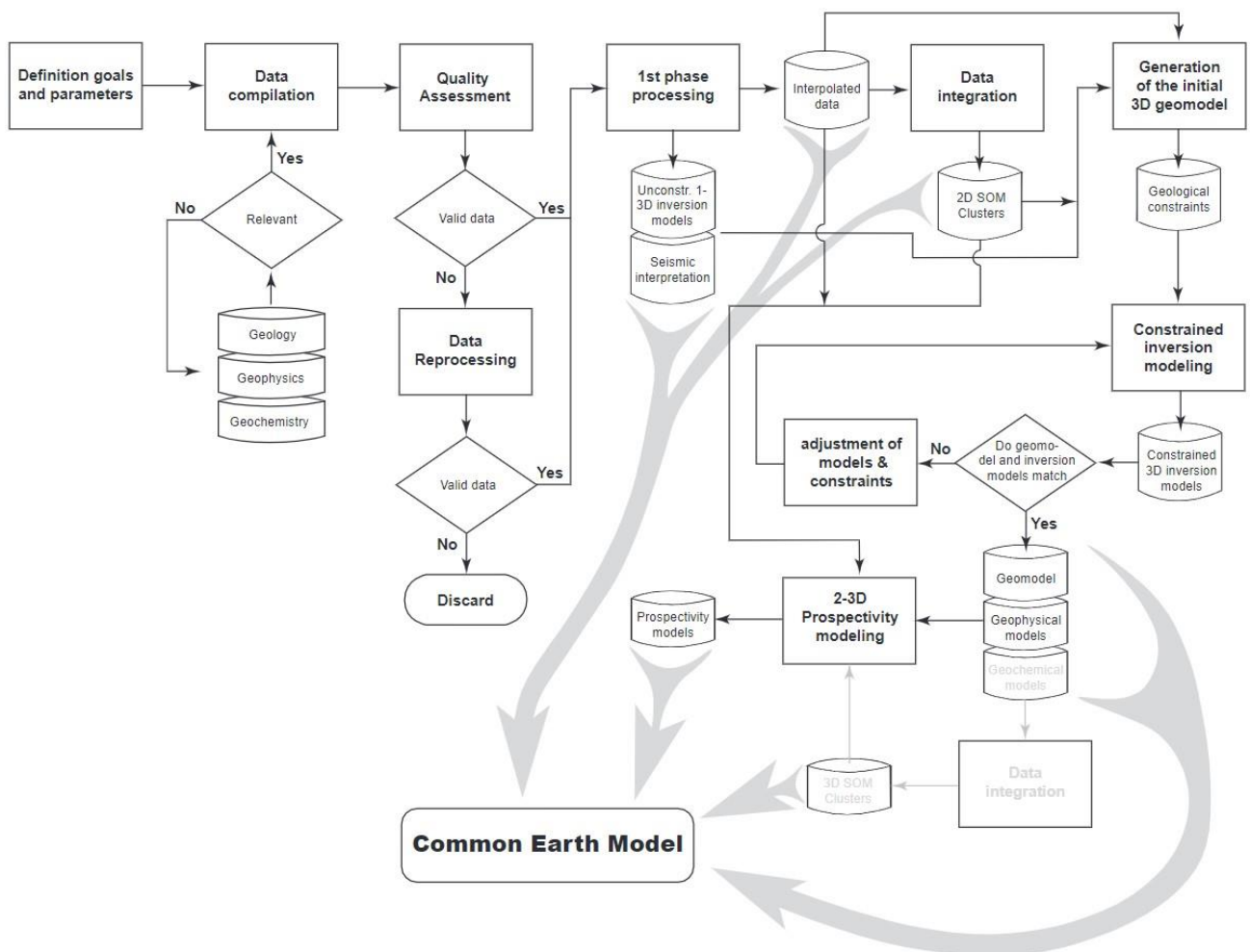


Figure 4.1. The XL3D workflow with process steps and data flow. The steps and data banks with light gray text indicate that they were planned to be carried out in the XL3D project but could not be accomplished due to a lack of sufficient data.

4.2 Self-organizing maps

We used self-organizing maps (SOMs) in conjunction with a k-means clustering algorithm as a clustering tool for the input data sets. Clusters were visually inspected and outliers were mapped. The general goal of clustering is to group the input data points without any prior knowledge about the groups so that inside a cluster the points are as similar as possible and between clusters the points are as dissimilar as possible. Outliers are data points that differ from other points.

A SOM (Kohonen 2001) is an artificial neural network capable of distinguishing similarity patterns in the data. It projects the data from the N-dimensional input space into a two-dimensional lattice of cells in the SOM space. Each SOM cell has the same dimensions as the input data; the vector values in the SOM cells are called weights. SOMs are generally used with large input datasets and a significantly smaller SOM lattice. This means that multiple input data points will be mapped to the same SOM cell.

The usability of SOMs comes from their topology-preserving nature: similar input data vectors are assigned to SOM cells that are close together. This is also the reason why SOMs can be used for clustering.

4.2.1 SOM process

Figure 4.2 presents an overview of the SOM process. The successive phases, labeled from A to G, are explained next.

A. Before running a SOM algorithm, the input data attributes have to be normally distributed. Thus, it is important to study the attributes one-by-one and apply appropriate transformation, generally logarithmic. The SOM algorithm is calculated with normalized values, and inverse transformation is applied after the SOM has been created.

B. The creation of a SOM includes some predetermined parameters. These are the size of the SOM lattice, the type of lattice, the grid shape, as well as multiple parameters related to the neighborhood and training in the algorithm. These parameters affect the results of the SOM and have to be frequently revisited and tuned if the results are not satisfactory.

C. The SOM algorithm works as follows:

- 1) Initialize the SOM cell weights. This is done either randomly or using principal component analysis.
- 2) Take one input data point and find the SOM cell that is closest to it. This cell is called the best matching unit (BMU).
- 3) Update the weights of the SOM cells for the BMU and its neighbors to be closer to the input data point.
- 4) Go back to step 2 until the training has been completed defined with the user-given parameter
- 5) Map all the input data points to their BMUs.

The formula for updating the weights in step 3 is

$$w(t + 1) = w(t) + \alpha(t)h(t)(x(t) - w(t))$$

where $w(t+1)$ is the new weight for a given neuron, $w(t)$ is the old weight, $\alpha(t)$ is a monotonically decreasing coefficient (learning rate), $h(t)$ is a neighborhood function, and $x(t)$ is the input data value. The learning rate ensures that the area in which the weights are updated shrinks over time and the neighborhood function ensures that the update is smaller the farther away the neuron is from the BMU in the SOM space.

D. To study outliers, the quantization error can be calculated. This is the difference between an input data point and the SOM cell weight in its BMU. If the value is large, the algorithm did not yield any SOM cells that are close to the data point; these points are considered as outliers.

E. Although the SOM cells themselves can be considered as clusters, their number is often too large for practical use. Thus, the cells are further clustered using either visual inspection or, more commonly, a clustering algorithm. K-means is one of the most common simple algorithms. It aims to minimize the variances within clusters by assigning observations to the closest cluster centroid and recalculating the centroids. This is repeated until no updating occurs. K-means generally requires the user to give the number of clusters as a parameter, but an optimal number can be found by calculating a goodness index for numbers in a given range. In this project, the Davies-Bouldin index (Davies & Bouldin 1979) has been used.

F. SOM is a powerful visual tool and the final step is to examine the results. The clusters and quantization errors can be shown on a (geographical) map to study their location. The quantization errors are especially interesting in prospectivity analysis, as high errors, i.e. outliers, sometimes correspond to prospects. Visualizing the SOM one input attribute at a time provides a useful tool to describe the attributes of clusters.

G. Finally, if the results are not satisfactory, the process should be run again, as multiple parameters as well as random number generation affect the SOM algorithm. The process can be changed by selecting a different set of input data, using different parameters for the SOM or k-means clustering, or simply rerunning the SOM or k-means algorithm using a different random seed.

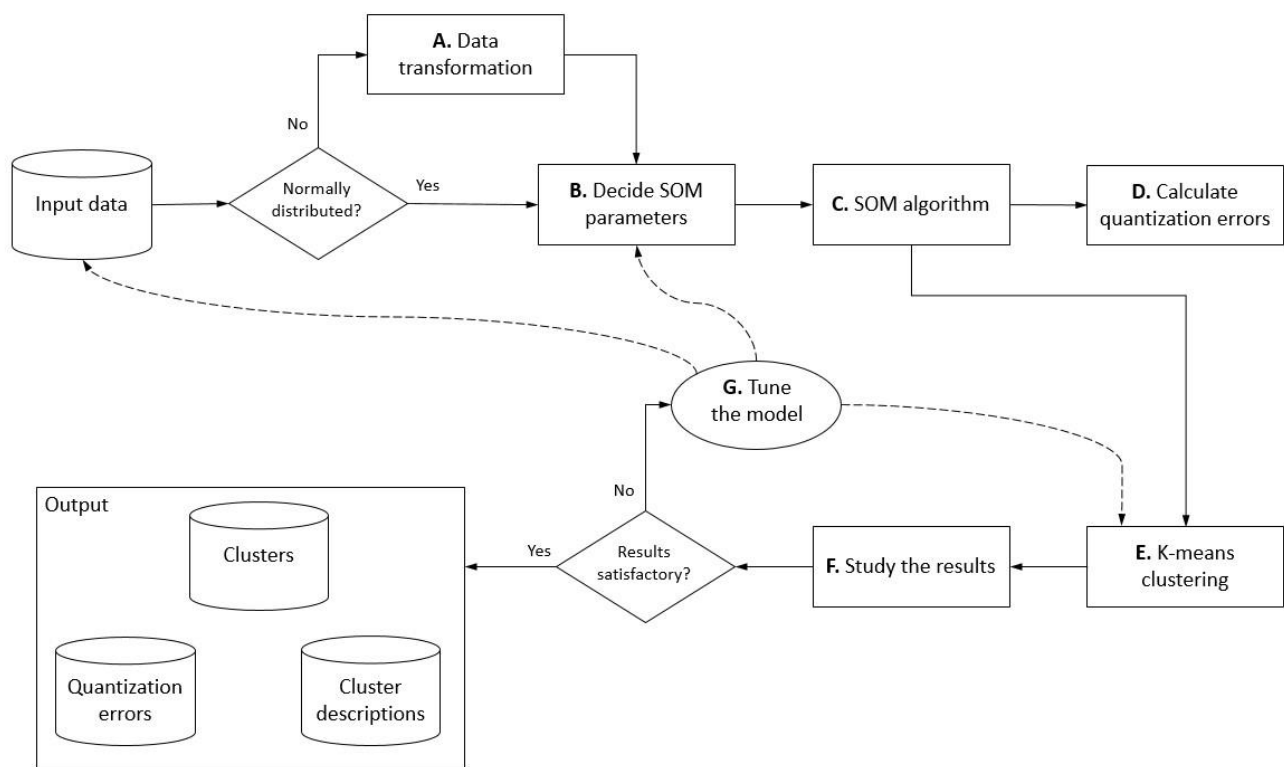


Figure 4.2. The SOM process.

4.2.2 SOM results

Multiple data sets, including till geochemical, airborne EM, magnetic and radiometric data, as well as gravimetric data were tested during the project. However, the final SOM was calculated using four geophysical raster datasets: the in-phase and quadrature components of GTK's 3 kHz frequency-domain airborne electromagnetic (AEM) data, GTK's airborne magnetic data (total magnetic field intensity, TMI), and the residual Bouguer anomaly of GTK's regional gravity data with the 500 m upward-continued field removed. The resulting clusters are displayed in Figure 4.3.

Based on histograms as well as skewness and kurtosis statistics, the attributes of the AEM quadrature, AEM in-phase, and TMI data have been normalized using logarithmic transformation. The size of the SOM has been set to 20 x 20 cells, the type of the lattice to toroid, and the grid shape to hexagonal. The number of clusters has been optimized between 10 and 20, and 10 is the optimal number. The range between 5 and 20 has also been tested, but the resulting 5 clusters has been seen as too few.

Quantization errors (Q-errors) are presented in Figure 4.4; the lighter the area, the higher the error value. Plotting the errors on top of clusters is a good method to study interesting areas, especially in prospectivity modeling.

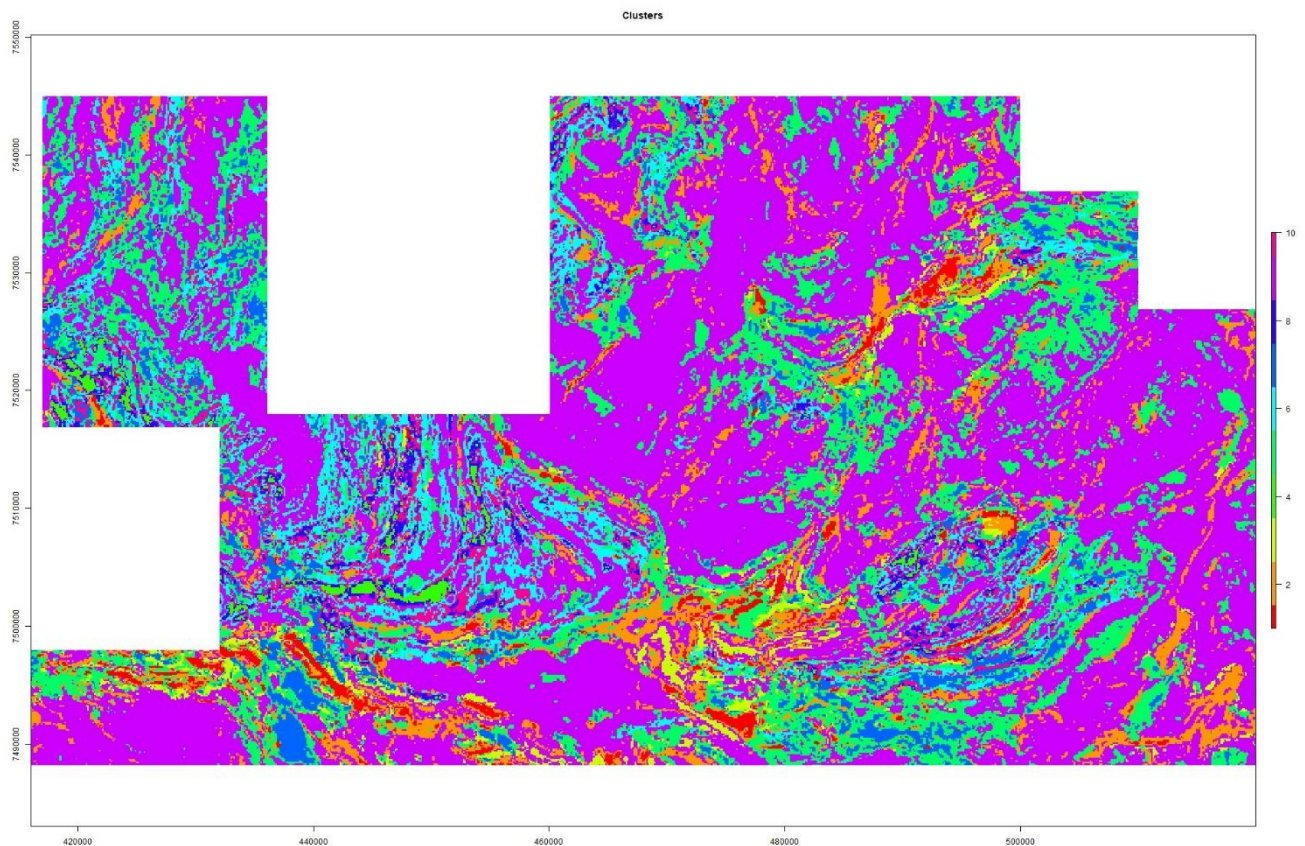


Figure 4.3. Clusters from SOM and the k-means algorithm.

To describe the clusters, multiple visualization techniques can be utilized. The easiest one involves showing each attribute at a time for one cluster at a time in the SOM space. An example of this is presented in Figure 4.5, which displays the attributes for SOM cells for cluster number 4. In this cluster, the AEM quadrature ranges from low to high values, AEM in-phase is high, gravity is middle to high, and TMI is low.

To show all clusters and their attributes at the same time, a more complex form of visualization can be used with clusters as colors and attributes as a chart on top of the SOM cell. This is displayed in Figure 4.6.

Table 4.1 presents descriptions of all clusters and their attribute values. The color after the cluster number refers to the colors used for the clusters in the above map view (Fig. 4.3) and SOM view (Fig. 4.6). The number of cells that the cluster has is also included.

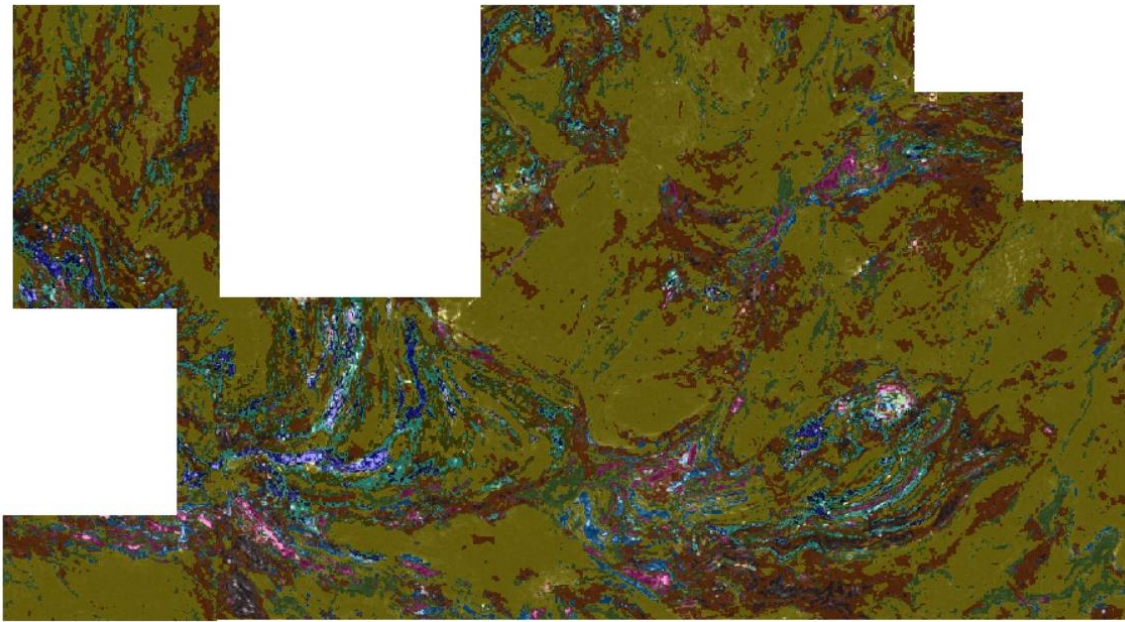


Figure 4.4. Clusters and quantization errors. The lighter areas indicate high error values.

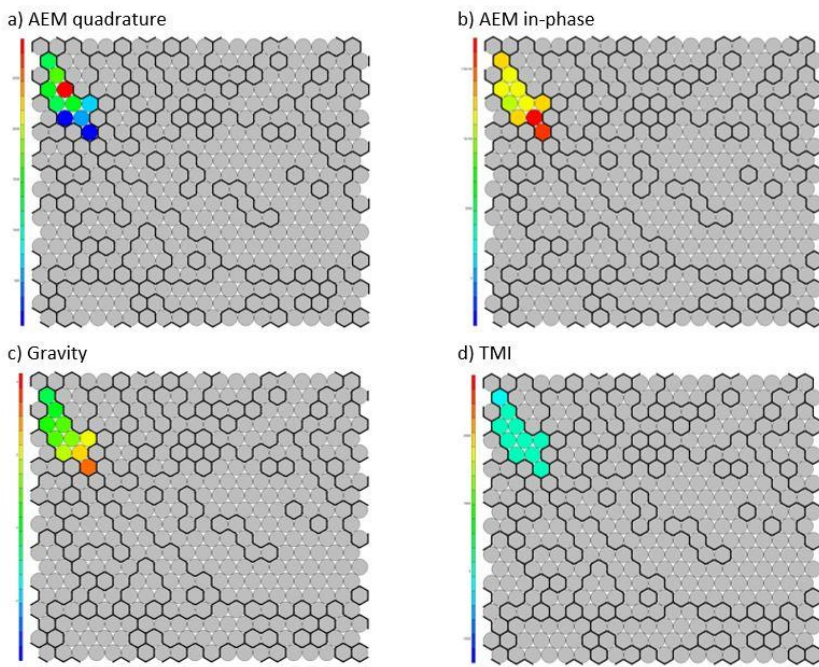


Figure 4.5. Visualization of attributes in cluster number 4.

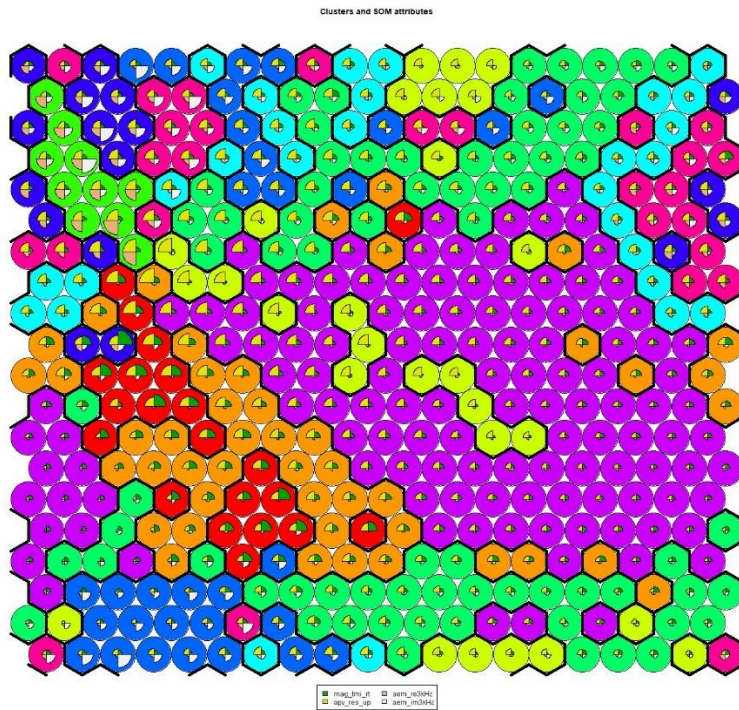


Figure 4.6. SOM clusters and attributes.

Table 4.1. Description of clusters.

Cluster	Number of cells	EM quadrature	EM In-phase	Gravity	TMI
1 (Red)	Small	Low-middle	Low	Middle-high	Middle
2 (Orange)	Moderate	Low	Low	Middle	Middle
3 (Yellow)	Small	Low-middle	Low	Low-middle-high	Low
4 (Saturated green)	Small	Low-middle-high	High	Middle-high	Low
5 (Green)	Large	Low-middle	Low	Low-middle	Low-middle
6 (Cyan)	Moderate	Low-middle	Low	Middle	Low
7 (Light blue)	Small	Middle-high	Low	Low-middle	Low-middle
8 (Dark blue)	Small	Low-middle-high	Middle	Middle	Low-middle-high
9 (Purple)	Very large	Low	Low	Low-middle	Low
10 (Magenta)	Small	Low-middle-high	Middle	Middle	Low-middle

The generated clusters were visually compared with GTK's digital bedrock map DigiKp 200k. In general, there is a broad correlation in the number of lithological units with the different clusters, which is unsurprising, as much of the geological map is based on geophysical data due to the limited outcrop exposure within the study area. However, a number of the clusters highlight subareas within lithological units and also domains across lithological boundaries.

Clusters 1 and 2 correlate relatively well with mafic to ultramafic lithologies, including gabbros, diabases and komatiitic volcanic rocks. In komatiitic units, clusters one and two preferentially outline the peridotitic komatiites. Cluster 3 dominantly highlights the komatiitic basalts of the Sattasvaara formation. In addition, it highlights areas in Kumpu group sedimentary rocks near the contacts of the 2.0 Ga and 2.2 Ga mafic sills and dykes. Cluster 4 chiefly occurs within the graphite-bearing tuffs and sedimentary rocks of the Kittilä suite and Savukoski group. Cluster 5 covers a large area and extends over a vast variety of different lithologies, from mafic to ultramafic in composition. Cluster 6 is relatively extensive, but mainly highlights the graphite-bearing units within the Kittilä suite and Savukoski group, similarly to cluster 4. Cluster 7 contains a relatively small number of cells that occur in a relatively high number of different lithologies in an inconsistent manner. Cluster 8 behaves similarly to cluster 4, except that it also extends to the banded iron formation rocks of the Porkonen formation. Cluster 9 is the most extensive. It highlights most of the felsic units, including quartzites, mica schists, and Archean basement gneisses. However, it also covers most of the Koitelainen layered intrusion and large areas of the Kittilä suite tholeiitic basalts. Cluster 10, with low-middle-high and middle values for EM quadrature and in-phase, respectively, behaves similarly to clusters 4 and 8 with respect to lithological correlation.

The clusters were also visually correlated with known Au and Ni–Cu deposits. For the gold deposits, no clear pattern was observed. However, the Kevitsa intrusion and the Ni–Cu–PGE deposit is highlighted by clusters 1 and 2. Similarly, the Sakatti Ni–Cu–PGE deposit occurs within the cluster 2 domain. The known deposits were also checked against the quantization error map, in which the most pronounced feature is the relatively high Q-error anomaly correlating with the Kevitsa intrusion. A smaller Q-error anomaly is also located just south of the Sakatti deposit. No clear pattern was found between the Q-error map and known gold deposits.

4.3 Potential field inversions

4.3.1 Inversion methodology

Potential field inversions were conducted in three stages: 1) regional gravimetric and 2) magnetic inversions to support regional geological modeling, and 3) gravimetric inversion in the vicinity of the Alaliesintie seismic profile to support the geological modeling of the Alaliesintie area. The regional inversions were run without geological constraints (unconstrained). For the detailed model, we studied

how geological constraints are best applied with the available petrophysical data and selected modeling scenario for the Alaliesintie gravimetric inversions.

Gravimetric inversions were mainly completed using commercial Grav3D v3.0 software by the University of British Columbia (UBC) (Li & Oldenburg 1998). Grav3D is a regularized inversion that produces a 3D mesh of subsurface relative density values that would result in an anomaly close to the one observed in ground or airborne gravity measurements. The corresponding software for magnetic data is Mag3D (Li & Oldenburg 1996). Mag3D assumes that the magnetization completely consists of induced magnetization and thus the recovered model represents a scalar magnetic susceptibility. Remanent magnetization (and anisotropic magnetic susceptibility) are assumed absent.

Some regional gravity datasets and the magnetic data were inverted with the Geosoft VOXI package, a potential field inversion tool by Seequent Ltd (formerly Geosoft) available as an extension to Geosoft Oasis Montaj software. Its regularized inversion process and constraint formulations are comparable to those in the UBC software. However, in addition to magnetic susceptibility inversion available in MAG3D, VOXI also offers a recent component named Magnetic Vector Inversion (MVI), which solves for the direction and magnitude of the 3D subsurface magnetization, thus allowing for remanent magnetization (MacLeod & Ellis 2013). More specifically, the algorithm solves for a scalar property and its direction vector. The scalar property represents the magnitude of the total magnetization in susceptibility units, i.e. 'MVI susceptibility'. The vector nature of the inversion makes building constraints rather complicated, as they should also be presented as vectors (even if scalar in nature). MVI inversion was used in this project for the magnetic data.

Potential field inversion is always non-unique, meaning that an infinite number of 3D petrophysical distributions produce the observed data. Geological constraints can be imposed on the inversion in order to reduce the ambiguity inherent to the process and to increase model reliability. A thorough practical guide to constraining Grav3D and Mag3D inversions is given by Williams (2008).

Regularized Grav3D (and Mag3D) inversions produce the recovered subsurface model by minimizing the so-called model objective function, which is a sum of the data fit and regularization terms. The data fit term ensures that the inversion complies sufficiently well with the observed data. The regularization term is a composition of several constraints such as smallness and smoothness (Williams 2006, 2008). The smallness term minimizes the deviation between the recovered inversion model and the user-supplied expected 'target' model (called the reference model constraint). The smoothness terms minimize the coarseness of the model: any deviations between the recovered model and the reference model are spread over a number of cells instead of letting them concentrate on individual cells. The algorithm also controls the model by imposing the depth attenuation behavior characteristic of gravimetric or magnetic fields. A useful constraint in addition to or instead of reference models is restricting of the upper and lower boundary property values in some or all of the model cells (bounds constraint). The reference model constraint is a 'soft' constraint, which means that the recovered

model is allowed to deviate to some extent from the reference model. However, bounds constraints are strictly imposed.

The reference model and bounds constraints are included in the inversion as petrophysical data. The petrophysical data can be ‘raw’ measurement data (for example, from surface sampling or drill hole logging) that are used to guide the inversion towards the observed petrophysical data. However, if a geological model is available and can be expressed in terms of petrophysical value ranges, the constraints can also be expanded outside the observed petrophysical data space. It should be noted that the geological model does not have to cover the complete modeling space, but can be, for example, a model of the shallow bedrock or a sub-model enveloping a drilled target.

To apply a geological model as a constraint in UBC-GIF or VOXI inversion, the geological knowledge must be expressed 1) as petrophysical values and 2) in the inversion model framework.

4.3.2 Linking geology to petrophysics

If a geological model is available and is to be included in the inversion as a constraint, the geological model units must first be mapped into petrophysical values. This requires petrophysical knowledge, typically measurement data, of the geological units to be modeled.

The more precisely the geological units can be expressed in terms of petrophysical value ranges, the more reliably they can be applied as inversion constraints. This may require consideration of the sampling and modeling scales. For example, in Finland, outcrop petrophysical data are available at the regional scale for nearly all parts of the country and can be used to constrain (regional) inversions together with the surface geological map. However, the bedrock map is a generalization of the outcrops, and any geological 3D model is often a further generalization of the bedrock map, which may conflict with the data collected from petrophysical samples (Fig. 4.8). The question that then arises is how to link the outcrop-scale petrophysical data with the geological 3D model units.

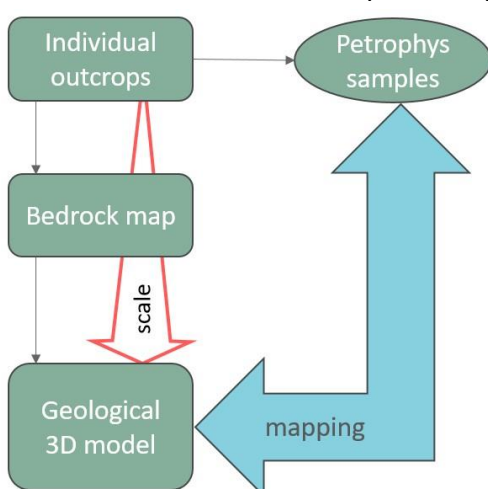


Figure 4.8. The effect of scale in mapping outcrop petrophysical data into geological constraints.

To address the difference in data scales, petrophysical data often need to be reclassified to the classes of geological model units. This can be done, for instance, based on the lithological names (if available) of samples or sample locations. Density as a rock property is controlled by the same major minerals that are also used as a basis for lithological classifications, and thus often correlates well with lithological units. This is not necessarily the case for magnetic susceptibility, which is dominated by minor mineral components of the rocks (Dentith et al. 2019). Several factors such as weathering, alteration and metamorphism may also disturb the classification of data into lithological classes. In some cases, modification of the geological classification may also be necessary: a lithological class may contain sub-classes with a sufficient petrophysical contrast to justify separation into new units (for example, a layered gabbro with layers of high and low magnetic susceptibility).

Geophysical modeling can only distinguish between units that have petrophysical contrasts; lithological units with similar petrophysical value ranges cannot be separated from each other. To achieve the best possible results in iterative/integrated geophysical–geological modeling, the discussion between the geologist and geophysicist on the data scales, modeling units, and petrophysical contrasts should continue throughout the modeling process.

If a complete geological model exists, it can be included as a complete reference or bounds constraint model, assuming that the related petrophysical properties are known; this scenario may be useful, for example, in geological model validation. More often, however, the geological 3D space is only partially known, and in such a case, a partial constraint model can be included to also improve the recovered model reliability in the unconstrained space. The property values in the cells of a reference model can be, for example, the mean property values of petrophysical data observed or those of the geological rock class. The restrictions for the upper and lower property value allowed in each cell (bounds constraint) can be defined based on the property distribution and statistics derived either from measured petrophysical data or the value distributions of the units.

4.3.3 Inversions and results

Regional gravimetric inversions

Regional gravimetric 3D inversions were carried out for the regional gravity data of GTK. The regional gravity measurements of the central Lapland area started in 1972, and the current total number of observations is about 25,000 points. The density of regional gravity observations is usually 1–4 per square kilometer in the dataset. Additional gravity measurements were performed in 2017 along the seismic survey profiles with 100-m station spacing. These new data were combined with older gravity data and 3D inversions were carried out using UBC Grav3D and VOXI. As an example, Figure 4.9 presents one set of results of 3D inversion using Geosoft Voxi.

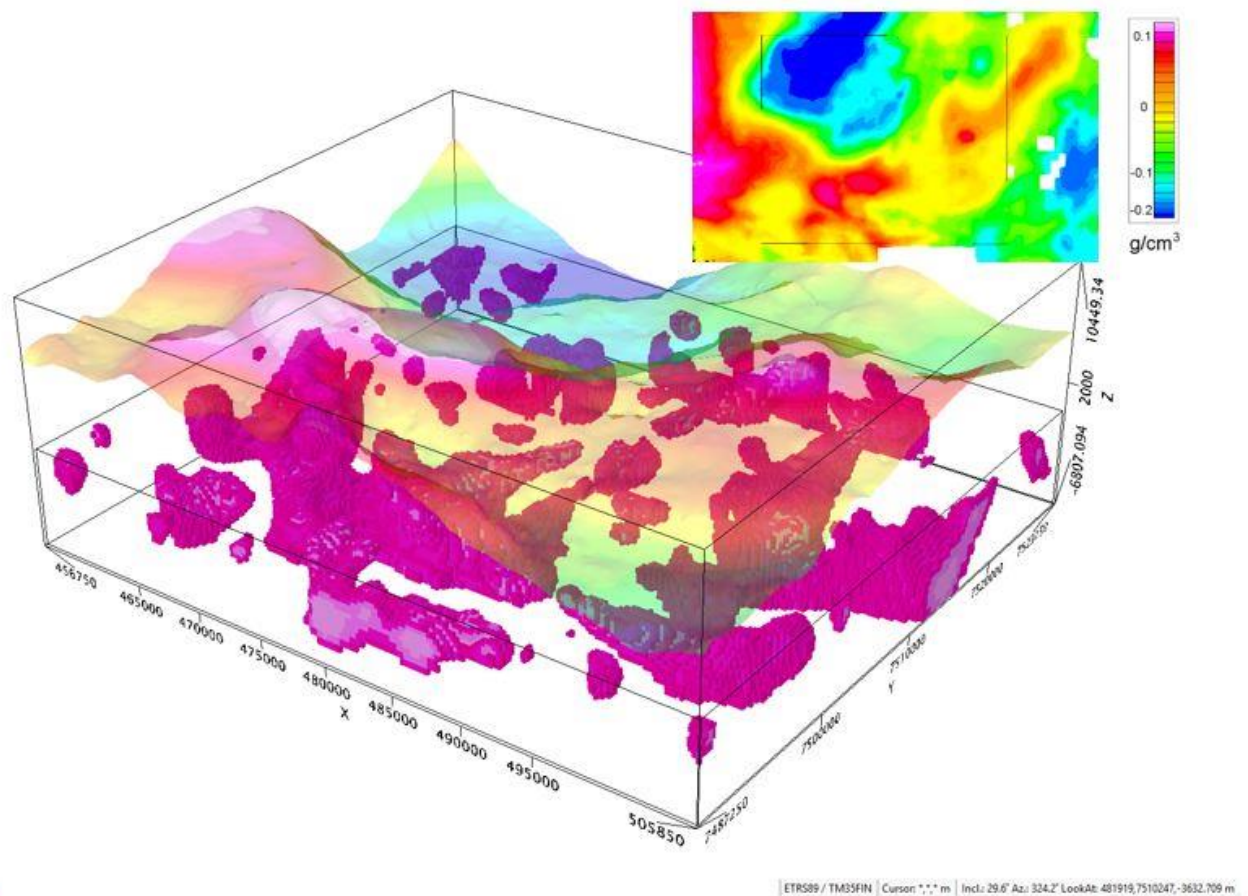


Figure 4.9. A 3D gravity model of the XL3D survey area.

Regional magnetic inversions

Comparison of the total magnetic field intensity data with its various transformations (most importantly pole-reduced data (RTP) and the analytic signal) may give an indication of natural remanent magnetization (NRM). In the study area, it is likely that most magnetic sources are dominated by induced magnetization (proportional to magnetic susceptibility, directed in the field of the Earth's current magnetic field). However, some 'negative' (in reference to the regional zero level) features remain in the RTP data that may indicate the local presence of remanent magnetization with a direction that deviates from the current field (Fig. 4.10).

The petrophysical data collected by GTK in 2017 along the seismic profiles (Leväniemi et al. 2018) indicate that Königsberger (Q) ratios (the ratio of NRM to induced magnetization) are often >1 for ferromagnetic ultramafic volcanic rocks ($Q = 1-3$), meaning that NRM may be the dominant magnetization component in these rocks. However, no characteristic magnetization direction could be determined regionally.

The negative magnetic anomaly in the center of the Kevitsa intrusion dunite layer indicates remanent magnetization. The anomaly is due to a 55-m-thick layer with strong remanent magnetization having a clearly negative inclination direction: based on petrophysical measurements and modeling, $Q = 4.2$, NRM inclination -42° ($-52^\circ \pm 15^\circ$), and declination 240° ($246^\circ \pm 5^\circ$) (Montonen 2012, values in parentheses from Fournier et al. (2020)).

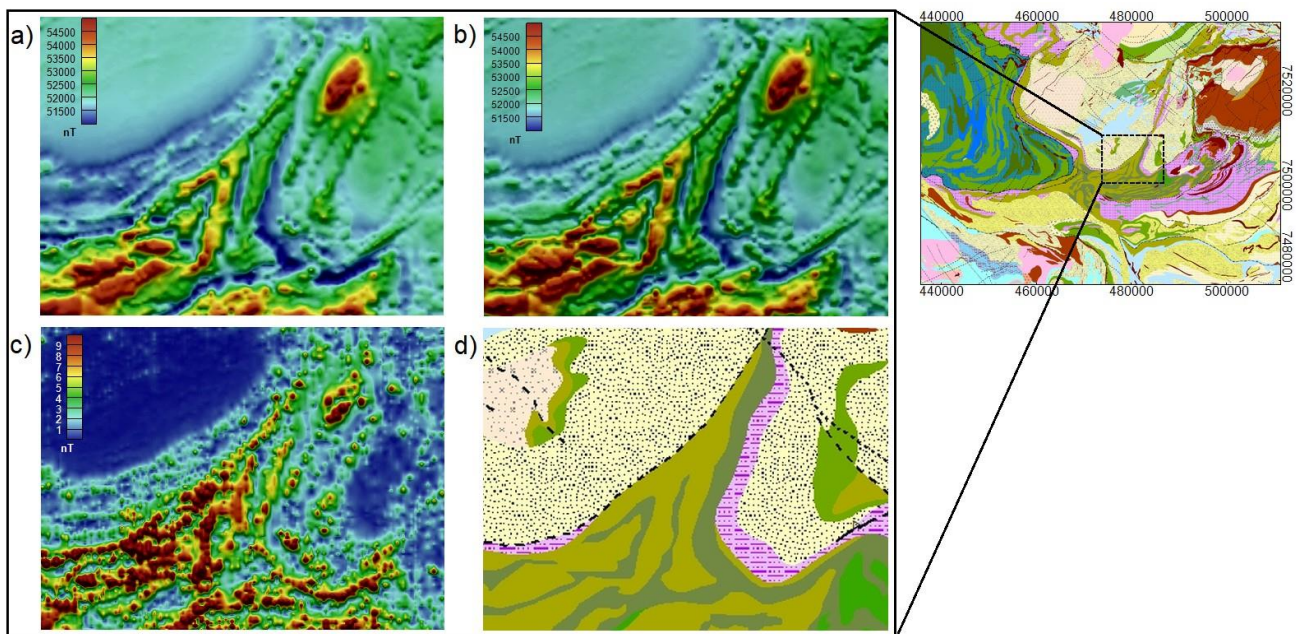


Figure 4.10. A detail from the magnetic data. a) Magnetic total field intensity, b) RTP transformation, c) the analytic signal, d) a lithological map. Possible remanent magnetization is shown as 'negative' values (dark blue) in a) and b).

The above-mentioned indications of NRM were considered when selecting the inversion method for the regional magnetic inversions. Although conventional inversion for magnetic susceptibility (i.e. magnetization aligned with the current Earth's field) is more straightforward, we selected the MVI technique due to the possible local presence of remanent magnetization. All regional inversions were performed with MVI. We also present a comparison with the magnetic susceptibility inversion from the area shown in Figure 4.10.

In an attempt to simplify the inversion problem and to reduce the calculation times, the study area was divided into thirteen subareas with distinguished magnetic anomalies. The subareas focus on the seismic profiles and most significant magnetic anomalies (Fig. 4.11). The inversions were performed on a residual magnetic grid (5 km upward-continued field removed from the total intensity data). The inversions were geologically unconstrained. Key inversion parameters are compiled in Table 4.2.

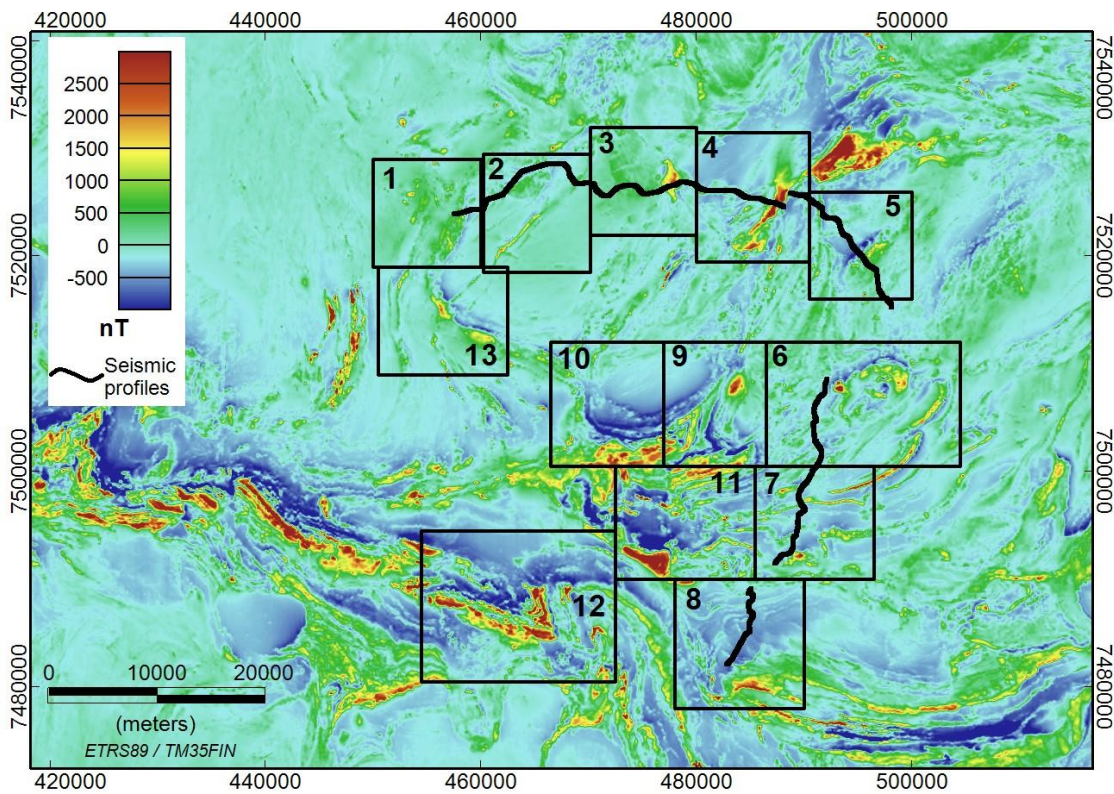


Figure 4.11. MVI inversion subareas 1–13 on top of the residual magnetic grid used as the inversion input data.

Table 4.2. MVI inversion parameters for regional inversions.

Inversion parameter	Value
Cell size	100 x 100 m; mesh and cell depths determined by software. Depths windowed to -2500 m in post-processing.
Topographic surface	Topographic grid (50 m resolution)
Regional level	5 km upward-continued field
Sensor elevation	35 m above the surface
Padding	Software default (5 cells)
Data error	Software default (5% of the standard deviation of the data)
IGRF value	B = 52920, I = 77°, D = 7.6°
IRI focus value	IRI = 1
Geological constraints	Not applied

Figure 4.12 presents a comparison of the MVI and magnetic susceptibility inversion results for two cross-sections (480000E and 483400E) from subarea #9. The susceptibility inversion shows distinct negative shapes or negative–positive pairs that may indicate remanent magnetization (MacLeod & Ellis

2013) (note: negative magnetic susceptibilities are not physically reasonable). Deeper negative features on profile 480000E may also indicate that the 'overall' regional field should be slightly adjusted sub-region by sub-region; however, this does not cause the sharp shallow negative features. The MVI magnitude values show sources with a positive magnitude (MVI values are always positive) and with shapes considerably different from the susceptibility inversion.

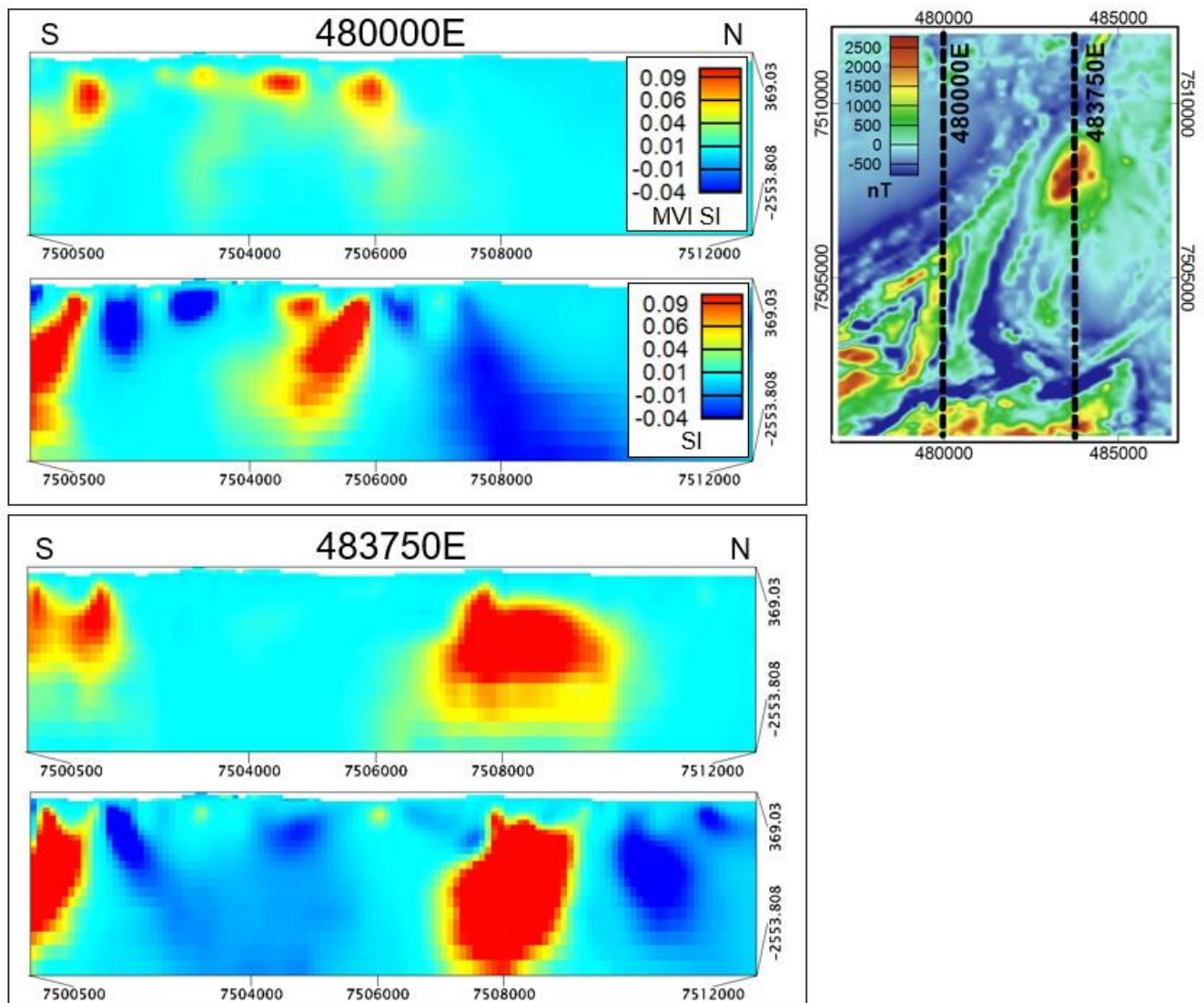


Figure 4.12. Comparison of MVI and magnetic susceptibility inversions (top and bottom panels, respectively) on two sections of sub-area #9 (see previous figure). Color scales are the same for all sections. On the right: section profile locations on the residual magnetic map.

Based on the comparison above, the MVI results seem physically more reliable. However, they should be validated against available geological or geophysical knowledge of the sub-areas. A recent detailed MVI inversion model was published from the Kevitsa intrusion by Fournier et al. (2020). They enhanced

the smoothness convergence of the total magnetization inversion with spherical coordinate transformation for calculational improvements. Comparison with their results across the remanence-bearing part of the intrusion (Fig. 4.13) shows that the regional MVI inversions performed in this project have roughly similar features, but the results are coarser, assumedly due to the level of detail in the inversion techniques and parameters and also the data/model resolution.

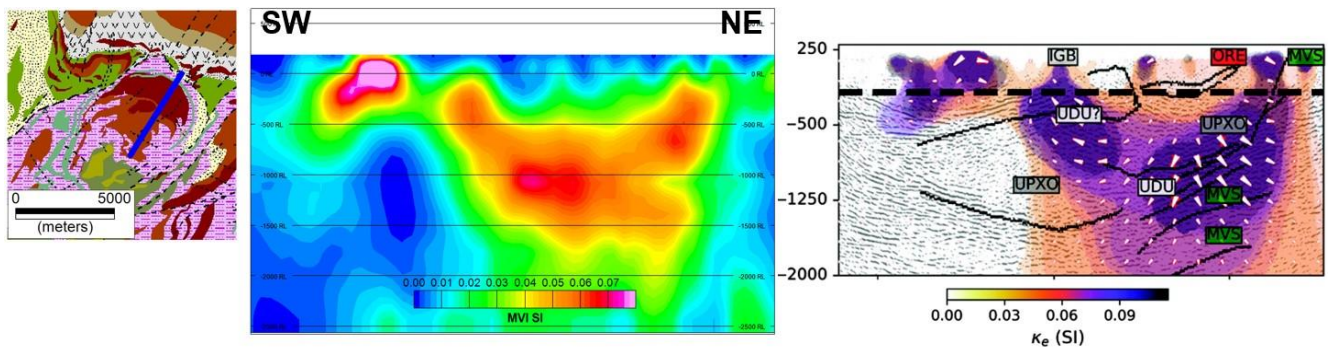


Figure 4.13. Comparison of the regional MVI inversion in this project (in the middle) with the spherical coordinate system MVI of Fournier et al. (2020) (on the right) on a profile across the Kevitsa intrusion (profile location shown on the left).

Gravimetric inversion for the Alaliesintie sub-area

The Alaliesintie seismic profile extends roughly in a NW direction across the Koitelainen intrusion and the Sodankylä and Salla group rocks north of Sodankylä town (Fig. 3.4). The gravity data in the area are sparse and the short wavelength content (i.e. local surface anomalies) is absent. To better include the sources resulting in long wavelengths on the borders of the model region, the gravimetric inversion was conducted on an extended 38 x 36 km area including the Alaliesintie sub-area (Fig. 4.14a–d).

The irregularly distributed gravimetric data were gridded and a 10 km upward-continued field was removed from the data as the regional field. The average station spacing of the data in the extended Alaliesintie area is 1.1 stations/km². The data were gridded with a 500-m cell size; this is also the lateral cell size for the inversion mesh. The depth of the mesh is 15 km with 36 cells; cell heights increase towards depth. The data fit error was set to 0.1 mgal after testing several values and a flat topographic surface of 225 m a.s.l. was used in all inversions (there is little variation in topography in relation to cell heights).

The petrophysical data (see chapter 3.1) were used to constrain the inversion. The Alaliesintie geological model (chapters 4.4 and 5.1) consists of seven modeled lithostratigraphic units: Archean basement, Sodankylä, Salla and Kuusamo groups, and Matarakoski and Sattasvaara formations (Fig. 4.14e). However, since these units are lithostratigraphic units, which means that they individually include variable lithologies, the units are not all easily expressed in terms of characteristic petrophysical value ranges. For this reason, and considering that all petrophysical data are collected from the surface, the geology-driven constraints are based on a simplified surface geology (Figure 4.14d). The

simplification rather closely follows the geological map (Bedrock of Finland – DigiKP). However, the smallest units have been merged with the surrounding unit (as they play little role in modeling) and some units of similar lithology have been merged. These will be called ‘lithological units’ to separate them from the lithostratigraphic units.

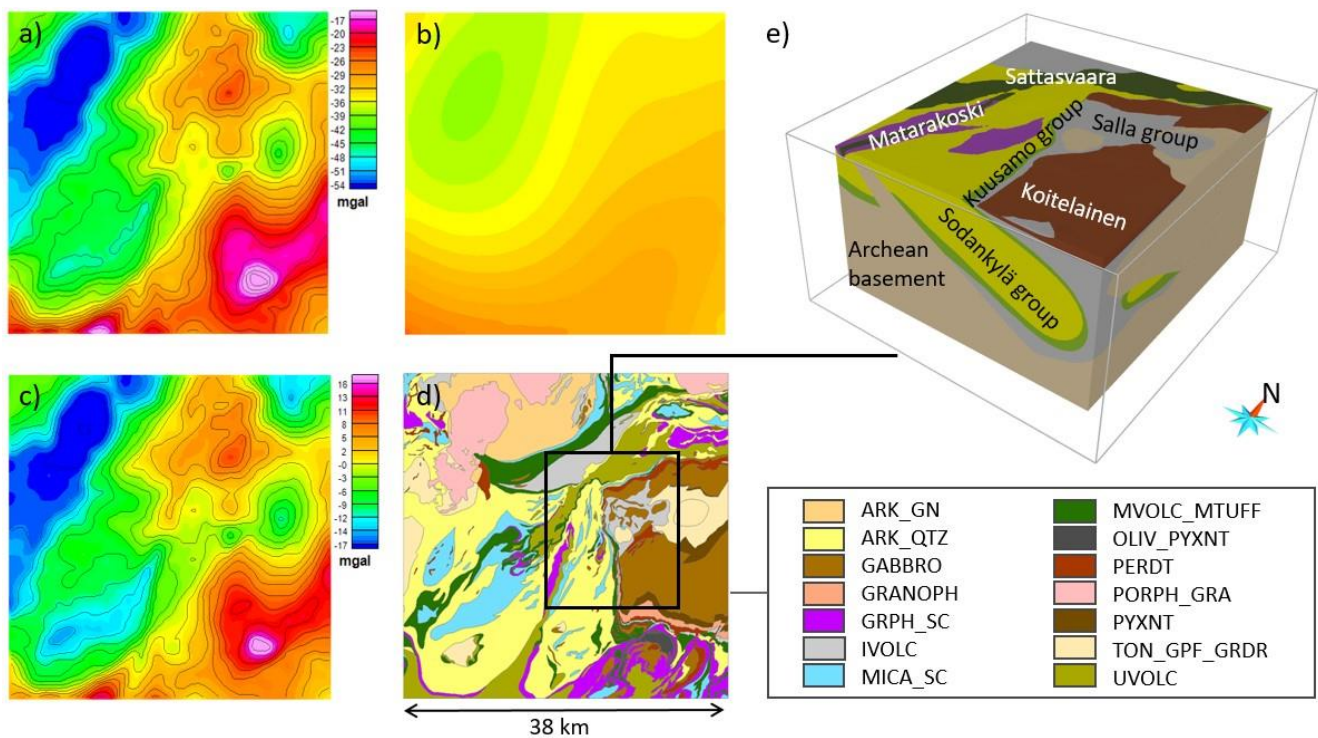


Figure 4.14. a) Bouguer anomaly, b) regional field, c) residual Bouguer anomaly, d) simplified bedrock map of the extended Alaliesintie area with the geological model area outlined, and e) initial geological model of the Alaliesintie area. Bedrock map legend: ARK_GN = arkose gneiss, ARK_QTZ = arkose quartzite, GABBRO = gabbro, GRANOPH = granophyre, GRPH_SC = graphite schist, IVOLC = intermediate volcanic rock, MICA_SC = mica schist, MVOLC_MTUFF = mafic volcanic rock / mafic tuff, OLIV_PYXNT = olivine pyroxenite, PERDT = peridotite, PORPH_GRA = porphyric granite, PYXNT = pyroxenite, TON_GPF_GRDR = Archean tonalite, porphyric granite, granodiorite, UVOLC = ultramafic volcanic rocks.

The first step of building the geology-driven inversion constraints is to formulate the linkage between the petrophysical data and the modeling units, i.e. characterize the units in terms of petrophysical value ranges. This requires finding a balance between the data scales and model unit homogeneities (Fig. 4.8 and related text).

Each petrophysical sample has been assigned a lithological attribute. These ‘field names’ are typically highly variable, as the data originate from three different sources and the naming conventions have not been harmonized. The field names also represent individual outcrops, whereas the lithological units on the bedrock maps (i.e. our modeling units) are generalizations; a unit may in reality be composed of various rock types that have been combined as an entity with a name label based on the majority rock type. For this reason, the petrophysical data were grouped based on their hosting

lithological modeling unit rather than outcrop lithology: each sample was assigned a lithological name based on its location on the bedrock map. This approach gives a realistic view of the petrophysical value ranges of the modeling units and removes the tedious task of harmonizing the field name lithologies. However, if the units are mixtures of various lithologies, the petrophysical value distributions will spread or be bi- or multimodal, and building constraints for the modeling units becomes ambiguous.

In the study area, the lithological modeling units can be fairly well characterized in terms of density, as shown by the density distributions in Figure 4.15 (distributions are presented as kernel density estimator (KDE) plots, the shape of which closely follows that of a histogram). However, it is also obvious that for some units, the density ranges are less clearly defined. These units display multi-peaked distributions indicating a heterogeneous source. This is likely due to inaccuracy of the unit boundaries (samples near the boundary should belong to another unit) or complexity of the internal geology (several different lithologies simplified into one unit or rock composition varies within the lithological class). The multi-peaked distribution may also be due to alteration. Most clearly, this applies to peridotites (class PERDT in Fig. 4.15b), which have a high-density peak at 3000 kg/m^3 and another lower-density peak at ca. 2800 kg/m^3 ; the latter strongly corresponds with the density of the samples with the field name 'serpentinite' (circle symbol in Fig. 4.15b). Serpentinization typically lowers the density of the rock and petrophysically this modeling unit is thus clearly divided into altered and nonaltered rocks. However, due to time constraints, the multimodal classes could not be further separated.

Magnetic susceptibilities (Fig. 4.15e–h) display a wide spread of values in most of the lithological model units. Most notably, almost all units have a substantial proportion of ferromagnetic samples (magnetic susceptibility $> \text{ca. } 2000 \times 10^{-6} \text{ SI}$); these rocks are the main source of magnetic anomalies on magnetic maps. Ultramafic rocks (olivine pyroxenites, peridotites, and ultramafic volcanic rocks) are mostly ferromagnetic, whereas schist rocks are mostly paramagnetic (magnetic susceptibility $< \text{ca. } 2000 \times 10^{-6} \text{ SI}$).



Figure 4.15. Density (a–d) and magnetic susceptibility vs density (e–h) distributions of the extended Alaliesintie area rocks. Vertical lines in a–d denote median values for each distribution. ARK_GN = arkose gneiss, ARK_QZT = arkose quartzite, GABBRO = gabbro, GRANOPH = granophyre, GRPH_SC = graphite schist, IVOLC = intermediate volcanic rock, MICA_SC = mica schist, MVOLC_MTUFF = mafic volcanic rock / mafic tuff, OLIV_PYXNT = olivine pyroxenite, PERDT = peridotite, PORPH_GRA = porphyric granite, PYXNT = pyroxenite, TON_GPF_GRDR = Archean tonalite, porphyric granite, granodiorite, UVOLC = ultramafic volcanic rocks.

It should be noted that in the initial geological model (Fig. 4.14e), the two major lithostratigraphic units, the Archean basement (represented by class TON_GPF_GRDR in Figure 4.) and the Sodankylä group (class ARK_QTZ), both have their main peak close to the value of 2600 kg/m³; the density difference between these units is small. Therefore, these units probably cannot be well distinguished from each other in gravimetric modeling. The lithostratigraphic modeling unit Koitelainen is heterogeneous in density, as it contains gabbro (GABBRO), granophyre (GRANOPH), and peridotite (PERDT) rocks. The Salla and Matarakoski modeling units are diverse in terms of lithologies, and thus not easily characterized by definite density ranges. The Sattasvaara unit is represented by the class UVOLC with a fairly clear density distribution, albeit slightly skewed towards smaller densities.

As the link between petrophysics and geology is built between the surface petrophysics and bedrock map, we can only constrain the inversion on the top cells of the mesh, i.e. shallow depths, where we can assume our constraint data to be valid. The constraints are limited to the two top subsurface cell layers of the mesh, which extend to a depth of 325 m. With the use of geological constraints at shallow depths, the smoothness and depth attenuation terms built in the algorithm should also increase the geological reliability at deeper depths, even though the constraints are not applied there.

The sample densities were transformed to relative densities (as required by the inversion algorithm) by using a reference value of 2800 kg/m³ (several values were tested according to the procedures described by Williams (2008, p. 131)). The relative density values were used to construct three different constraint models:

1. Reference model #1: On the surface layer of the mesh, the density value of every cell is the average of petrophysical samples within 500 m radius of the cell center (Figure 4.16a). The surface layer is then copied to the layer below it to cover the top 325 m of the mesh. A zero value is assigned to cells for which no petrophysical samples are within the search radius and to all layers below the top two. This layer is then copied to the second layer of the mesh. Note that this model is purely based on measured petrophysical data, but the data are not available for all top layer cells.
2. Reference model #2: The previous reference model is complemented on the top two layers by assigning the cells that contain no data within the search distance the median density value of their lithological modeling unit (Fig. 4.16b). The median values of the lithological modeling units are listed in Figure 4.15. This reference model thus combines measured petrophysical data and density characterizations of the lithological units and provides a completely filled model for the top layer cells.
3. Bounds constraint model (Fig. 4.17): On the surface layer of the mesh, for each cell with a minimum of three petrophysical samples within the cell, the minimum and maximum densities of these samples are used as the minimum and maximum boundary values for the cell. For

other cells, the minimum and maximum boundaries are set to estimated values based on the density distribution of the cell's lithological model unit. The surface layer is then copied to the second layer of the mesh. This model also combines measured petrophysical data and density characterizations of lithological units, as did reference model #2.

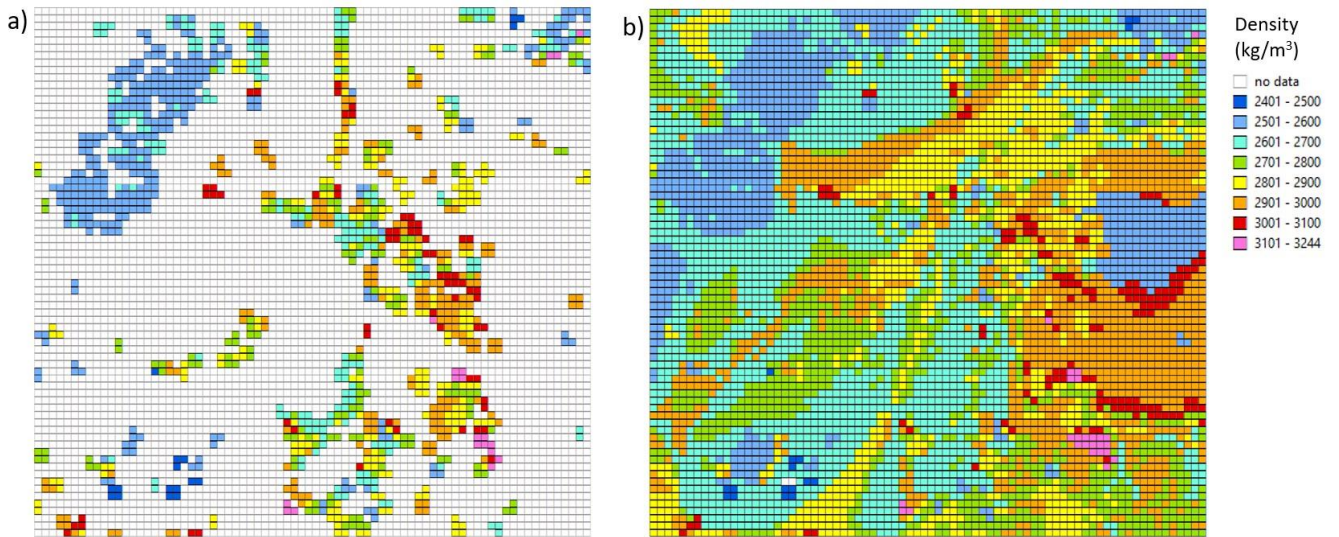


Figure 4.16. a) Top mesh layer with petrophysical sample density averages calculated for cells with samples within 500 m radius of the cell center; b) the same as a) but with empty cells filled with the median density value of the cell's lithological model unit.

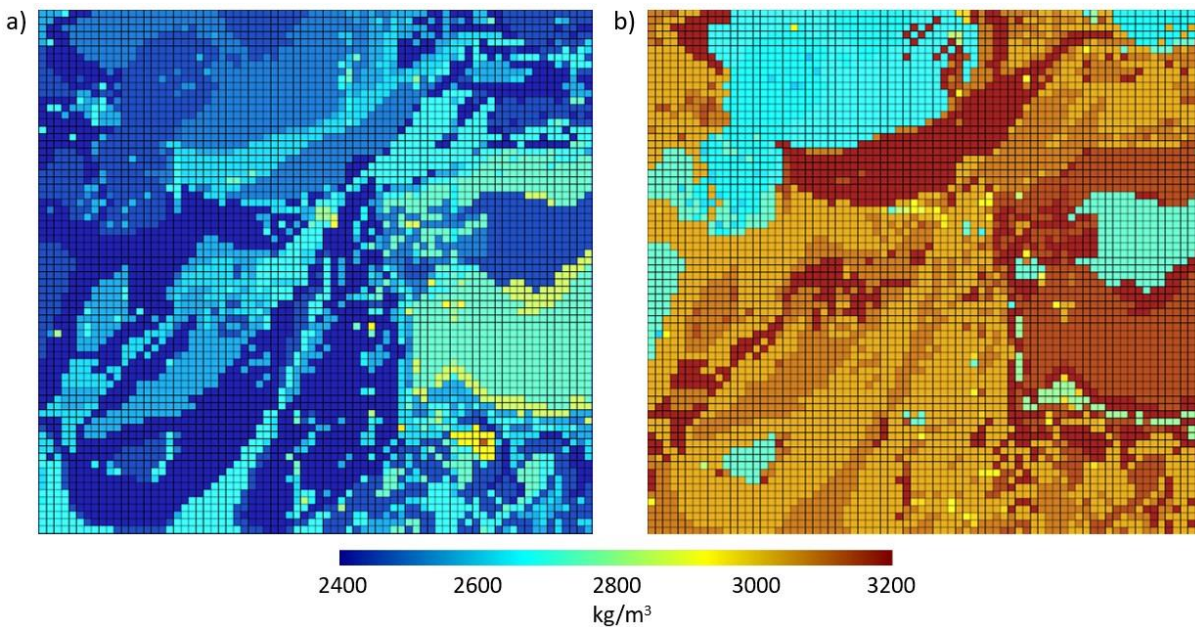


Figure 4.17. a) Lower and b) upper boundary constraints shown for the top layer of the mesh.

To compare the effect of constraints and other control parameters, we present a comparison of four inversions:

- 1) INV1: Geologically unconstrained inversion run with default parameters.
- 2) INV2: Inversion with reference model #1 applied.
- 3) INV3: Inversion with reference model #2 applied. For this inversion, the parameters L_e , L_n , L_z controlling the relative importance of smallness/smoothness were adjusted to 2x cell size (for L_z , 2x the smallest cell size) (cf. UBC-GIF (2005) and Williams (2008)). An additional weighting model was also applied to weight the cells of reference model #2 (note that for Grav3D, the weighting model must be manually added into the control files if using the standard graphical user interface):
 - a. For cells with a density value based on the lithological unit's median density, the smallness weight w_s values are increased from the default value $w_s = 1$ to values of $w_s = 1-3$ based on a subjective reliability estimate. w_s control the relative closeness of the recovered model to the reference model and should be increased when confidence in the reference model is high (UBC-GIF 2005).
 - b. For cells with a density value based on the sample average, the smallness weight w_s values are increased from the default value $w_s = 1$ to values of $w_s = 15-50$ based on the number of sample points within the cell.
 - c. The directional smoothness weights w_n , w_e are set to a value of 2 (default: 1) in order to enforce more lateral smoothness in the reference model. The vertical smoothness weight w_z is left at the default value.
- 4) INV4: Bounds constraint model with a zero (default) reference model applied and the L -parameters adjusted as previously. (The compression error value was also lowered to 0.025).

In all inversions, the misfit values were monitored to ensure a good data fit.

On the EW profile 7515577N, the recovered models from INV1 (Fig. 4.18b) and INV2 (Fig. 4.18c) are in accordance with each other. This is due to the fact that reference model #1 is quite sparse and does not have a significant constraining effect on the recovered model.

The recovered model from INV3 follows the high-contrast reference model quite faithfully in the top layers, where the reference model is valid (Fig. 4.18d). As discussed earlier, the recovered model may deviate from the reference model, and it seems intuitive that by enforcing more smoothness in the inversion, any abrupt value changes between adjacent cells of the reference model should be avoided in the recovered model if so desired. However, GRAV3D v3.0 implements the smoothness conditions as *smooth model difference* rather than *smooth model* (Williams 2008): the deviations between the reference model and the observed model, rather than the observed model itself, are kept smooth. This may still result – as seen here – in sharp value variations between adjacent cells in the recovered model if such variations are present in the reference model.

The newer version (v4.0) of the software should have more options to control the smoothness behavior. With the v3.0 software, Williams (2008) suggests the use of bounds constraints with a zero reference model to mimic the smooth model option. In this way, the values in the recovered model cells are restricted to certain value ranges, but the abrupt property changes between near cells are avoided. The recovered model from INV4 (Fig. 4.18e) does provide a smooth model, but with better-defined sources than the unconstrained and petrophysically constrained inversions.

On profile 7515577N, the highest densities in all recovered models are related to the ultramafic volcanic rocks (marked 1 in Figure 4.18) and the western margin of the Koitelainen intrusion (2). The ultramafic rocks are consistently presented on all inversion versions and the lithostratigraphic model (Fig. 4.18f) is in accordance with the shallow depth of these rocks. The Koitelainen intrusion is interpreted in the geological model to be very shallow, and the deeper-plunging high-density body could be related to the mafic volcanic rocks of the Kuusamo group that envelope the arkose quartzites (Sodankylä group). In this case, the Kuusamo unit could be thicker than presented in the lithostratigraphic model. Another alternative is that there is a hidden high-density source below the Koitelainen intrusion. The dip directions of the gravity inversions and the lithostratigraphic model are generally in accordance with each other.

Profile 7523000N (Fig. 4.19) crosses the Sattasvaara ultramafic volcanites (marked as 1 in the figure), the undefined gabbros (2) within the Salla group and the Tojottamaselkä Archean tonalite. The volcanic rocks are best defined in the INV4 inversion (Fig. 4.19e) and the gabbros in the INV3 (Fig. 4.19d) and INV4 (Fig. 4.19e) models. Based on the inversions, the Sattasvaara rocks extend slightly deeper than in the lithostratigraphic model (Fig. 4.19f); the gabbros seem quite shallow (<2 km), but are not included in the geological model. The porphyric granite within the Tojottamaselkä tonalite shows as a distinctly low-density shape in all inversions. As discussed previously, the density difference between the Archean basement and the Sodankylä group quartzites is small, and these two units will not therefore be well distinguished from each other in the inversion. However, the true density of this porphyric granite unit is unknown, as it has not been sampled and may be lower than for other Archean rocks.

Profile 496000E (Fig. 4.20) crosses the Kevitsa and Koitelainen intrusions and Sattasvaara ultramafic volcanic rocks. The high-density Kevitsa intrusion is clearly visible in all inversions but seems most compact in the INV4 model (Fig. 4.20e). The small peridotite section of the Koitelainen intrusion (marked as 1 in the figure) and the undefined gabbros (2) within the Salla group rocks appear as shallow high-density bodies. A small Archean granitoid between them is quite well defined in the INV3 and INV4 models (Figs 4.20d–e). In comparison to the lithostratigraphic model (Fig. 4.20f), the contacts between the Archean rock and the gabbros are steeper in the inversions, although the depths are well matched.

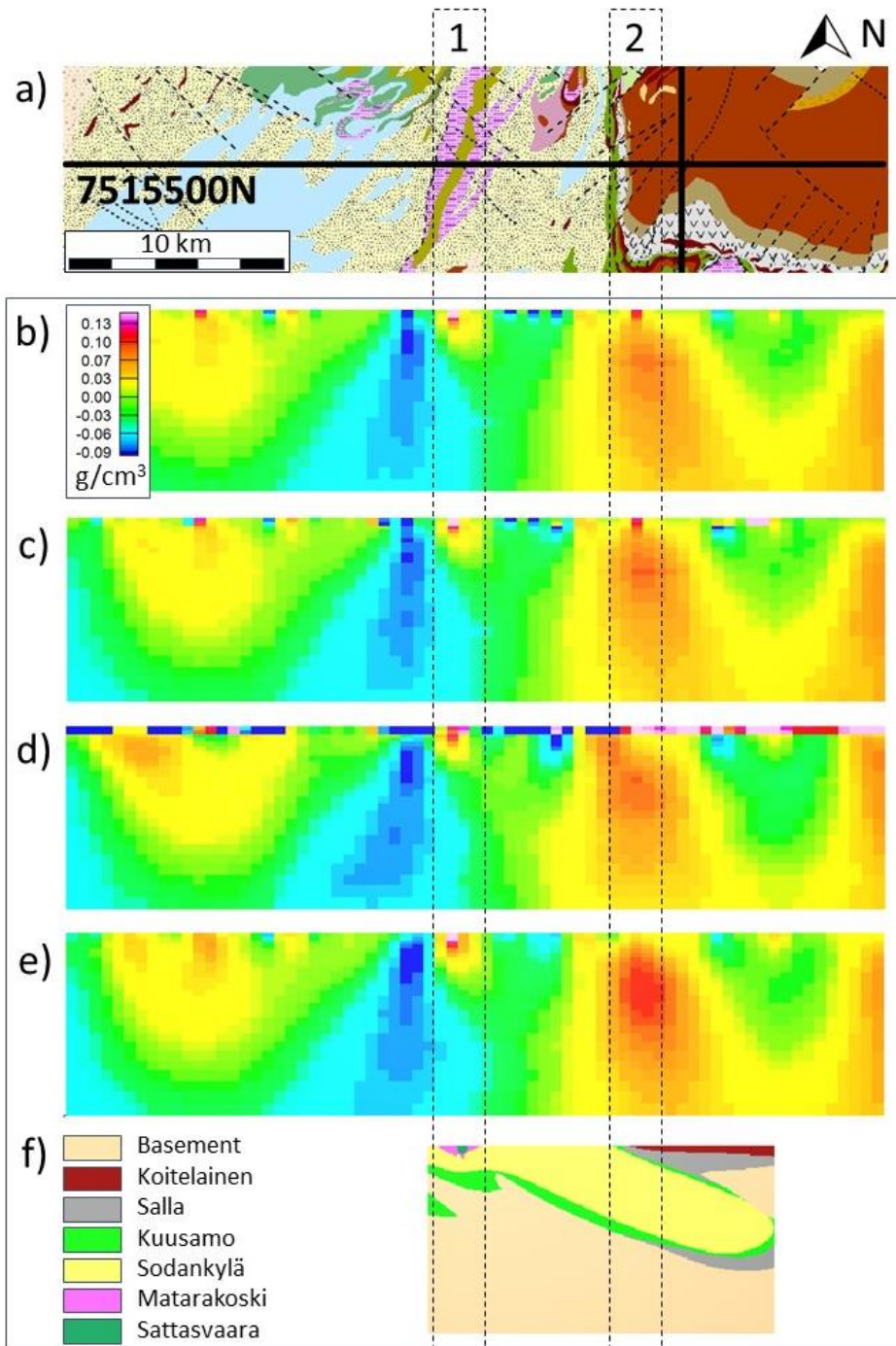


Figure 4.18. Comparison of gravimetric inversion results and the geological data/model on profile 7515500N. a) Plan view of the geological map, b) vertical section of the recovered model of inversion INV1, c) INV2, d) INV3, e) INV4, f) lithostratigraphic model. Details 1, 2 discussed in the text.

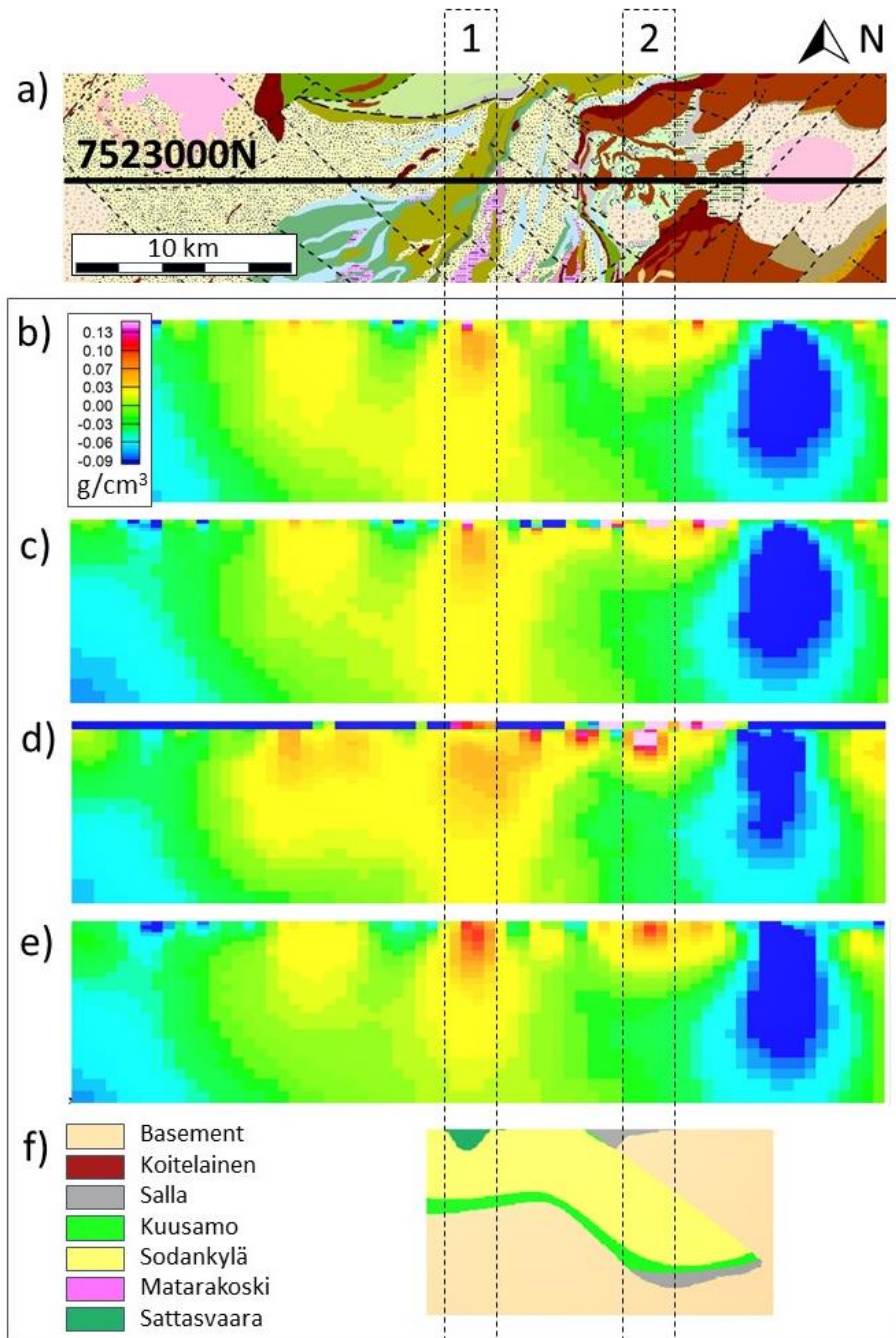


Figure 4.19. Comparison of gravimetric inversion results and the geological data/model on profile 7523000N. a) Plan view of the geological map, b) vertical section of the recovered model of inversion INV1, c) INV2, d) INV3, d) INV4, f) lithostratigraphic model. Details 1, 2 discussed in the text.

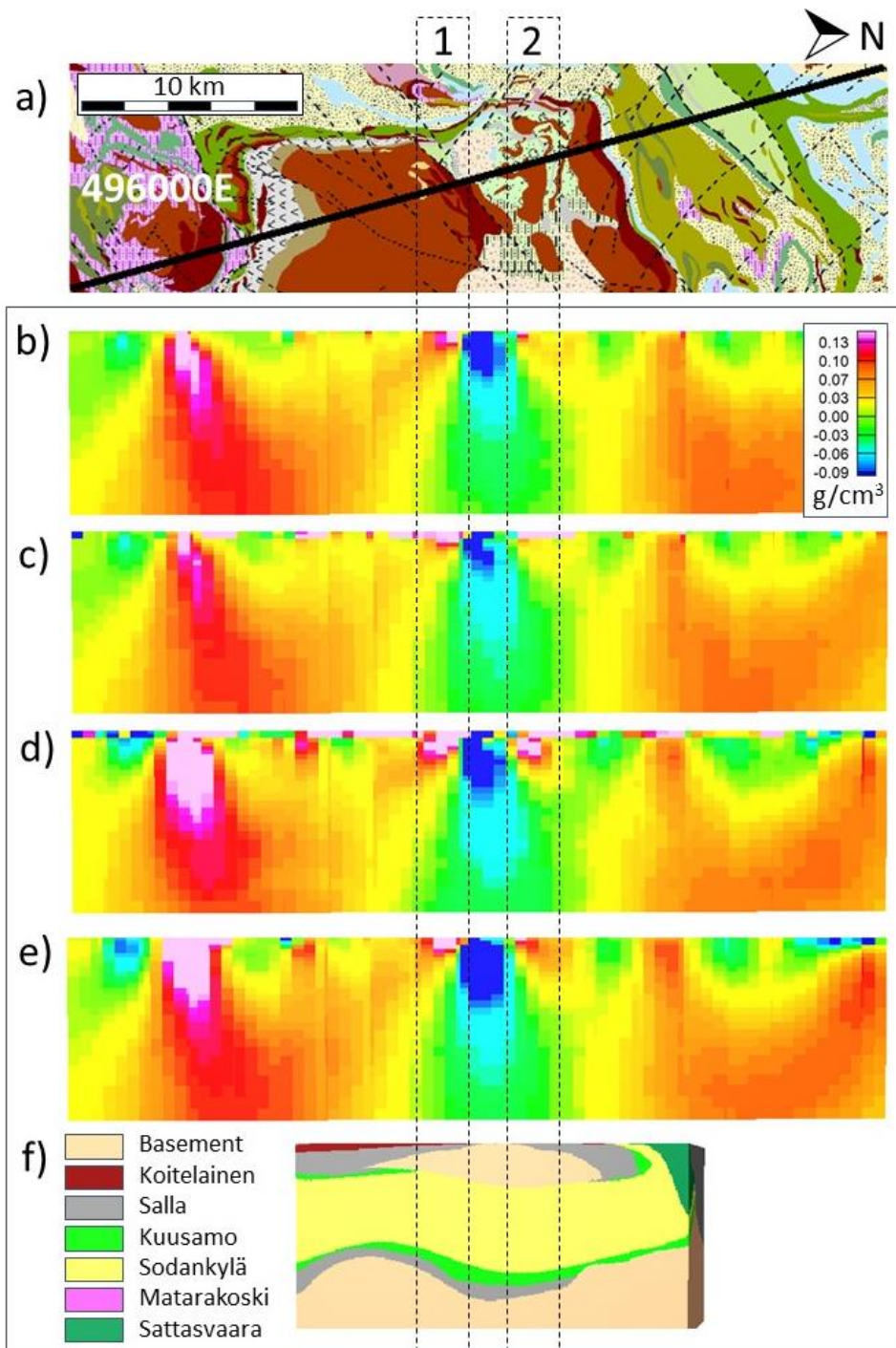


Figure 4.20 Comparison of gravimetric inversion results and the geological data/model on profile 496000N. a) Plan view of the geological map, b) vertical section of the recovered model of inversion INV1, c) INV2, d) INV3, e) INV4, f) lithostratigraphic model. Details 1, 2 discussed in the text.

4.4 AMT inversions

1D and 2D inversions were carried out for the AMT data acquired prior to the project in 2017–2018. Unfortunately, satisfactory RMS errors were not achieved for 2D inversion results. Usually, this problem occurs when 3D sources are modeled with 2D inversion. In many cases, however, 1D inversion of various averages of AMT impedance tensor data can be useful in such 3D cases. The results presented here are 1D inversions of the determinant average of the impedance tensor.

Pseudosections obtained with 1D models are presented in Figure 4.21. The results are visualized along two projection profiles shown in Figure 3.3a. Blank areas in pseudosections are due to limited sensitivity of the EM fields below good conductors that cause fast field attenuation. For resistive areas, in turn, natural EM fields reach greater depths, providing much deeper information.

Combining various geophysical modeling results that reflect different petrophysical properties is a useful approach to support geological modeling. As an example, Figure 4.22 shows an integrated reflection seismic and AMT electrical conductivity section along profile 1.

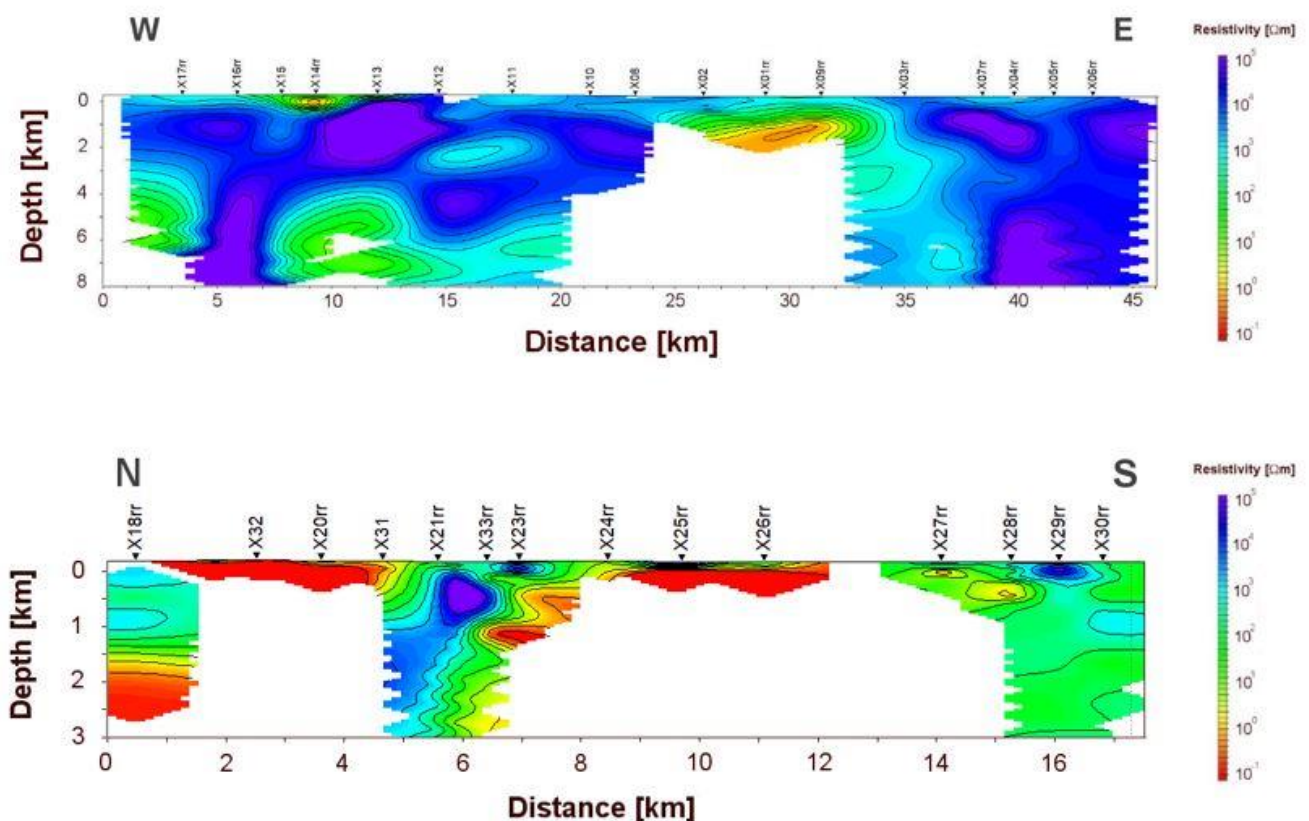


Figure 4.21. 1D inversion model pseudosections along Profiles 1 (upper panel) and 2 (lower panel).

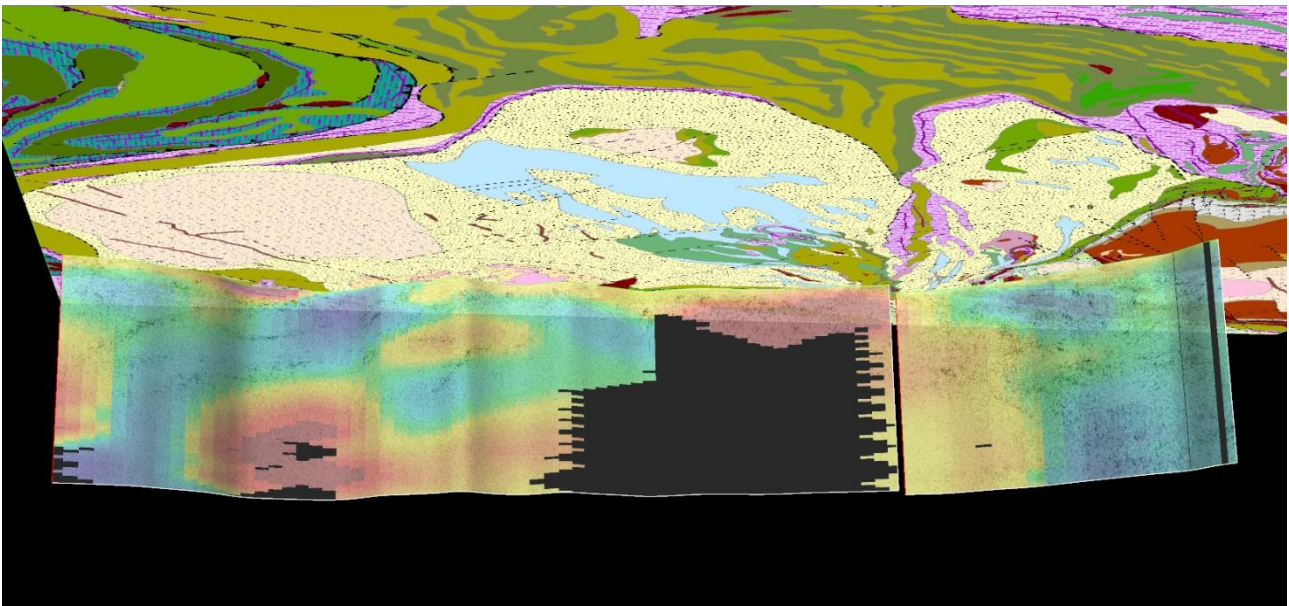


Figure 4.22. Integrated reflection seismic and AMT electrical conductivity section along the Pomokaira profile (Profile 1). View from the south.

4.5 3D GEOMODELING

3D modeling includes data visualization, interpretation, and model production. It is required that a model is in harmony with existing data, but it is almost equally important to consider geological evolution during the construction of a regional-scale model. Diamond drill or other direct sampling material from the bedrock are sparsely, if at all, available for geomodeling and regional geomodels are typically almost solely based on geophysical data and bedrock maps. Furthermore, geological maps in Finland are largely based on the interpretation of aerogeophysical data. For this reason, regional scale modeling requires consultation and interpretation with experts of different specialties and a careful review of earlier geological interpretations. Finally, the model itself can be regarded as an interpretation of past geological processes instead of a detailed representation of the subsurface.

The 3D modeling focused on the regional scale, covering an area of 53 × 42 km. The Alaliesi subarea (17 × 15.5 km) was extracted from the regional-scale model for the iterative constrained inversion work and model optimization. The Alaliesi subarea was chosen due to its diverse geology. The area represents a section of the stratigraphically lowermost units of the 2.45–2.0 Ga CLGB and is located in the proximity of exposed Archean basement and in the 2.45 Ga Koitelainen layered intrusion. Based on the current geological maps, the Archean basement rocks are exposed in the central part of the intrusion. This feature has been interpreted to be due to a basement dome at the footwall of the sheet-like intrusion. In contrast with this large-scale lateral geological feature, the supracrustal rocks appear to be more tightly folded and N–S and NE–SW trending. Thus, the area provided a structurally very interesting target to test the workflow of this project.

The 3D modeling was carried out with the program SKUA-GOCAD® version 17 in the Paradigm® software of Emerson Electric Co. The modeling with this program is performed in stages, from surfaces to sealed volumes and finally to a voxel. A 3D model is typically constructed from a set of horizon and fault surfaces representing the interpreted structure of the modeling area. Sealed volumes are defined by surfaces that individually share points along each contact with another surface. A sealed-volume structural model is also known as a Model3d object. A voxel is a grid of cells where each cell includes attribute data (Fig. 4.23). For example, the cell size of the Alaliesi 3D voxel model was 50 × 50 × 50 m.

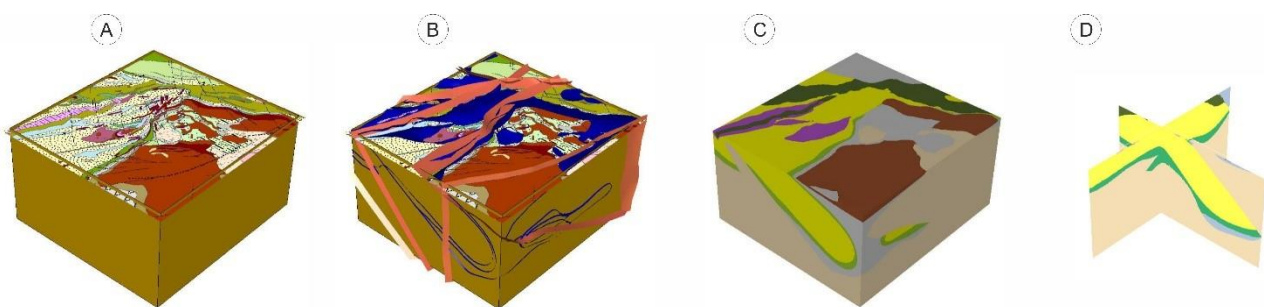


Figure 4.23. A 3D model of a modeling area (A) is constructed from surfaces (B) to form a sealed-volume structural model (C), and finally a voxel model. The attribute data of a voxel model can be visualized with sections (D).

4.6 Prospectivity modeling

Mineral prospectivity modeling is used to delineate favorable areas for a mineral deposit type of interest. Geographical information systems (GIS) provide a platform with many applications to integrate digital map data into a prospectivity map that delineates the mineral potential of a target area. Prospectivity mapping can be divided into two main approaches: conceptual (knowledge-driven) and empirical (data-driven) methods (Bonham-Carter 1994). Empirical methods require a considerable number of known examples of mineral deposits to be applicable, whereas conceptual methods can be used without any prior knowledge of mineral deposits. Conceptual methods include fuzzy logic, decision-tree approaches, and evidential belief functions (Carranza 2008). Empirical models, in turn, include weights-of-evidence, logistic regression, and artificial neural network techniques (Bonham-Carter 1994). In some cases, a combination of empirical and conceptual approaches has also been used (e.g. Porwal et al. 2004, 2006; Nykänen et al. 2008). The prospectivity modeling workflow (Fig. 4.24) consists of five main steps: 1. selection of an appropriate mineral system model, 2. selection of relevant datasets, 3. preprocessing, 4. data integration, and 5. validation of the results. The workflow is also iterative and, should the validation require it, one can easily go back into any stage for optimization of the results.

The selection of a relevant mineral system model is the key step, as the model defines the critical parameters needed to construct the prospectivity model. Mineral system models can be conceptual,

process-based, empirical, or a combination of these (Hronsky & Groves 2008). A classical mineral system model includes a description of the geological aspects of ore genesis that can be used to constrain the data and various derivatives that in turn are used as proxies for different aspects of the mineral system. These typically include: a) sources of metals, ligands, fluids and heat, b) transport channels or conduits, c) chemical, physical, or mechanical traps, d) deposition, and e) preservation (Wyborn et al. 1994; Knox-Robinson & Wyborn 1997; McCuaig et al. 2010; Kreuzer et al. 2015).

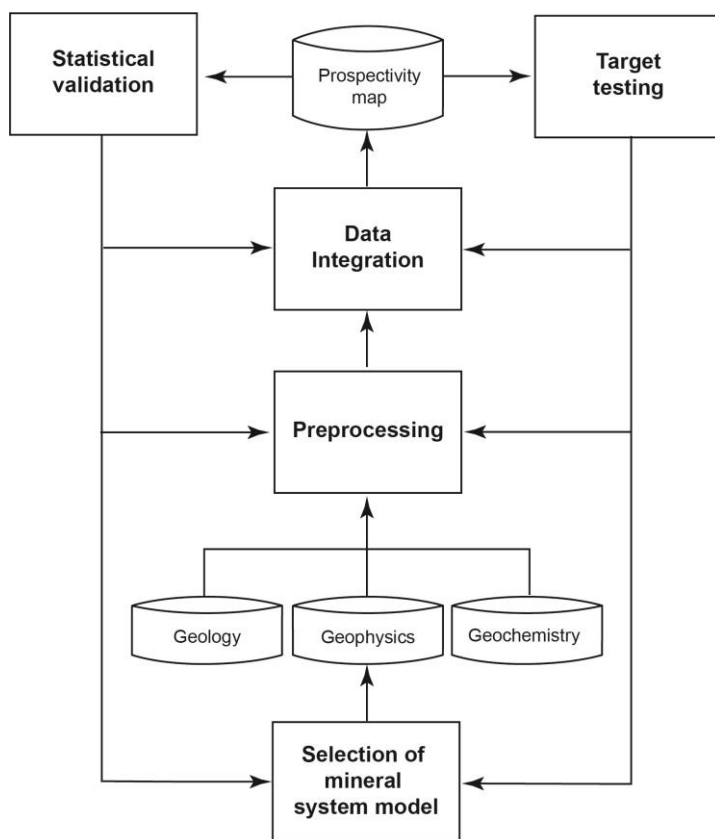


Figure 4.24. Prospectivity modeling workflow. Modified after Nykänen (2007).

The second step in prospectivity modeling is the selection of the datasets, or their derivatives, that are used as proxies of different aspects of the mineral system worked on. The pre-processing stage, the third step, involves various processing techniques for processing the raw data in order to extract or derive the input patterns representing proxies for critical parameters of the mineral system. The techniques involved include image processing, interpolation, raster calculation, data clustering, and classification, depending on the data and input layer needed. One of the key operations in preparing data for the data integration phase is to rescale all the input layers to a common scale, e.g. 0 to 1. The pre-processed data are integrated into the final prospectivity map in the data integration step. The approach used depends on the availability of training sites, i.e. known deposits. The last stage in the

process is model validation. This can be done either by statistical methods or direct exploration. In practice, it is reasonable to always carry out statistical validation if possible. The validation method depends on the modeling technique used and the amount of available validation data (e.g. Nykänen 2008).

In the XL3D project, prospectivity maps were generated for two deposit types: orogenic gold and magmatic Ni–Cu deposits. The data used in the models consisted of GTK’s geophysical, geochemical, and geological datasets described in chapter 3. For both of these models, the conceptual approach was selected and the fuzzy logic method was applied in final data integration. For Ni–Cu deposits, there are only four known deposits and prospects, thus ruling out the empirical methods. The situation with gold deposits is somewhat better, as there are a total of 25 known deposits and prospects within the study area. However, as with the Ni–Cu model, a conceptual approach was selected for the gold model.

4.6.1 Orogenic gold prospectivity model

A conceptual mineral system model for orogenic gold deposits by Groves et al. (1998), McCuaig and Kerrich (1998), Goldfarb et al. (2001), Groves et al. (2003), and Groves et al. (2020) was used in generating the prospectivity model. A particular local feature of the CLGB is that in a number of known orogenic gold deposits, base metals, especially copper, occur in elevated concentrations with the gold (e.g. Eilu et al. 2008). Therefore, the model was adjusted accordingly.

Table 4.3. Exploration criteria and input data.

Exploration criteria	Data set	Derived data set
Sulfides present	Regional till geochemistry 1 sample per 4 km ²	Interpolated grids (kriging) Cu, Co, Fe
Au mineralization present	Regional till geochemistry 1 sample per 4 km ²	Interpolated grids (kriging) Te
Proximity to Au indications	Regional till geochemistry 1 sample per 4 km ²	Proximity to Au anomaly
Structural control, pathway & trap	Regional gravity, 1–4 observation per km ²	Proximity to gravity worms
Structural control, pathway & trap	Updated bedrock map	Proximity to structures
Lithological control, trap	Bedrock map	Categorical grid, lithological favorability
Metamorphic control, trap	Bedrock map	Categorical grid, metamorphic favorability
Graphite-bearing units, trap	Low altitude EM in-phase	Interpolated grid (spline), conductors

The datasets used in the gold model consisted of till geochemistry (Cu, Co, Fe, Te, Au), bedrock map data (lithology, metamorphism, structures), airborne geophysics (EM real component), and regional gravity data (gravity worms), and each of these datasets represented proxies for the mineral system model (Table 4.3). The Cu, Co, Fe, and Te till data were interpolated to grids using the kriging method. These elements represent the geochemical signature of the orogenic gold deposits. The till data on gold were problematic. For the sample population of 1072, the average gold grade was 3.3 ppb, the

median value 1.7 ppb, the 75th percentile value 3.3 ppb, and the maximum value 103 ppb, indicating highly skewed and nuggety data for which regular interpolation does not produce good results. Instead, the 95th percentile (>10.5 ppb Au) samples were selected as gold indications and the Euclidian distance to a layer of them was calculated for them as a proxy. Gradient maxima or “worms” were extracted from the gravity data using a multiscale edge detection system (Hornby et al. 1999). Proximity rasters for the gravity worms were generated as a proxy for structural control on gold mineralization. Gold deposits typically contain low volumes of sulfides, and they do not therefore respond to EM methods. Graphite-bearing rocks, however, are potential chemical traps, and a number of the known gold deposits in the CLGB are hosted by graphite-bearing sedimentary and volcanoclastic rocks (e.g. Eilu et al. 2007). Highly conductive zones on EM maps are known to be linked to graphite-bearing lithological units in northern Finland (e.g. Hyvönen et al. 2013). Therefore, highly conductive zones on the EM real phase map were used as a proxy for potential graphite-bearing chemical traps. Lithological units and structural data were used from the bedrock map (Bedrock of Finland – DigiKp). Of these, structural data consisting of shear and fault zones were modified using the 3D model generated in this work. A proximity raster to gold-controlling structures was generated from this data. The lithological map was processed to a categorical grid whereby the lithologies were ranked based on expert estimates for different lithologies to act as traps for orogenic gold deposits. The highest ranking was given to komatiites, tholeiitic basalts, phyllites, and dolerites, whereas the lowest rank was given to TTG gneisses, granitic intrusions, and migmatites. The metamorphic map (Hölttä & Heilimo 2017) was also processed to a categorical grid. Zones with peak metamorphic facies of greenschist facies were ranked highest and the higher metamorphic facies zones were ranked with lower values, the zones with upper amphibolite facies being ranked with the lowest value.

Each of the generated evidential layers was rescaled to a common scale (0 to 1). The rescaling was performed using a fuzzy membership function (Tsoukalas & Uhrig, 1997):

$$\mu(x) = 1/(1 + (x/f_2)^{-f_1})$$

where f_1 = spread (between 1 and 10), and f_2 = midpoint (between the min and max of the input data). The spread parameter defines the steepness of the function and the midpoint the fuzzy membership value of 0.5 within the input data range. The midpoint and spread values used are presented in Table 4.4. The mean values for geochemical layers and EM real data were used as the midpoint. In proximity layers, the mean values were selected by expert opinion. Half the distance between sample points (1000 m) was used as a midpoint for the proximity to an Au indication layer. Expert opinion was used for other proximity layers. For both proximity to structures and proximity to worm layers, a midpoint value of 1500 m was applied. Spread values between 2 and 5 were used. Negative (ascending) spread values were given to layers for which low values are favorable and positive (descending) values to layers where high values are favorable. For categorical layers, the values varied between 0.1 and 0.9.

Table 4.4. Midpoint and spread values used in preprocessing the evidential data sets

Data layer	Midpoint	Spread
Au indications	1000 m	-3
Co in till	20 ppm	5
Cu in till	61 ppm	3
Fe in till	3.40%	4
Te in till	24 ppb	3
EM in phase	0 ppm	4
Gravity worms	1500 m	-2
Structures	1500 m	-2

Categorical classification was used for lithological and metamorphic maps.

The rescaled evidential layers were integrated using fuzzy AND and fuzzy GAMMA operators in accordance with the fuzzy flow chart in Figure 4.25. The fuzzy AND operator is similar to the Boolean AND operator. The fuzzy GAMMA operator is a combination of “fuzzy algebraic sum” and “fuzzy algebraic product” operators (Bonham-Carter 1994).

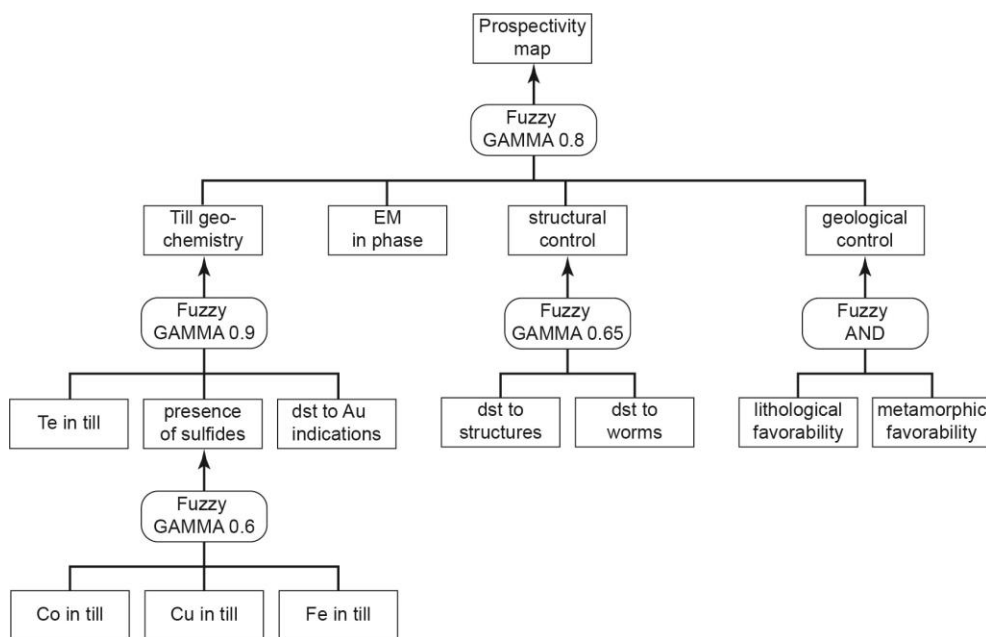


Figure 4.25. Fuzzy logic model flow chart.

In the first phase, the Co, Cu, and Fe of till data were integrated using the fuzzy GAMMA operator into a layer indicating the presence of sulfides, and this layer was subsequently integrated with Te in till and Au indication evidential layers using the fuzzy GAMMA operator (Fig. 4.26). The intermediate prospectivity maps “geological control” and “structural control” were integrated using fuzzy AND and fuzzy GAMMA operators, respectively (Fig. 4.27). The final orogenic gold prospectivity map was

generated by integrating the intermediate maps with the pre-processed EM real component map using the fuzzy GAMMA operator (Fig. 4.28).

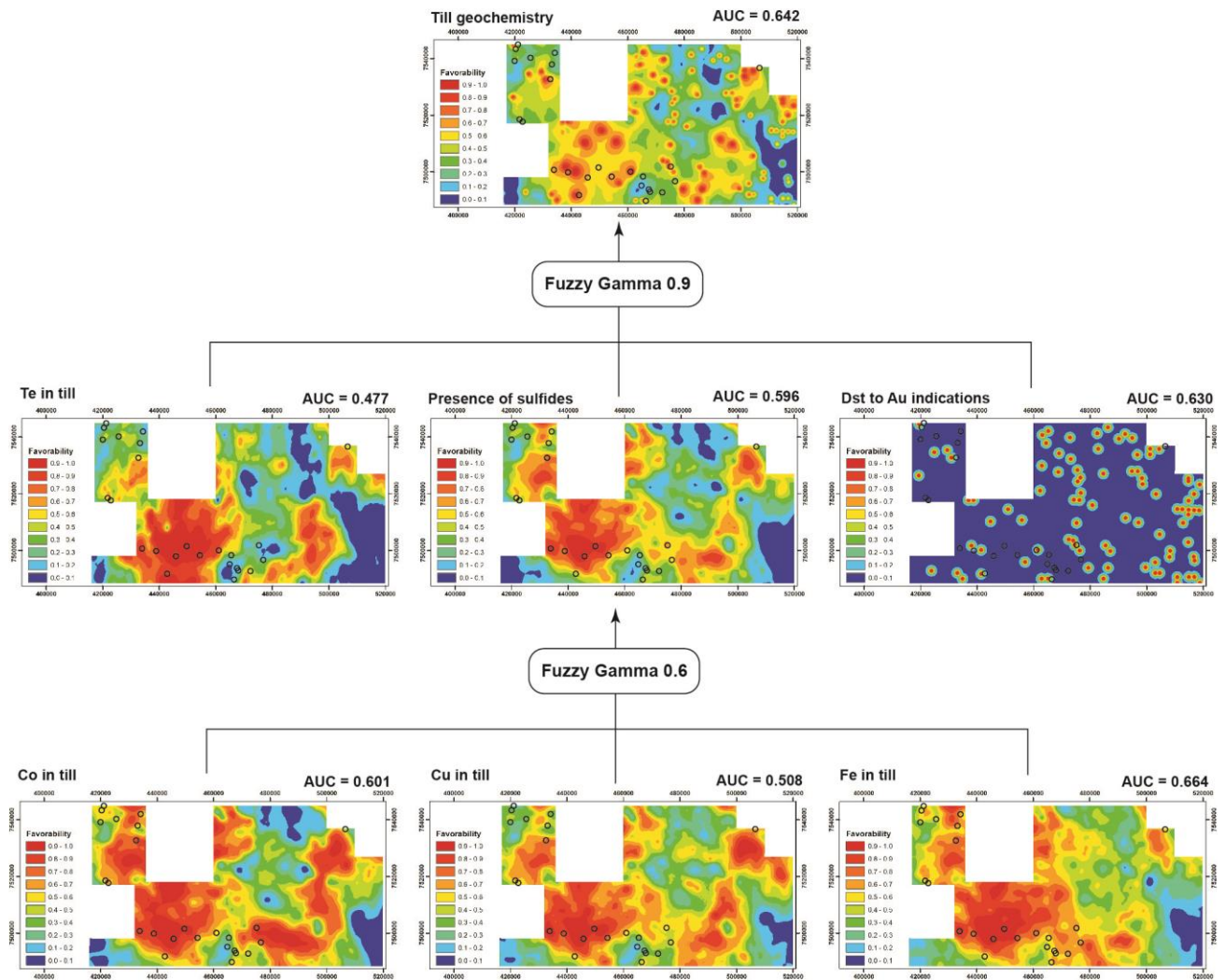


Figure 4.26. Integration of till geochemistry intermediate prospectivity maps from pre-processed evidential layers. Black circles indicate the location of known gold deposits and prospects. AUC values indicate the calculated AUC value of each layer (see text).

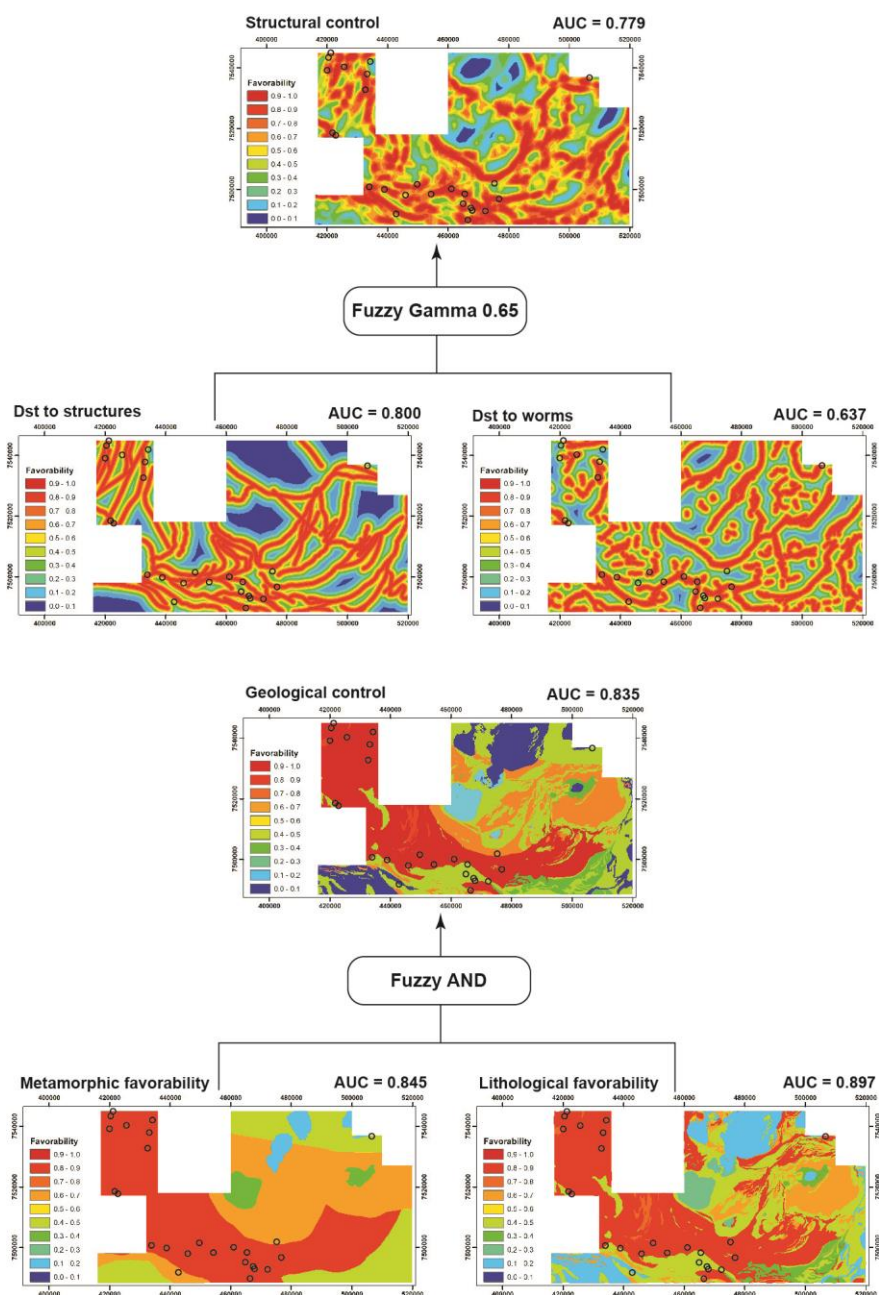


Figure 4.27. Integration of geological and structural control intermediate prospectivity maps. Black circles indicate the location of known gold deposits and prospects. AUC values indicate the calculated AUC value of each layer (see text).

The final orogenic gold prospectivity map was validated using the receiver operating characteristics (ROC) technique (Obuchowski 2003; Fawcett 2006). This is a proven method for spatial predictive model validation (e.g. Robinson and Larkins 2007; Nykänen et al. 2015; Nykänen et al. 2017). Successful use of the method requires a set of known examples of the deposit type in question. The locations of known deposits and occurrences within the study area were used as true positive sites. Furthermore, the method also requires true negative sites, which are sites that do not include any deposits or mineral

occurrences. For this, a set of random points was used. The surface expression of the known deposits varies considerably between the known deposits and occurrences. The smallest occurrences consist of single drill hole intercepts, whereas the mapped mineralized zone of the Suurikuusikko deposit extends over 4 km and varies from a few meters to tens of meters in thickness. Therefore, instead of using one true positive point for each deposit, up to 14 points were generated for each deposit on the basis of their surface expression in a similar manner to that reported by Niiranen et al. (2019). As a result, a total of 60 true positive sites was generated, and an equal number of random points was generated for true negative sites to avoid bias. This was repeated 10,000 times.

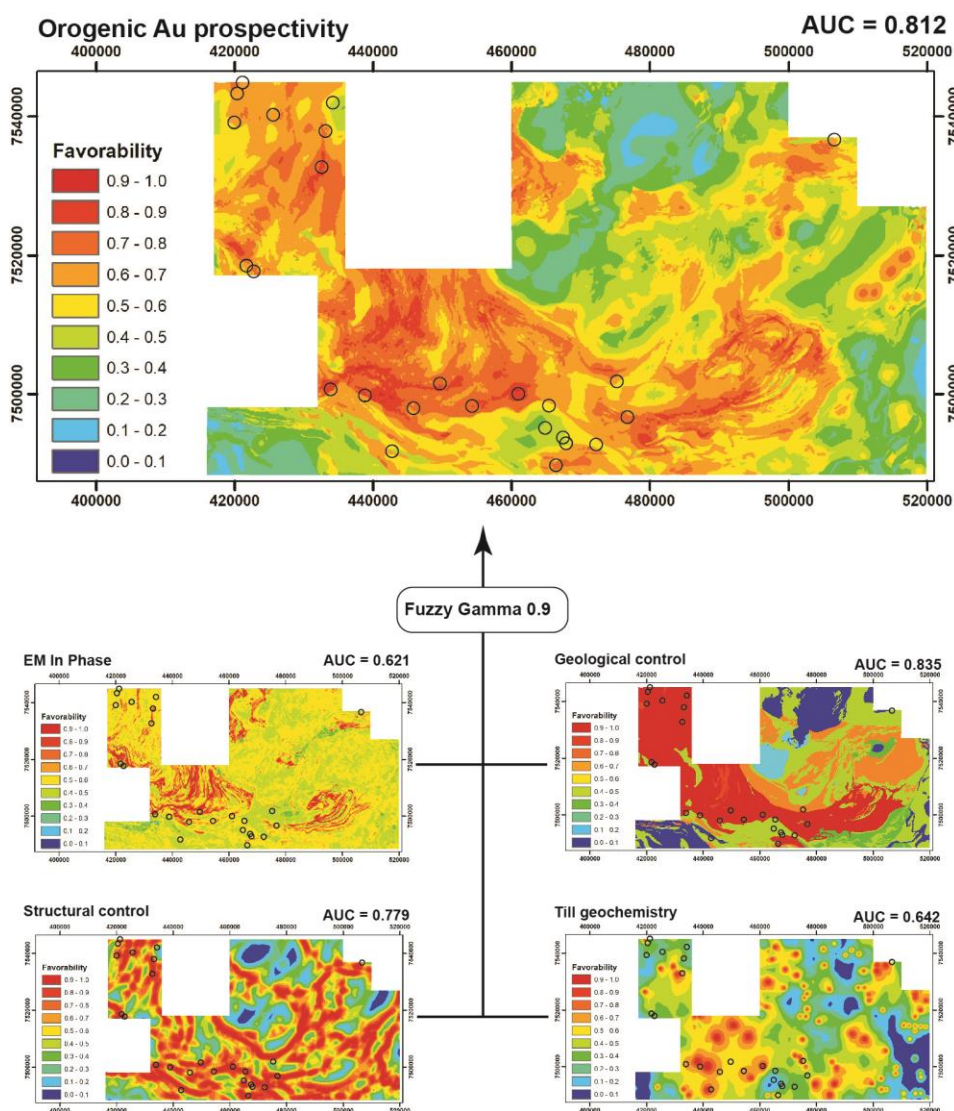


Figure 4.28. Integration of the final orogenic gold prospectivity map. Black circles indicate the location of known gold deposits and prospects. AUC values indicate the calculated AUC value of each layer (see text).

The ROC test was also run for evidential layers and intermediate prospectivity maps, in addition to the final map. This was done to optimize the pre-processing and modeling following the methodology of

Nykänen et al. (2017). The ROC test results in an AUC value, which is a measure of the accuracy of a diagnostic test. The values vary between 1 and 0. A value of 1 indicates a perfectly accurate test, 0.5 indicates that the result is completely random, and a value of 0 indicates that the result is perfectly inverse. The AUC score of 0.812 (Fig. 4.28) indicates that the prospective areas of the orogenic gold map correlate moderately well with the known deposits and occurrences.

4.6.2 Magmatic Ni–Cu prospectivity model

The conceptual mineral system model by Leshner and Keays (2002), Naldrett (2004), Barnes and Lightfoot (2005) and Stephen et al. (2012) was used for magmatic Ni–Cu deposits. There are two known Ni–Cu deposits and two known Ni–Cu occurrences within the study area. Due to this, the fuzzy logic method was used for Ni–Cu prospectivity modeling. Datasets on till geochemistry (Co, Cu, Ni, Pd), bedrock map data (lithology), the XL3D regional 3D geomodel (conduits), low altitude geophysical data (TMI, real EM component, imaginary EM component), ground gravity (Bouguer), and GTK’s mineral indication database comprised the used data sets (Table 4.5).

Table 4.5. Input data and exploration criteria

Exploration criteria	Data set	Derived data set
Till geochemistry	Till geochemistry 1 sample per 4 km ²	Interpolated grids (kriging) Cu, Co, Ni, Pd
Mafic intrusives present	Bedrock map	Proximity to mafic intrusives
Komatiites present	Bedrock map	Proximity to komatiite units
Magmatic conduits	XL3D regional 3D model	Proximity to conduits
Geophysical indications	Low-altitude TMI map	SOM clusters and Q-error
Geophysical indications	Low-altitude real and imaginary EM maps	SOM clusters and Q-error
Geophysical indications	Regional gravity, 1–4 observation points per km ²	SOM clusters and Q-error
Proximity to Ni and Cu indications	GTK’s mineral indications database	Proximity to Ni–Cu indications

The till geochemical data were pre-processed to evidential layers, as was done with the orogenic gold model. A Euclidean proximity raster was calculated for the komatiitic units. Similarly, a proximity raster was calculated for lithological units consisting of 2.44 Ga and 2.05 Ga layered intrusions, 2.2 Ga, 2.10 Ga, and 2.05 Ga mafic and ultramafic sills, dykes, and intrusions. In addition, Euclidean proximity rasters were calculated for conduits and Ni–Cu indications. Geophysical data were processed into ten clusters using the SOM method (chapter 4.2). Moreover, a Q-error SOM map was used as an evidential layer. The Euclidean proximity raster “Ni–Cu indications” was calculated from known Ni–Cu indications. The evidential layers were scaled to a 0–1 scale using equation [1] and the midpoint and spread values listed in Table 4.6. Mean values were used as the midpoint for till geochemical data. A midpoint of 1000 m was used for proximity to komatiites and proximity to mafic intrusion evidential layers, and 3000 m was used for proximity to Ni–Cu indications, while 0.06 was used as a midpoint for the Q-error

map. The SOM cluster map was classified into categorical layers. Values between 0.1 and 0.9 were given to different clusters based on expert estimates of how the SOM clusters correlated with potential host rocks for Ni–Cu deposits, i.e. clusters that showed a correlation with the ultramafic intrusives and komatiites were given high values and clusters correlating with TTG gneisses were given low values (chapter 4.2).

Table 4.6. Midpoint and spread values used in rescaling the evidential datasets

Data layer	Midpoint	Spread
Co in till	20 ppm	4
Cu in till	61 ppm	3
Ni in till	68 ppm	3
Pd in till	1.4 ppb	3
dst Komatiites	1000 m	-3
dst Mafic intrusives	1000 m	-3
dst Conduits	3000 m	-3
SOM Q-error	0.06	2
dst Ni–Cu indications	3000 m	-3

Categorical classification was used for SOM clusters

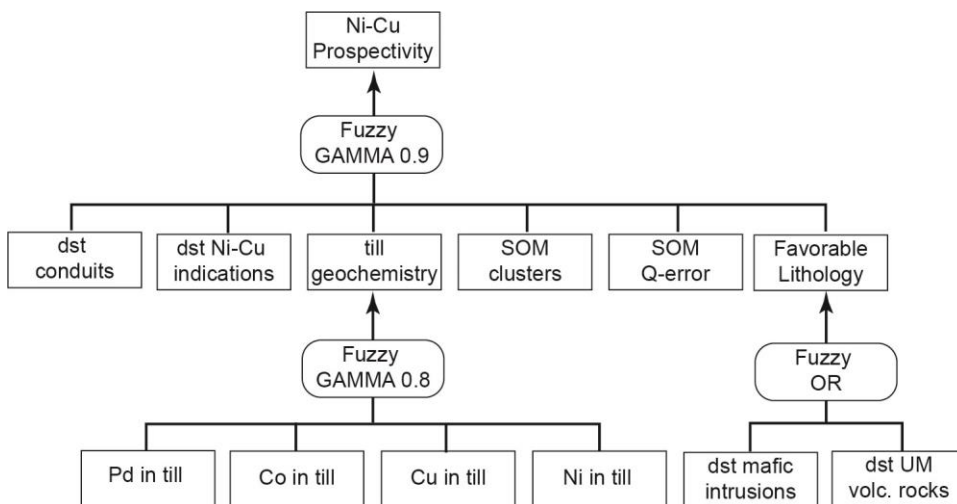


Figure 4.29. Flow chart for the fuzzy logic Ni–Cu model.

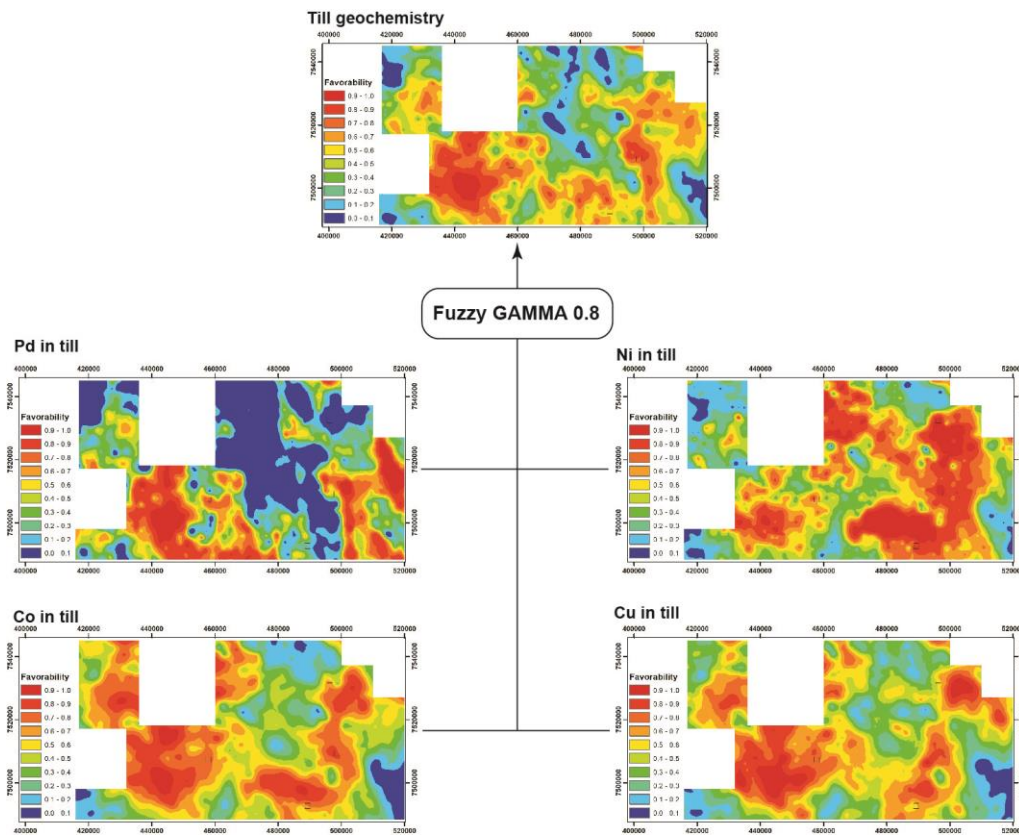


Figure 4.30. Integration of the till geochemistry intermediate prospectivity map

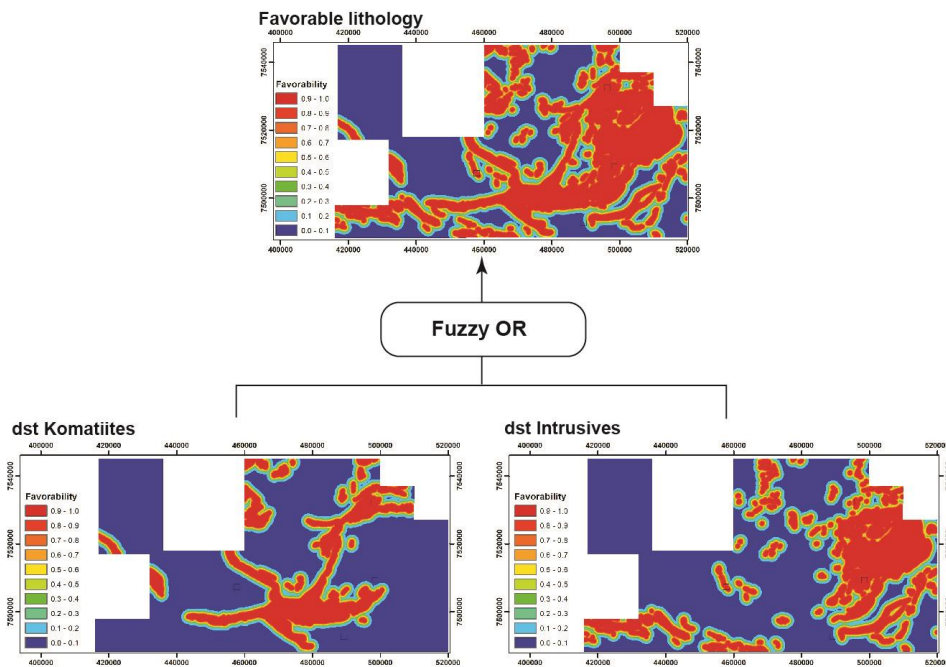


Figure 4.31. Integration of the favorable geology intermediate prospectivity map

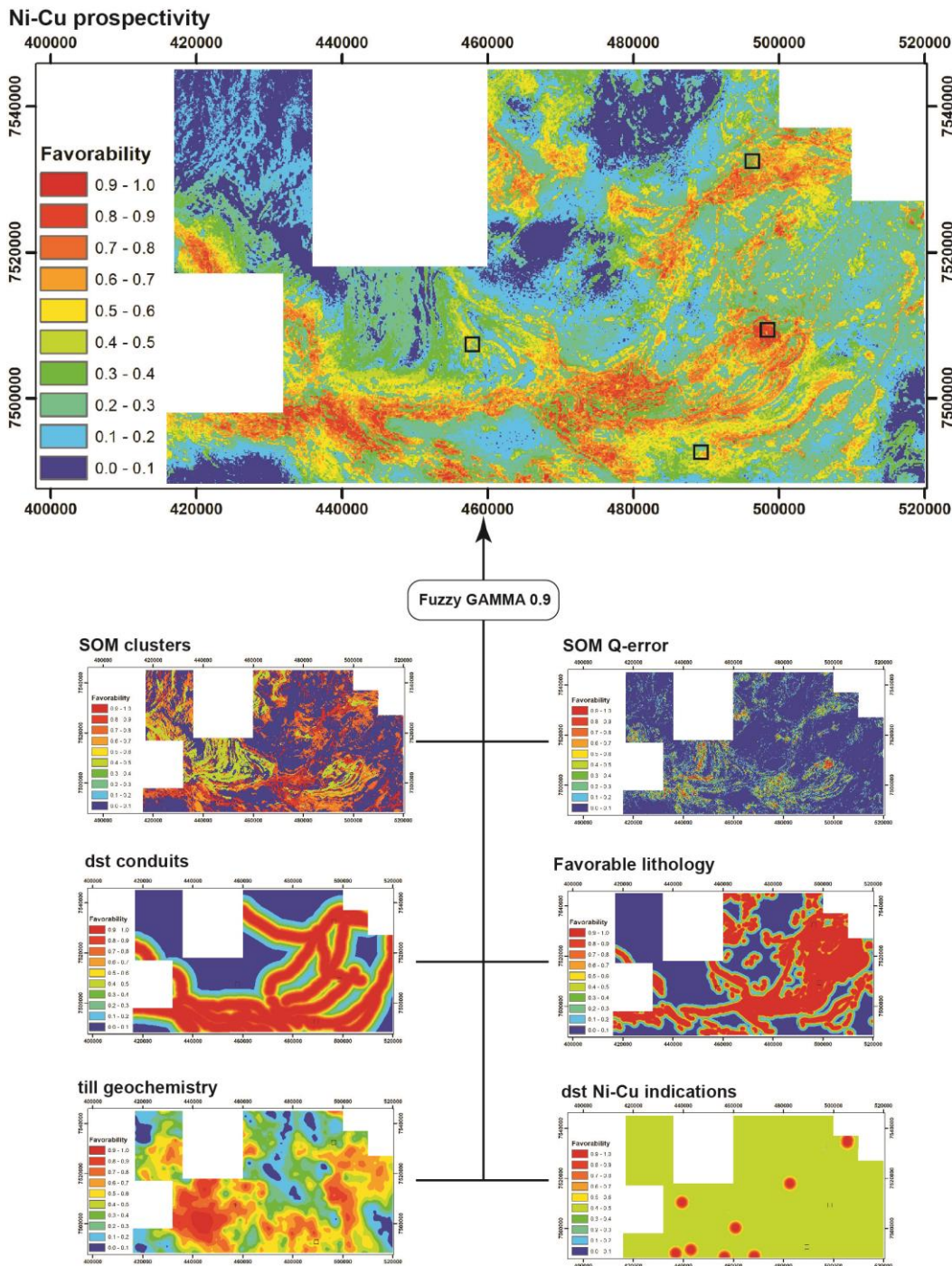


Figure 4.32. Integration of the final Ni–Cu prospectivity map. Black squares mark the locations of known magmatic Ni–Cu deposits and occurrences.

The evidential layers were integrated to intermediate prospectivity maps and final prospectivity maps using fuzzy OR and fuzzy GAMMA operators (Fig. 4.29). Ni, Pd, Cu, and Co in till evidential layers were integrated into an intermediate prospectivity map indicating the till geochemical signature (Fig. 4.30).

The evidential layers proximity to mafic intrusions and proximity to ultramafic volcanic rocks were combined into a “favorable lithology” intermediate prospectivity map using the fuzzy OR operator (Fig. 4.31). The final prospectivity map was integrated from the rest of the evidential layers and these intermediate maps using the fuzzy GAMMA operator (Fig. 4.32). Statistical evaluation of the Ni–Cu model could not be carried out due to the very limited number of known Ni–Cu deposits within the study area. Therefore, the estimation of model quality was limited to visual estimation only.

5 RESULTS

5.1 3D geological models

5.1.1 Modeled elements

Figure 5.1 presents a schematic diagram illustrating the modeled lithostratigraphic units and tectonic zones of the study area. The maximum depth of the CLGB in the area is 6 km, which was estimated using the gravimetric and reflection seismic survey data. The lithostratigraphic units at depth were mostly estimated utilizing a plan view geological map and taking into account the documented dip of the bedding, but in places, AMT and magnetic data were also used. The dip of the tectonic zones shown in Figure 5.2 was in most cases modeled on the basis of reflection seismic survey data. The abbreviations of the tectonic zones shown in the figures are explained in Table 5.1. Furthermore, the tectonic zones are presented in the plan view map in Figure 5.3.

Table 5.1. Modeled tectonic objects and their abbreviations presented in the figures.

Abbreviation	Name	Surfaces
KaSZ	Kaarestunturi shear zone	1
KeTZ	Kelujärvi thrust zone	1
KoTZ	Koitelainen thrust zone	1
LoTZ	Lokka thrust zone (1-2)	2
MoTZ-A	Moskuvaara thrust zone A	5
MoTZ-B	Moskuvaara thrust zone B	2
MoTZ-C	Moskuvaara thrust zone C	1
MöTZ	Möykkelmä thrust zone	1
NuTZ	Nuttio thrust zone*	3
PeTZ	Peurasuvanto thrust zone	1
PorSZ	Porkkaus shear zone	1
PoSZ	Porkkonen shear zone*	2
SeTZ	Seurukarkea thrust zone*	2
SiTZ	Sirkka thrust zone	3
SoTZ	Soasjoki thrust zone	1
VeTZ	Venejoki thrust zone	1

*From the 3D model of Niiranen (2015).

The tectonic zones are classified into four groups on the basis of their strike and dip directions. The groups predominantly represent thrust zones, for which the age relations were estimated on the basis

of the cross-cutting relationship, using plan view geophysical maps and reflection seismic survey data. The earliest faults belong to N–S-trending and eastward-dipping thrust zones (the black surfaces in Fig. 5.2), followed in age by E–W-trending and southward-dipping thrust zones in the southern part of the study area (the blue surfaces in Fig. 5.2). The E–W-trending and north-dipping faults belong to the youngest thrusts zones (red surfaces in Fig. 5.2). They were followed by faulting along NE–SW-trending vertical shear zones (the green surfaces in Fig. 5.2). The Nuttio thrust system is dipping to west and its relation to the presented scenario is discussed below.

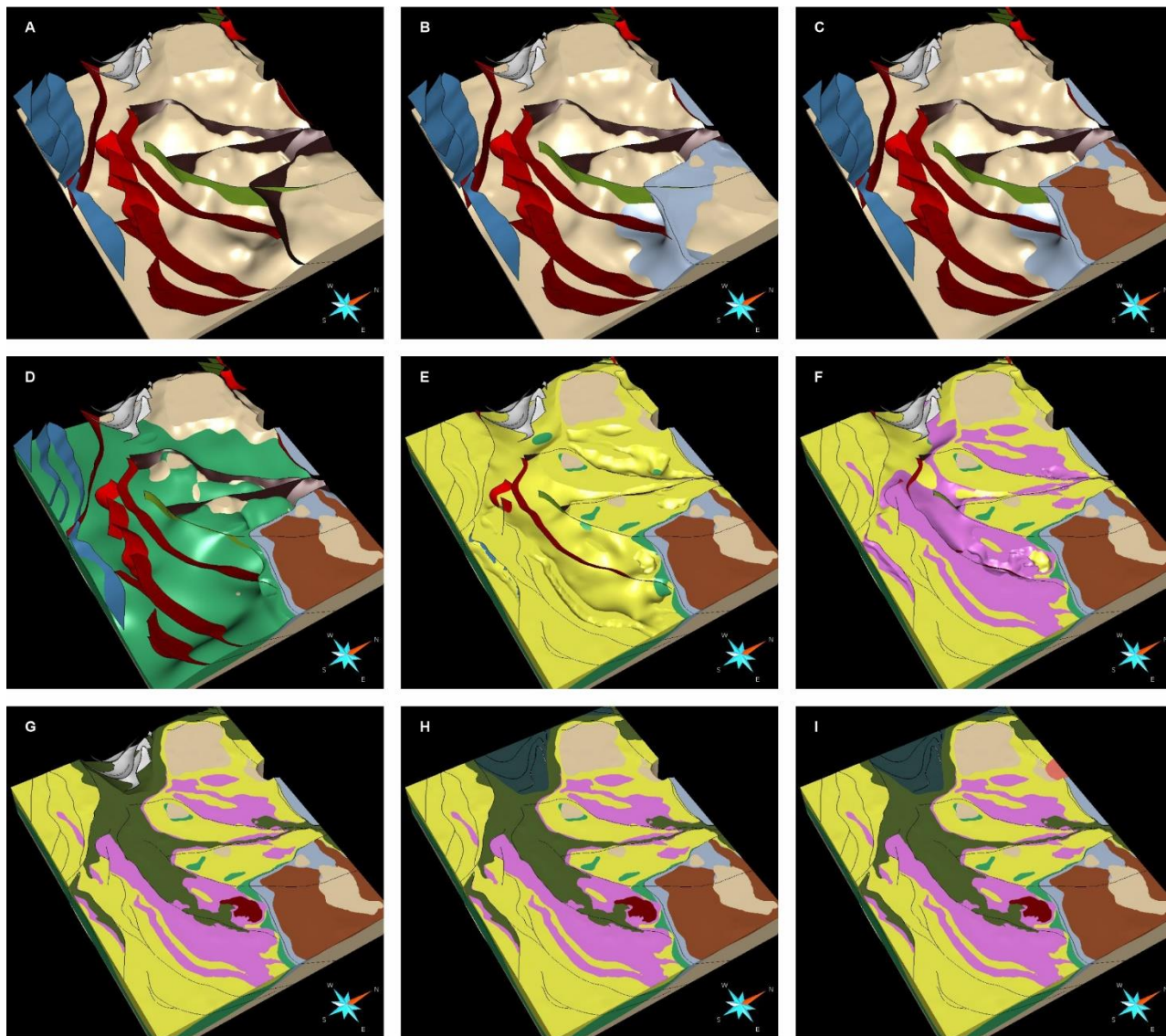


Figure 5.1. A schematic diagram showing oblique views of the modeled lithostratigraphic units and tectonic zones: A) the basement complex, B) the Salla group, C) the Koitelainen intrusion, D) the Kuusamo group, E) the Sodankylä group, F) the Matarakoski formation of the Savukoski group, G) the Sattasvaara formation of the Savukoski group and the Kevitsa intrusion, H) the Kittila suite, and I) the Nattanen suite. The lithostratigraphic units are shown as 3D model objects and tectonic zones as surfaces. The view of is from SSE in all of the figures.

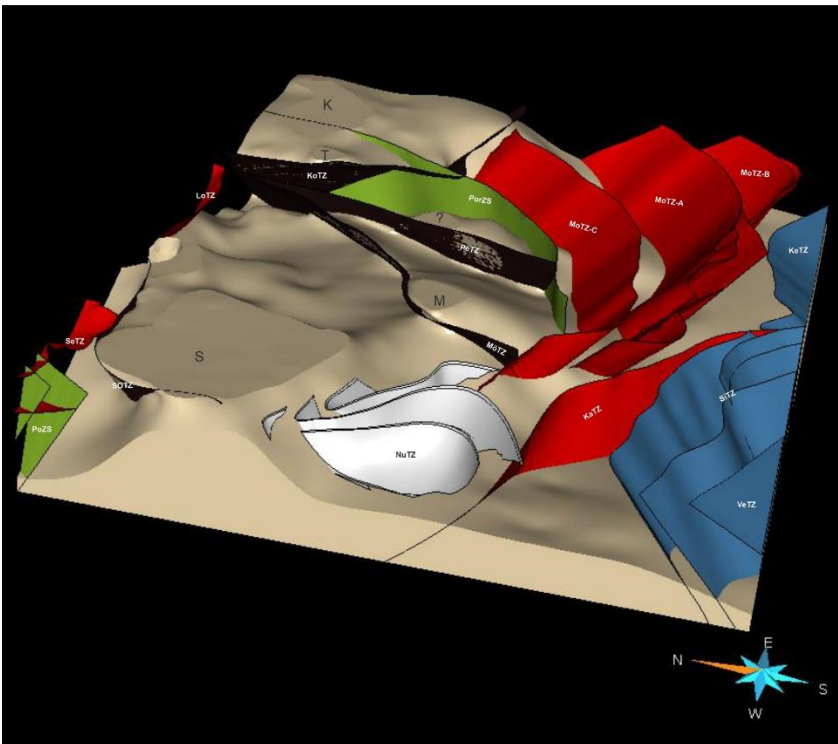
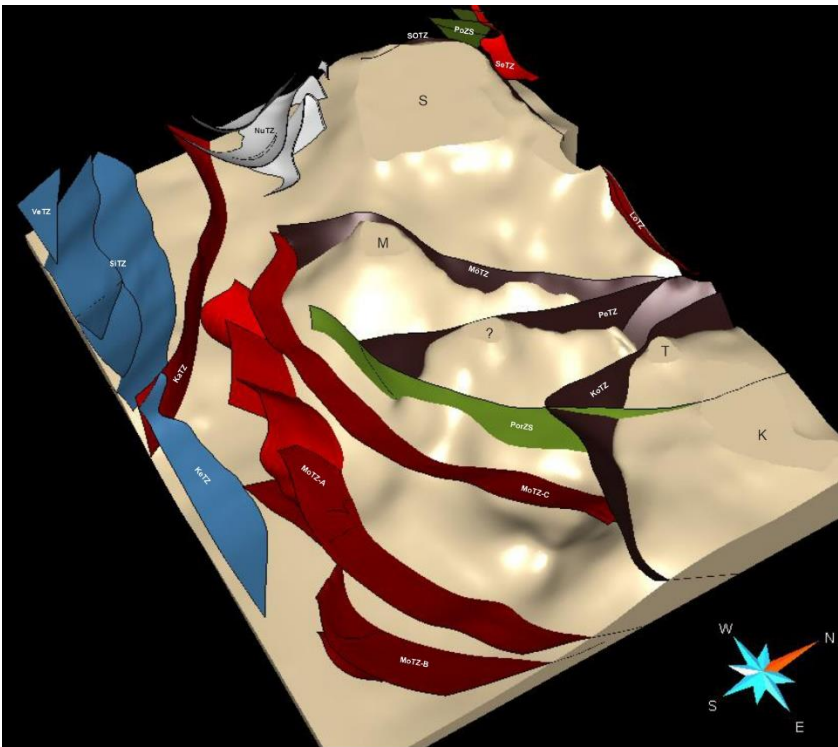


Figure. 5.2. Oblique views of the model from the SE (upper picture) and W (lower picture) showing tectonic zones as surfaces and the Archean basement as a 3D model object. See Table 5.1 for a key to the abbreviations. The abbreviations of the exposed basement domes are: S = Soasjoki, M = Möykkelmä, T = Tojottamanselkä, K = Kiviaapa, ? = Anonymous.

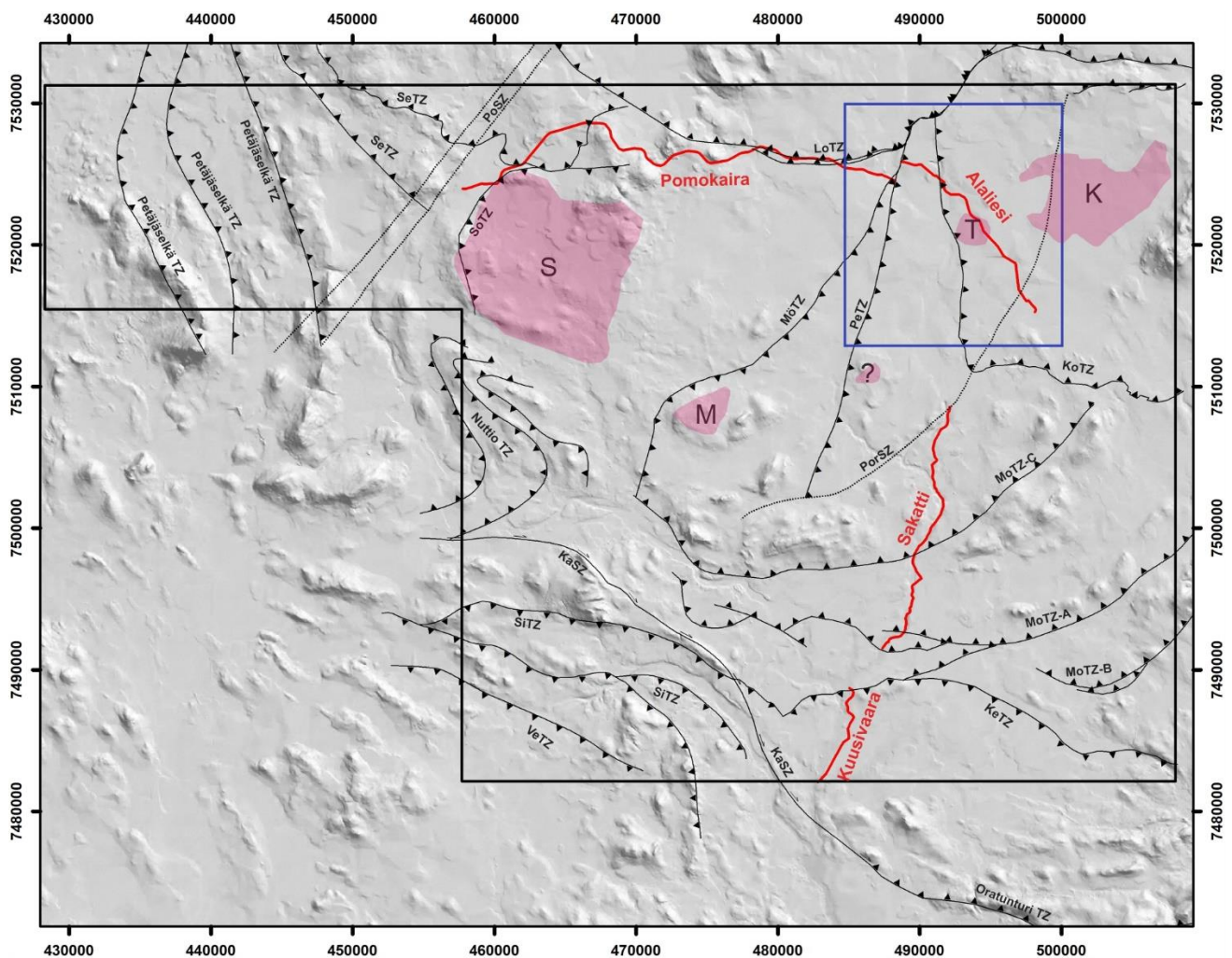


Figure 5.3. Hillside digital elevation model of the study area with the location of the modeled tectonic structures (the Petäjäseltä thrust zone and Nuttio thrust zone are from Niiranen 2015). Seismic survey lines are shown as red lines and the Alaliesi sub-area as a blue square. The exposed basement domes are colored in pink and their abbreviations are: S = Soasjoki, M = Möykkelmä, T = Tojottamanselkä, K = Kiviaapa, ? = Anonymous. Coordinate system ETRS-TM35FIN.

5.1.2 N–S-trending thrust zones

The Alaliesi seismic survey shows reflections located below the exposed basement rocks of the Tojottamanselkä dome (“T” in Fig. 5.3). This feature allows a thrust zone to be considered on the western side of the Koitelainen intrusion, the Koitelainen thrust zone (KoTZ), along which the intrusion and Archean basement was thrust towards the west over the younger supracrustal rocks (Fig. 5.4). This idea is further leveraged with the other basement exposures in the study area, and at least in the Pomokaira seismic survey, the scenario of a westward-thrusting Soasjoki thrust zone (SoTZ) could be used to explain the relatively deep seismic reflections located very near the Soasjoki dome (“S” in Fig. 5.3). The other interpreted thrust zones of this west-vergent thrust system are the Möykkelmä (MötZ) and Peurasuvanto thrust zones (PeTZ).

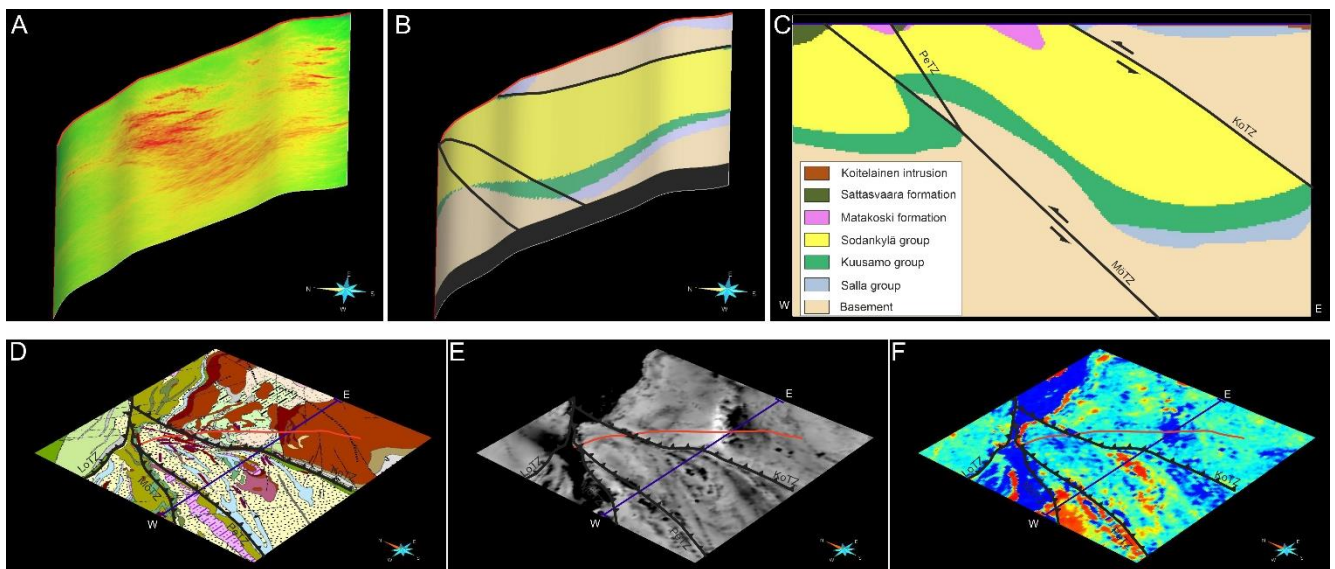


Figure 5.4. Interpreted 3D sections of the Alaliesi area: A) the CBFVM processed seismic reflection survey profile from Alaliesintie, B) geological interpretation of the seismic survey profile, and C) geological interpretation along a W–E-trending cross-section. The locations of the reflection seismic survey profile (red) and W–E-trending cross-section are shown in the geological (D), aeromagnetic (E), and aereoelectromagnetic (F) map. See Table 5.1 for a key to the abbreviations.

5.1.3 E–W-trending thrust zones

The Sakatti and Kuusivaara seismic surveys reveal both south- and north-dipping reflections, which have been interpreted to be due to folding and overthrusting in two oppositely directed thrust systems (Fig. 5.5). It is likely that the southward dipping system is older than the northward dipping one. This age relation has been interpreted on the basis of the Kaarestunturi shear zone (KaSZ), which in the plan view geophysical maps cuts the south-dipping Sirkka, Venejoki, and Kelujärvi thrust zones (SiTZ, VeTZ, and KeTZ), and which is an extension of the north-dipping Oratunturi thrust zone south of the study area (see location of the zone from Fig. 5.3) studied by Evins and Laajoki (2002). The cross-cutting relation of these oppositely directed thrust systems is also interpreted from the reflections of the Sakatti seismic survey profile (Fig. 5.6).

The younger northward-dipping, south-vergent thrust systems include the family of Moskuvaara thrust zones (MoTZ-A, -B, and -C) in the southern part of the study area. The thrusts of this group have not been observed in the central part of the study area, but the system is again visible in the Lokka and Seurujärvi thrust zones (LoTZ and SeTZ) in the northern part of the study area. There, the Salla group volcanites have been thrust over younger units of the CLGB. This is most markedly visible in the aerogeophysical data and is illustrated in Figure 5.7, which is a view of the 3D model of the Alaliesi sub-area.

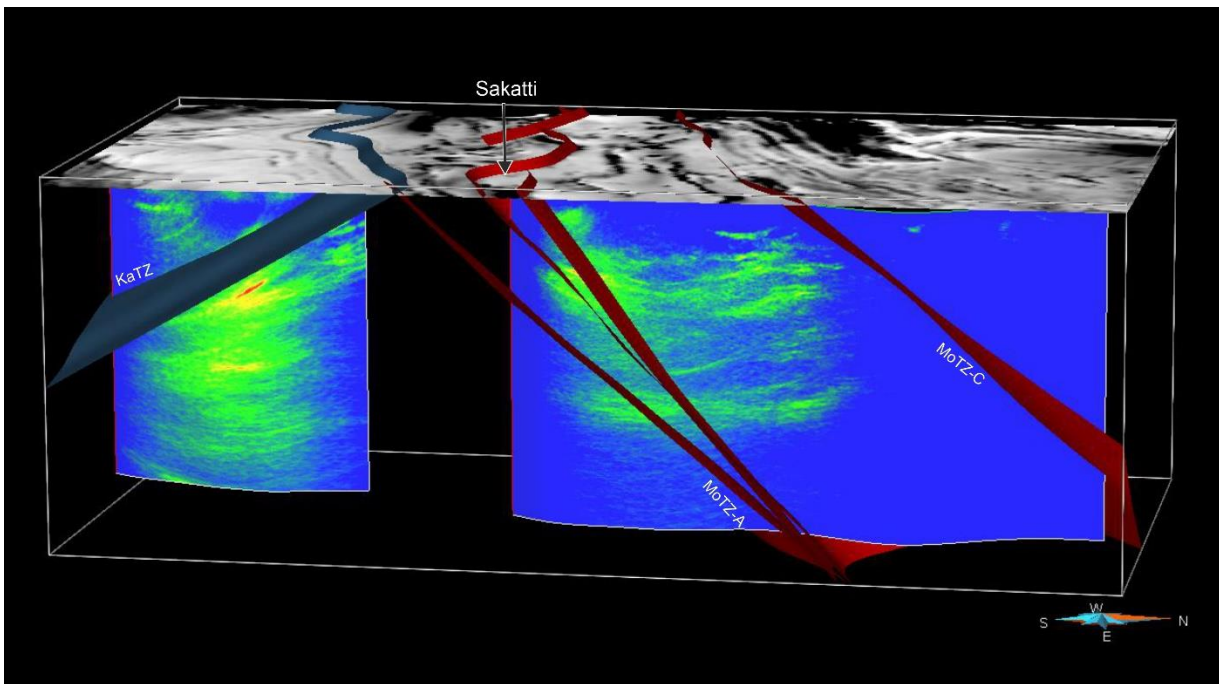


Figure 5.5. CBFVM processed seismic reflection data on the survey profiles of the Kuusivaara (left) and Sakatti (right) showing south- and north-dipping reflections, which have been interpreted to be due to folding and overthrusting in two oppositely directed thrust systems (thrust planes shown as surfaces). The plan view image is a low-altitude aeromagnetic map.

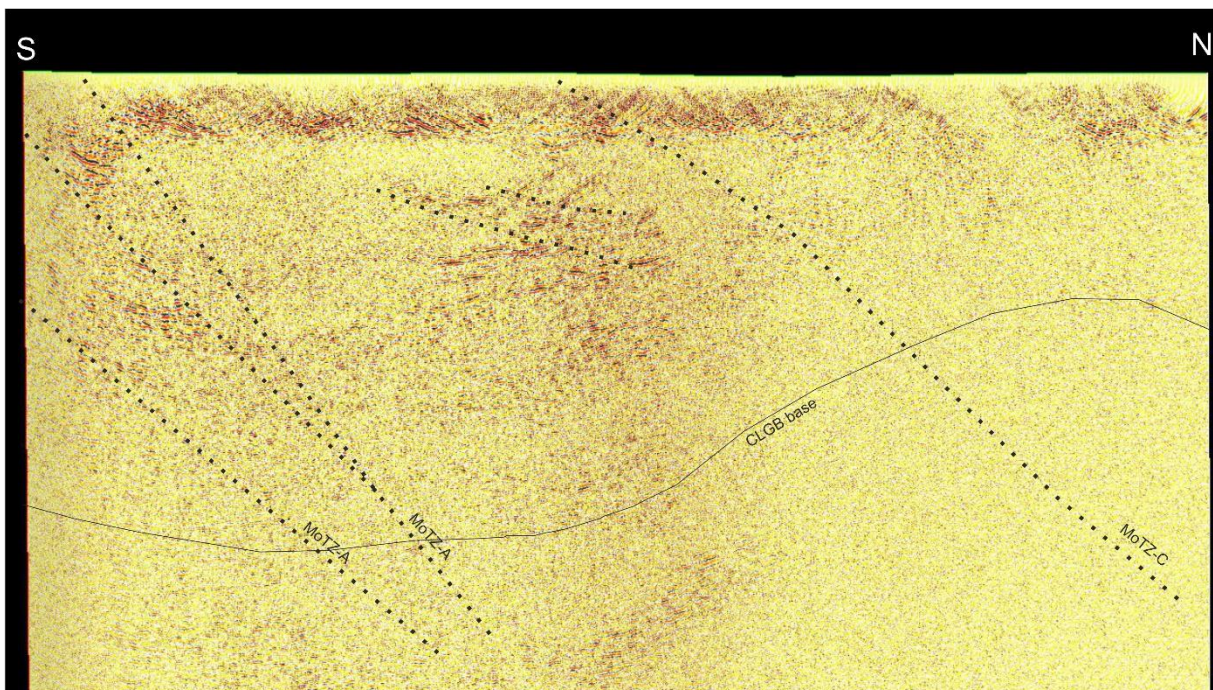


Figure 5.6. Sakatti seismic profile (looking west) with the interpreted structures and base of the CLGB (the seismic data were processed following hardrock seismic data processing at GTK). The location of the seismic profile is shown in Figure 5.3.

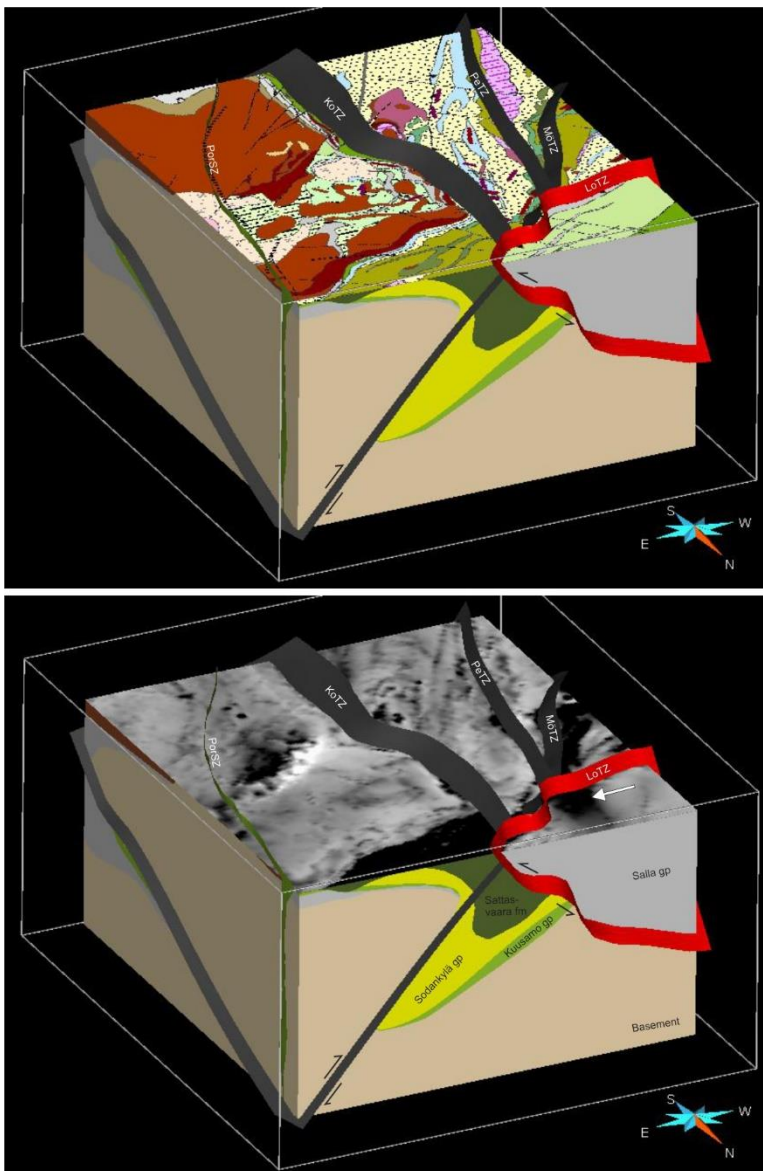


Figure 5.7. 3D model of the Alaliesi sub-area viewed from the NE, and showing fault surfaces and a geological map (A) and aeromagnetic map (B). The arrow shows an area in the aeromagnetic data indicating that the Salla group volcanites have been thrust over the rocks of the Sattasvaara formation.

5.1.4 NE–SW-trending shear zones

These tectonic zones (PorSZ, PeSZ) were interpreted on the basis of plan view maps and are assumed to be the latest tectonic structures in the area.

5.1.5 The Nuttio thrust system

The east-vergent Nuttio thrust zone (NuTZ) is illustrated by white surfaces in Figures 5.2 and 5.3. The surfaces of this thrust zone are from the 3D model presented in Niiranen (2015).

5.1.6 Discussion

The structural interpretation presented here suggests that the deformation history in the study area was predominantly controlled by thrust tectonics in at least three deformation phases. The conclusion of deformation stages in the study area is in line with the studies by Niiranen (2015) and Sayab et al. (2019) on the deformation history of the Kittilä suite, located west of the study area.

The earliest deformation stage in the study area was characterized by thrusting in deep-extending west-vergent reverse faults, which resulted in a N–S-trending inclined fold pattern and the exposures of the basement complex in the central part of the study area. This stage can be linked to the E–W-directed bulk shortening of the D₁ stage of thrusting and stacking at ca. 1.92 Ga in the scheme of the Kittilä suite presented by Sayab et al. (2019). In the Kittilä suite, the D₁ stage has been associated with the family of west-vergent thrust splays that coincide in the detachment zone at the base of the suite, interpreted on the basis of the seismic reflection surveys conducted in 2001–2005 and 2008–2009 (Niiranen 2015). For example, the Petäjäseltä thrust zone presented in Figure 5.3 belongs to these thrusts, and it is likely that the NuTZ was also initiated during the D₁ stage. This is because the NuTZ is N–S directed and, according to Niiranen (2015), the Kittilä suite in the area of this thrust zone is a very thin, tongue-shaped block, which means that the structures in this area could well have been rotated during later deformation events.

The following thrusting event in the study area could have been one such stage, as it dominates the southern part of the study area, where the thrusting caused the E–W-trending fold pattern visible in the aerogeophysical maps. In the study area, the SiTZ, VeTZ, and KeTZ represent the thrust zones of this stage, and they can be linked with the N–S-trending shortening of the D₂ stage (1.90–1.89 Ga) in the scheme of Sayab et al. (2019), who interpreted that during this stage, the regional strain was released in north-vergent thrust zones along the southern and northern margins of the CLGB.

The latest thrusting was south vergent and took place in the northern and southern parts of the study area. The reason why this phase is not visible in the central part of the study area may be due to the rigid basement domes and the faults of the earliest stage, which could have reactivated as transverse faults and therefore served as boundaries for the released strain during this N–S-trending shortening stage. This last thrusting stage in the study area can be linked to the D₃ stage in the scheme of Sayab et al. (2019), who attributed the deformation of this stage to the NW-vergent thrusting of the Lapland Granulite belt from 1.88–1.87 Ga.

The strike-slip faults, which have been interpreted to represent the youngest deformation stage in the study area, may actually be related to the thrust faults of the first stage, which were reactivated as transverse faults during later deformation stages.

5.2 Prospectivity models

Two prospectivity models were generated in the XL3D project, one for orogenic gold deposits and the other for magmatic Ni–Cu deposits. Visual comparison suggests a relatively good fit between the known orogenic gold deposits and occurrences and high prospectivity areas in the final prospectivity map (Fig. 5.8). Most of the known deposits and occurrences overlie high prospectivity (favorability 0.8–1.0) or moderate prospectivity (favorability 0.6–0.8) locations. However, the ROC test using the known deposits as true positive sites and a random point set as true negative sites yielded an AUC score of 0.812, which indicates only a moderate result. A cluster of known occurrences just north of the Kaarreselkä deposit falls outside the high or moderate prospectivity areas. However, this alone does not explain the moderate AUC result. The final orogenic gold prospectivity map indicates that a considerable percentage of the study area is moderately to highly prospective. This is in line with previous prospectivity modeling studies in the CLGB area (e.g. Nykänen & Salmirinne 2007; Niiranen et al. 2019), and the results of this project thus confirm that the study area is among the most prospective areas for orogenic gold in the CLGB. The large percentage of high prospectivity areas results in a high percentage of randomly generated true negative sites for the ROC test falling in these areas, and as such, the AUC values will be lower even if the true positive sites were all in high prospectivity areas.

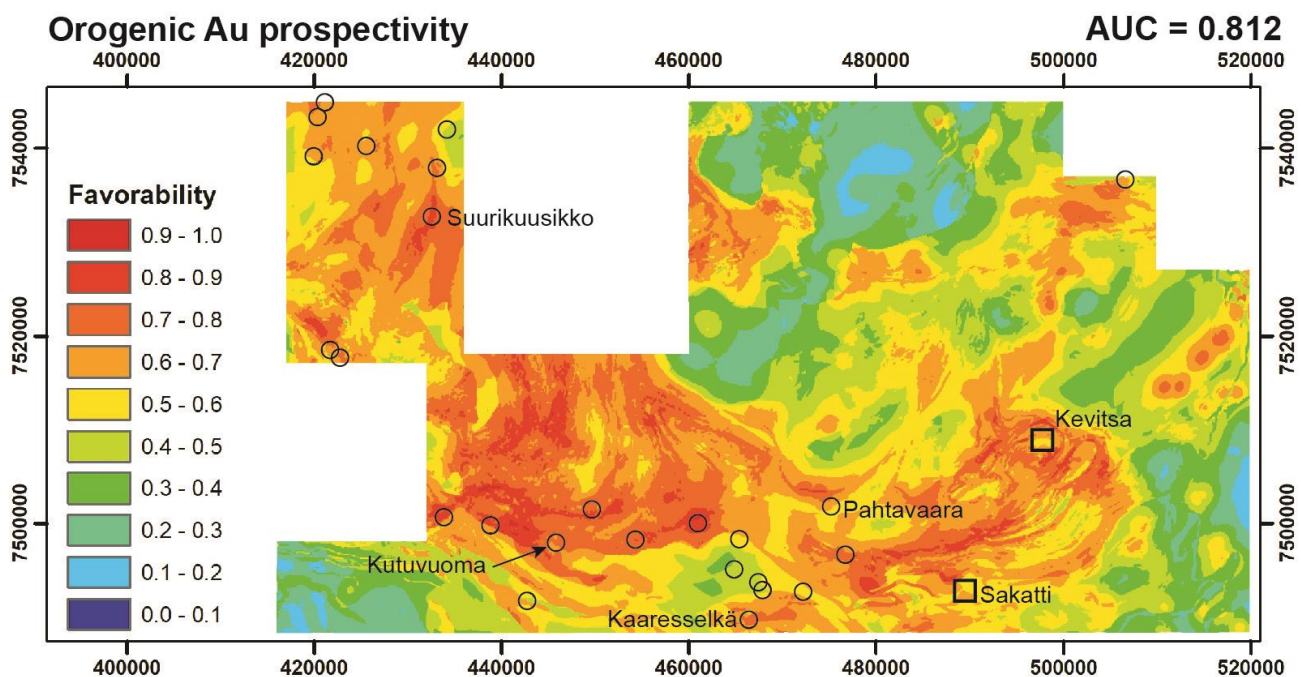


Figure 5.8. The final orogenic gold prospectivity map. Circles denote the location of known gold deposits and prospects, and squares known significant magmatic Ni–Cu deposits.

A comparison of the results with the belt-scale prospectivity map of Niiranen et al. (2019) indicates that the general pattern of the maps is fairly similar. The prospectivity map presented in this work

narrows down the high prospectivity areas (favorability 0.8–1.0), and the changes in their location are relatively small. The main differences between the evidential data are in the structural dataset, which was modified in this work based on the 3D modeling results. The data on gold in till were processed into an evidential layer, which was not carried out in the work by Niiranen et al. (2019).

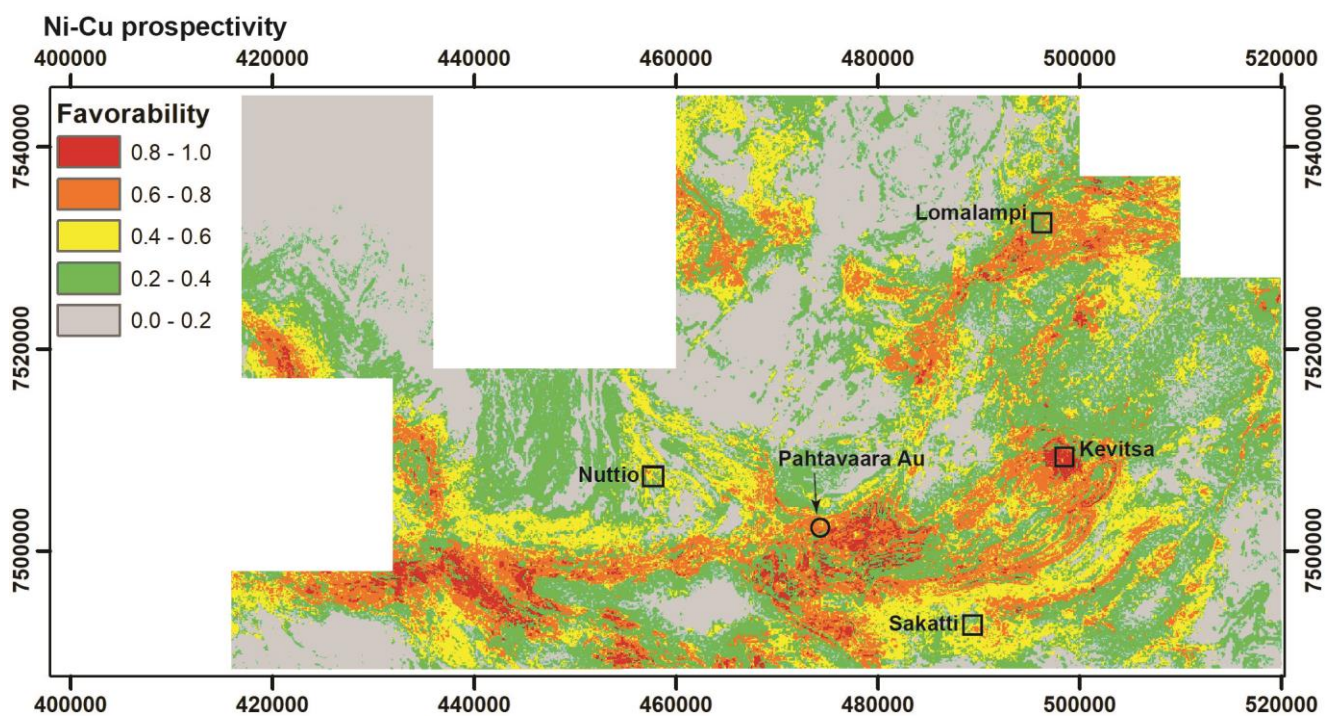


Figure 5.9. Magmatic Ni–Cu prospectivity map generated in the project. Squares mark the location of the known Ni–Cu deposits and prospects. The location of the Pahtavaara gold deposit is marked with a circle.

The magmatic Ni–Cu prospectivity model utilized geophysical SOM clusters, SOM Q-error and 3D geomodeling data generated in the previous stages of the XL3D project. The final Ni–Cu prospectivity map outlines several high prospectivity targets (favorability 0.8–1.0) within the study area (Fig. 5.9). Due to the limited number of known deposits and occurrences, no statistical evaluation similar to the orogenic gold case could be carried out. The Kevitsa deposit is indicated with a broad high prospectivity area. Small moderate prospectivity areas correspond to the Lomalampi komatiite-hosted prospect, as well as the ophiolite-related Nuttio prospect. Only a small area of moderate prospectivity occurs in the location of the Sakatti deposit. This is probably partly due to the fact that the current version of the bedrock map does not show any ultramafic rocks in Sakatti, resulting in the location falling into low prospectivity areas in the “favorable lithology” evidential layer. This illustrates the potential pitfalls of using interpreted data such as bedrock maps in prospectivity modeling. However, we feel that the benefits of using interpreted evidential data such as geological maps and 3D models outweigh these problems, which should, however, be kept in mind when using prospectivity maps generated using

such data. One of the high prospectivity clusters in the prospectivity maps occurs next to the Pahtavaara gold deposit. The deposit is hosted by altered komatiites within a broader Sattasvaara komatiite sequence. Interestingly, massive sulfide lenses with elevated Ni–Cu–Co grades have been reported by the previous owner of the deposit (Lapland Gold Miners).

6 DISCUSSION AND CONCLUSIONS

The XL3D workflow presented in this report can be used with targets varying in data density, from a regional scale to a deposit scale. One of the main aims with the workflow is that all the available datasets are used efficiently and that the final model provides a holistic representation of the available datasets. 3D geomodeling using multiple datasets, ranging from different fields of geophysics to geological field observations, is an iterative process and requires input from a number of experts from different fields of geoscience. As such, for a successful result, teamwork with active discussions between the experts throughout the process is imperative.

Seismic reflection data acquired within the XSoDEx project were originally processed using the Fresnel Volume Migration algorithm developed at TU Bergakademie Freiberg, Germany. These results were utilized in the first versions of the 3D geomodel. However, it was noted that seismic images are not optimal, especially from the shallower (<1500 m) part of the seismic section. Thus, it was decided to return to the workflow question “Are the data valid?” and we realized that the data need to be reprocessed in order to achieve a better image of the shallow subsurface. The seismic image was improved by using a standard hardrock seismic processing flow employing static corrections that had not been previously made. This example emphasized the importance of flexible thinking during the process that enables critical inspection of possible improvements needed within any stage of the workflow.

Potential field inversions are inherently ambiguous; however, the inversion algorithms optimize the results towards a physically realistic solution. By adding geological information into the process as inversion constraints, the results conform with the known geology and can better ‘fill the gaps’ in areas with little or no geological information. As geological constraints must be expressed in terms of petrophysical data values or value ranges, the geological units used in defining the constraints should have petrophysical signatures that are as distinct and homogeneous as possible. Thus, transforming geological models or data into inversion constraints should be a joint effort between geologists and geophysicists. In regional 3D inversion modeling, petrophysical sample data are often only available at shallow depths (from outcrop sampling or shallow drilling in relation to the inversion depth). However, even shallow data help constrain the inversions and should be applied if available.

There are numerous clustering algorithms, and a SOM was chosen for data integration in the XL3D project because it offers good visualization to describe the clusters. In addition, SOMs have been used

in a similar manner before (Carneiro et al. 2012; Cracknell et al. 2014; Bierlein et al. 2008). The SOM process should be applied in an iterative manner. Often, it takes multiple attempts to find suitable datasets or SOM and k-means parameters. Correlation and principal component analysis provide useful insights into the data. In this project, approximately 30 SOM analyses were studied. It is important to combine knowledge of data mining with geological knowledge to understand what the results mean in a geological context and how the SOM process needs to be modified to reveal something else. Running the process multiple times also shows whether the clustering results are robust.

A SOM can also be used and performs well with data that include missing values (Cottrell & Letrémy 2005). When calculating the BMU, the missing attribute is ignored, and the closest SOM cell is found using the remaining attributes. The same approach is used when the weights are updated. After the training has been completed, the missing values can be estimated using the attribute values of the BMUs. This is very useful when single pixels are missing in a datasets, areas have been masked out, or when rasters do not cover the same area. For many other methods, these data points would simply be left out of the analysis, but a SOM can utilize the remaining data in the algorithm. A SOM is a non-spatial model, meaning that the algorithm ignores the spatial location of points. It simply considers all input data as independent values with no relation to the neighboring locations. There are no spatial clustering models that could account for heterogeneity, which means that in different locations, different processes yield the data, and the analysis aims to reveal this variation. Splitting the study area into smaller areas is one simple solution that was tested during the project. On the other hand, due to the nature of SOMs, using the process requires very little modification when applied to 3-dimensional data. The SOM algorithm remains the same; only the visualization of the results is different. The XL3D project initially planned to test the SOM approach for 3D data, but the study area lacked suitable datasets and this work had to be dropped. However, in brownfield areas such as mine sites with abundant drilling data and multiple different deep-penetrating geophysical datasets, data mining and data integration with the SOM approach would be beneficial and thus these steps are included in the workflow (Fig. 4.1).

3D models recovered from geophysical inversions describe the physical properties of the rocks. The properties from all inversion models (physical properties) may not be directly relevant to all geological modeling units (for example, not all units are magnetic or have a density contrast with each other). For this reason, different models should be used concurrently and together with reflection seismic data. Model comparison can be time-consuming; however, geophysical inversions are one of the few ways of acquiring numerical information from deep depths and, as such, the models should be carefully analyzed in geological modeling. Petrophysical sampling or the study of existing petrophysical data helps in linking the models with geological units.

Evaluation of the ore potential of the study area focused on two deposit types, orogenic gold and magmatic Ni–Cu deposits, and it was carried out through mineral prospectivity modeling. The mineral system models related to these deposit types differ considerably with respect to the geological elements that are critical in the formation of the two deposit types. However, understanding the local geological evolution and framework is essential for the exploration of all deposit types. Geological 3D modeling is a very good method for improving this understanding, as it does force considerably more rigorous testing of different hypotheses than more traditional 2D interpretations (i.e. 2D maps and sections). However, 3D modeling is labor-intensive and time-consuming, and thus it is most cost-effective when focused on modeling elements that are essential for the ultimate problem aimed to be solved.

The significance of the generated 3D geomodel in prospectivity modeling can be illustrated via the structural data. For orogenic gold, the most important aspect on the scale at which this work was conducted is understanding the structural framework, as the deposits are always structurally controlled. Deep, crustal-scale structures act as the main pathways for mineralizing fluids and second or lower-order splays related to them commonly act as structural traps for mineral deposition (e.g. Groves et al. 1998; McCuaig & Kerrich 1998; Goldfarb et al. 2001). Crustal-scale deep structures also act as conduits in magmatic systems. Although it is somewhat difficult to decipher which of the crustal-scale structures in the study area were already active during the extensional phases between 2.44 Ga and 2.05 Ga, the spatial association with contemporary komatiites and layered intrusions enabled an estimate, which was used as a proxy in the magmatic Ni–Cu prospectivity model.

The geophysical SOM clusters were utilized in prospectivity modeling of magmatic Ni–Cu deposits, but were not found useful in the case of orogenic gold deposits. Magmatic Ni–Cu deposits in general have a good response to geophysical methods, as the mineralization and host rocks are typically always denser than the surrounding rocks, have elevated magnetic susceptibilities through their magnetite (host rocks) or pyrrhotite (mineralization) content, and are conductive (mineralization). The geophysical response of orogenic gold deposits is highly variable. The mineralization itself rarely gives any direct geophysical response, and they occur in highly variably host rock sequences in which mineralization-related alteration patterns vary within and between the deposits. Considering this, it is unsurprising that no correlation was found between the geophysical SOM clusters and known orogenic gold deposits.

6.1 Implications for regional geology and ore potential

The 3D model and related structural interpretation of this project indicates that the deformation history in the study area was predominantly controlled by thrust tectonics. The tectonic zones are Au potential, as they could have been pathways for Au-bearing fluids. In addition, the origin of some of the thrust zones is very likely related to earlier rift-related normal faults that were originally pathways of the primitive magmas, but were later, during a compressional phase, reactivated as thrust

zones. Therefore, the faults and gravimetric anomalies could be used in locating significant igneous bodies at depth.

The orogenic gold potential of the CLGB, including the study area, has been well demonstrated, with numerous known deposits and occurrences, including Europe's largest gold deposit, the Suurikuusikko deposit, being located in the area. The prospectivity map for orogenic gold deposits (Fig. 5.8.) indicates that the highest potential areas are within the Kittilä suite and its southern contact, along the trend from Kaarreselkä to Kevitsa, and in the Peurasuvanto area in the NE corner of the study area. The magmatic Ni–Cu prospectivity map highlights a number of highly prospective areas within the study area, in addition to the one at the Kevitsa deposit (Fig 5.9). In the western part, the most prospective areas fall along the Venejoki thrust zone and to a lesser degree along the Sirkka thrust zone (cf. Fig 5.3). Both structures are crustal-scale features and there are abundant 2.2 Ga mafic sills and dykes, and komatiites, along the VeTZ and SiTZ, respectively. The broad Sattasvaara komatiite area in the proximity of the Pahtavaara Au deposit shows up as highly prospective, and a number of small highly prospective targets exist around the Lomalampi Ni–Cu prospect.

The exploration history in the CLGB is relatively short compared to some of the most renowned gold and nickel districts, and much of the belt can still be considered underexplored. Based on exploration and relinquish reporting, gold exploration in the study area has mainly focused on the Kittilä Suite area and along the SiTZ, and has been less intensive in the eastern parts. Up until the past 15 years, Ni–Cu exploration has chiefly focused on the Kevitsa and Koitelainen intrusions. However, the discovery of the Sakatti deposit resulted a considerable increase in interest in Ni–Cu exploration elsewhere. The prospectivity maps presented in this report suggest that the mineral potential for both Au and Ni–Cu extends beyond the areas where the exploration of these commodities has been most active.

7 ACKNOWLEDGEMENTS

This project was funded by the Business Finland European Union Regional Development Fund Programme for Sustainable Growth and Jobs 2014–2020 (EURA2014 Project code A73339) and private industry. The contributions of Agnico-Eagle Finland Oy, Anglo American Sakatti Mining Oy, Astrock Oy, Aurion Resources Oy, Boliden FinnEx Oy, Geovisor Oy, Magnus Minerals Oy, Palsatech Oy, and Rupert Finland Oy are highly appreciated.

8 REFERENCES

- Airo, M.-L. & Säävuori, H. 2013.** Petrophysical characteristics of Finnish bedrock – Concise handbook on the physical parameters of bedrock. Geological Survey of Finland, Report of Investigation 205. 33 p.
- Anglo American 2019.** Ore reserves and mineral resources report 2019. 54 p. <https://www.angloamerican.com/~media/Files/A/Anglo-American-Group/PLC/investors/annual-reporting/2020/aa-ore-reserves-and-mineral-resources-2019.pdf>.
- Barnes, S.J., Lightfoot, P. 2005.** Formation of Magmatic Nickel Sulfide Ore Deposits and Processes Affecting Their Copper and Platinum Group Element Contents. *Economic Geology* 100, 179-213
- Bedrock of Finland - DigiKP.** Digital map database [Electronic resource]. Espoo: Geological Survey of Finland [referred 25.02.2020]. Version 2.1.
- Bierlein, F. P., Fraser, S. J., Brown, W. M., and Lees, T. 2008.** Advanced methodologies for the analysis of databases of mineral deposits and major faults. *Australian Journal of Earth Sciences*, 55, 79-99.
- Boliden AB 2020.** Mineral Resources and Mineral Reserves 2019. Press release, 13 February 2020 <https://vp249.alertir.com/afw/files/press/boliden/202002124453-1.pdf>.
- Bonham-Carter, G.F. 1994.** Geographic Information Systems for Geoscientists—modelling with GIS: Computer Methods in the Geosciences 13. Pergamon, Oxford, pp. 398.
- Brownscombe, W., Ihlenfeld, C., Coppard, J., Hartshorne, C., Klatt, S., Siikaluoma, J. K., Herrington, R. J. 2015.** The Sakatti Cu-Ni-PGE sulfide deposit in northern Finland. In: Maier, W., O'Brien, H., Lahtinen, R. (eds.), *Mineral Deposits of Finland*. Elsevier, Amsterdam, 211–252.
- Buske, S., Gutjahr, S. and Sick, S. 2009.** Fresnel volume migration of single-component seismic data. *Geophysics* 74(6), WCA47-WCA55.
- Coppard, J., Klatt, S., Ihlenfeld, C. 2013.** The Sakatti Ni-Cu-PGE deposit in northern Finland. In: Hanski, E., Maier, W. (eds.), *Excursion Guidebook FINRUS, Ni-Cr-PGE Deposits of Finland and the Kola Peninsula, 12th SGA Biennial Meeting, Mineral Deposit Research for a High-Tech World*. Geological Survey of Sweden, Uppsala, 10–13.
- Carneiro, C. D. C., Fraser, S. J., Crósta, A. P., Silva, A. M., and Barros, C. E. D. M. 2012.** Semiautomated geologic mapping using self-organizing maps and airborne geophysics in the Brazilian Amazon. *Geophysics*, 77, K17-K24.
- Cracknell, M. J., Reading, A. M., and McNeill, A. W. 2014.** Mapping geology and volcanic-hosted massive sulfide alteration in the Hellyer–Mt Charter region, Tasmania, using Random Forests™ and Self-Organising Maps. *Australian Journal of Earth Sciences*, 61, 287-304.
- Carranza, E. J. M. 2008.** Geochemical anomaly and mineral prospectivity mapping in GIS. *Handbook of Exploration and Environmental Geochemistry* 11, 351.
- Cottrell, M., Letrémy, P. 2005.** Missing values: processing with the Kohonen algorithm, in: *Applied Stochastic Models and Data Analysis*, 489–496.
- Davies, D. L., & Bouldin, D. W. 1979.** A cluster separation measure. *IEEE transactions on pattern analysis and machine intelligence* 2, 224-227.
- Dentith, M., Enkin, R. J., Morriw, W., Adams, C. & Bourne, B. 2019.** Petrophysics and mineral exploration: a workflow for data analysis and a new interpretation framework. *Geophysical Prospecting* 68, 178-199.

- Eilu, P. 2015. Mining history – Finland** In: **Boyd, R., Bjerkgård, T., Nordahl, B. & Schiellerup, H. (editors).** Mineral Resources in the Arctic, 320-321. Geological Survey of Norway.
- Eilu, P., Pankka, H., Keinänen, V.J., Kortelainen, V., Niiranen, T., Pulkkinen, E. 2007.** Characteristics of gold mineralisation in the greenstone belts of northern Finland. In: Ojala, J. (Ed.), Gold in the Central Lapland Greenstone Belt. Geological Survey of Finland, Special Paper 44, 57–106.
- Evins, P. M. & Laajoki, K. 2002.** Early Proterozoic nappe formation: an example from Sodankylä, Finland, Northern Baltic Shield. Geological Magazine 139, 73–87.
- Fawcett, T. 2006.** An introduction to ROC analysis. Pattern Recognition Letters 27, 861–874.
- Fournier, D., Heagy, L. J. & Oldenburg, D. W. 2020.** Sparse magnetic vector inversion in spherical coordinates. Geophysics, 85, J33-J49.
- Groves, D. I., Goldfarb, R. J., Gebre-Mariam, M., Hagemann, S.G., Robert, F. 1998.** Orogenic gold deposits: a proposed classification in the context of their crustal distribution and relationship to other gold deposits. Ore Geology Reviews 13, 7–27.
- Groves, D. I., Goldfarb, R. J., Robert, F., Hart, G.J.R. 2003.** Gold deposits in metamorphic belts: overview of current understanding, outstanding problems, future research, and exploration significance. Economic Geology 98, 1–30.
- Groves, D.I., Santosh, M., Deng, J., Wang, Q., Yang, J. 2020.** A holistic model for the origin of orogenic gold deposits and its implications for exploration. Mineralium Deposita 55, 275-292.
- Hanski, E. S. 1997.** The Nuttio serpentinite belt, central Lapland; an example of Paleoproterozoic ophiolitic mantle rocks in Finland. Ofioliti 22 (1, Special Issue), 35–46.
- Hanski, E., Huhma, H. & Vaasjoki, M. 2001.** Geochronology of northern Finland; a summary and discussion. In: Vaasjoki, M. (ed.) Radiometric age determinations from Finnish Lapland and their bearing on the timing of Precambrian volcano-sedimentary sequences. Geological Survey of Finland, Special Paper 33, 255–279.
- Hanski, E. & Huhma, H. 2005.** Central Lapland greenstone belt. In: Lehtinen, M., Nurmi, P. A. & Rämö, O. T. (eds) Precambrian Geology of Finland – Key to the Evolution of the Fennoscandian Shield. Developments in Precambrian Geology 14. Amsterdam: Elsevier, 139–194.
- Hautaniemi, H., Kurimo, M., Multala, J., Leväniemi, H. & Vironmäki, J. 2005.** The “Three In One” aerogeophysical concept of GTK in 2004. In: Airo, M.-L. (ed.) Aerogeophysics in Finland 1972-2004: Methods, System Characteristics and Applications. Geological Survey of Finland, Special Paper 39, 21-74.
- Heilimo, E., Halla, J., Lauri, L. S., Rämö, T., Huhma, H., Kurhila, M. I., & Front, K. 2009.** The Paleoproterozoic Nattanen-type granites in northern Finland and vicinity: A postcollisional oxidized A-type suite. Bulletin of the Geological Society of Finland 81, 7-38.
- Heinonen, S., Malinowski, M., Hlousek, F., Gislason, G., Buske, S., Koivisto, E. and Wojdyla, M. 2019.** Cost-effective seismic exploration: 2D reflection profiling at the Kylahti massive sulfide deposit, Finland. Minerals, 9, 263, <https://doi.org/10.3390/min9050263>
- Hlousek, F., Hellwig, O., Buske, S. 2015.** Improved structural characterization of the Earth's Crust at the German Continental Deep Drilling Site (KTB) using advanced seismic imaging techniques. Journal of Geophysical Research (Solid Earth), 10.1002/2015JB012330.

- Hölttä, P., Väisänen, M., Väänänen, J. & Manninen, T. 2007.** Paleoproterozoic metamorphism and deformation in central Lapland, Finland. In: Ojala, V. J. (ed.) Gold in the Central Lapland Greenstone Belt. Geological Survey of Finland, Special Paper 44, 7–56.
- Hornby, P., Boschetti, F., Horowitz, F.G. 1999.** Analysis of potential field data in the wavelet domain. *Geophysical Journal International* 137, 175–196.
- Hronsky, J.M.A., Groves, D.I. 2008.** Science of targeting: definition, strategies, targeting and performance measurement. *Australian Journal Earth Sciences* 55, 3–12.
- Huhma, H., Hanski, E., Kontinen, A., Vuollo, J., Mänttari, I. & Lahaye, J. 2018.** Sm-Nd and U-Pb isotope geochemistry of the Palaeoproterozoic mafic magmatism in eastern and northern Finland. Geological Survey of Finland, Bulletin 405, 150 p.
- Hyvönen, E., Airo, M.-L., Arkimaa, H., Lerssi, J., Loukola-Ruskeeniemi, K., Vanne, J., Vuoriainen, S. 2013.** Airborne geophysical, petrophysical and geochemical characteristics of Palaeoproterozoic black shale units in Finland: applications for exploration and environmental studies. In: Hölttä, P. (Ed.), Current Research: GTK Mineral Potential Workshop, Kuopio, May 2012. Geological Survey of Finland Report of Investigation 198, 59–61.
- Knox-Robinson, C.M., Wyborn, L.A.I. 1997.** Towards a holistic exploration strategy: using geographic information systems as tool to enhance exploration. *Australian Journal Earth Sciences* 44, 453–463.
- Kohonen, T. 2001.** Self-Organizing Maps. Springer-Verlag.
- Korhonen, J. V., Säävuori, H., Wennerström, M., Kivekäs, L., Hongisto, H. & Lähde, S. 1992.** One hundred seventy eight thousand petrophysical parameter determinations from the regional petrophysical programme. In: Autio, S. (ed.) Geological Survey of Finland Current Research 1991-1992. Geological Survey of Finland, Special Paper 18, 137-141.
- Korkiakoski, E. 1992.** Geology and geochemistry of the metakomatiite hosted Pahtavaara gold deposit in Sodankylä, northern Finland, with emphasis on hydrothermal alteration. Geological Survey of Finland, Bulletin 360, 96 p.
- Kreuzer, O.P., Miller, A.V.M., Peters, J., Payne, C., Wildman, C., Partington, G.A., Puccioni, E., McMahon, M.E., Ethridge, M.A. 2015.** Comparing prospectivity modelling results and past exploration data: a case study of porphyry Cu–Au mineral systems in the Macquarie Arc, Lachlan Fold Belt, New South Wales. *Ore Geology Reviews* 71, 516–544.
- Lahtinen, R., Huhma, H., Lahaye, Y., Jonsson, E., Manninen, T., Lauri, L. S., Bergman, S., Hellström, F., Niiranen, T., Nironen, M. 2015.** New geochronological and Sm-Nd constraints across the Pajala shear zone of northern Fennoscandia: Reactivation of a Paleoproterozoic suture. *Precambrian Research* 256, 102-119.
- Lahtinen, R., Huhma, H., Sayab, M., Lauri, L. S. & Hölttä, P. 2018.** Age and structural constraints on the tectonic evolution of the Paleoproterozoic Central Lapland Granitoid Complex in the Fennoscandian Shield. *Tectonophysics* 745, 305–325.
- Lehtonen, M., Airo, M.-L., Eilu, P., Hanski, E., Kortelainen, V., Lanne, E., Manninen, T., Rastas, P., Räsänen, J. & Virransalo, P. 1998.** The stratigraphy, petrology and geochemistry of the Kittilä greenstone area, northern Finland. A report of the Lapland Volcanite Project. Geological Survey of Finland, Report of Investigation 140. 144 p. (in Finnish).
- Leshner C. M., Keays R.R. 2002.** Komatiite-associated Ni-Cu-(PGE) deposits: geology, mineralogy, geochemistry and genesis. In: Cabri L. J. (ed) The geology, geochemistry, mineralogy and mineral beneficiation of platinum-group elements. Canadian Institute of Mining and Metallurgy CIM Special Volume 54, 579–619.
- Leväniemi, H., Melamies, M., Mertanen, M., Heinonen, S. & Karinen, T. 2018.** Petrophysical measurements to support interpretation of geophysical data in Sodankylä, northern Finland. Geological Survey of Finland, Open File Work Report 25/2018. 7 p.

- Li, Y. & Oldenburg, D. 1996.** 3D inversion of magnetic data. *Geophysics*, 61, 394-408.
- Li, Y. & Oldenburg, D. 1998.** 3D inversion of gravity data. *Geophysics*, 63, 109-119.
- MacLeod, I. N. & Ellis, R. G. 2013.** Magnetic Vector Inversion, a simple approach to the challenge of varying direction of rock magnetization. ASEG-PESA, 23rd International Geophysical Conference and Exhibition, 11-14 August 2013, Melbourne, Australia.
- Manninen, T., Pihlaja, P. & Huhma, H. 2001.** U-Pb geochronology of the Peurasuvanto area, northern Finland. Radiometric age determinations from Finnish Lapland and their bearing on timing of Precambrian volcano-sedimentary sequences. Geological Survey of Finland, Special Paper 33, 189-200.
- McCuaig, T. C., Kerrich, R. 1998.** P-T-t-deformation-fluid characteristics of lode gold deposits: evidence from alteration systematics. *Ore Geology Reviews* 12, 381-453.
- McCuaig, T. C., Beresford, S., Hronsky, J. 2010.** Translating the mineral systems approach into an effective exploration targeting system. *Ore Geology Reviews* 38, 128-138.
- Mineral Deposit and Exploration –service** [Electronic resource]. Espoo: Geological Survey of Finland [referred 18.05.2020]. (<http://gtkdata.gtk.fi/MDaE/index.html>).
- Montonen, M., 2012.** Indusoitunut ja pysyvä magnetoituma kahdessa Kevitsan intruusion lävistävässä kairareissä. Unpub. M.Sc. Thesis, University of Helsinki. (In Finnish, with an English abstract).
- Mutanen, T. 1976.** Koitelaisen malmitutkimukset 1975. Geological Survey of Finland, unpublished report M19/3741/-76/1/10. 45 p. + 10 appendices. (In Finnish).
- Mutanen, T. 1979.** Vanadiini- ja kromi-platinamalmitutkimukset Koitelaisenvosien alueella Sodankylässä vuosina 1973-1978. Geological Survey of Finland, unpublished report M19/3741/1-79/1/10. 130 p. + 9 appendices. (In Finnish).
- Mutanen, T. 1989.** Koitelaisen malmitutkimukset vuosina 1979-1989. Geological Survey of Finland, unpublished report M19/37/89/1/10. 81p. + 5 appendices. (In Finnish).
- Mutanen, T. 1997.** Geology and ore petrology of the Akanvaara and Koitelainen mafic layered intrusions and the Keivitsa-Satovaara layered complex, northern Finland. Geological Survey of Finland, Bulletin 395. 233 p.
- Mutanen, T. & Huhma, H. 2001.** U-Pb geochronology of Koitelainen, Akanvaara and Keivitsa. In: Vaasjoki, M. (ed.) Radiometric age determinations from Finnish Lapland and their bearing on the timing of Precambrian volcano-sedimentary sequences. Geological Survey of Finland, Special Paper 33, 229-246.
- Naldrett A.J. 2004.** Magmatic sulfide deposits: geology, geochemistry and exploration. Springer Verlag, Berlin-Heidelberg. 728 p.
- Niiranen, T. 2015.** A 3D structural model of the central and eastern part of the Kittilä terrane, Archive report 90/2015, Geological Survey of Finland, 17 p.
- Niiranen, T., Nykänen V. M., Lahti, I. 2019.** Scalability of the mineral prospectivity modeling - An orogenic gold case study from northern Finland. *Ore Geology Reviews* 109, 11-25.
- Nironen, M. 2005.** Proterozoic orogenic granitoid rocks. In: Lehtinen, M., Nurmi, P. A. & Rämö, O. T. (eds) Precambrian Geology of Finland – Key to the Evolution of the Fennoscandian Shield. *Developments in Precambrian Geology* 14. Amsterdam: Elsevier, 443-480

- Rasilainen, K. & Lahtinen, R. 2007.** The Rock Geochemical Database of Finland Manual. Geological Survey of Finland, Report of Investigation 164. 38 p.
- Rastas, P., Huhma, H., Hanski, E., Lehtonen, M. I., Härkönen, I., Kortelainen, V., Mänttari, I. & Paakkola J. 2001.** U-Pb isotopic studies on the Kittilä Greenstone area, Central Lapland, Finland. In: Vaasjoki, M. (editor). Radiometric age determinations from Finnish Lapland and their bearing on timing of Precambrian volcano-sedimentary sequences. Geological Survey of Finland, Special Paper 33, 95-141.
- Riddarhyttan Resources AB 2001.** Annual report 2001, 51
http://tupa.gtk.fi/karttasovellus/mdae/references/386_Suurikuusikko/102113.pdf
- Rupert Resources Ltd. 2018.** NI 43-101 Technical Report: Pahtavaara Project, Finland. 212 p.
- Salminen, R. (Ed.), 1995.** Finnish with summary in English. Geological Survey of Finland, Report of Investigation 130. 47 p.
- Santaguida, F., Luolavirta, K., Lappalainen, M., Ylinen, J., Voipio, T., Jones, S. 2015.** The Kevitsa Ni-Cu-PGE deposit in the Central Lapland greenstone belt in Finland. In: Maier, W., O'Brien, H., Lahtinen, R. (eds.), Mineral deposits of Finland. Elsevier, Amsterdam, 195–210.
- Sayab, M., Molnár, F., Aerden, D., Niiranen, T., Kuva, J. & Välimaa, J. 2019.** A succession of near-orthogonal horizontal tectonic shortenings in the Paleoproterozoic Central Lapland Greenstone Belt of Fennoscandia: constraints from the world-class Suurikuusikko gold deposit. *Mineralium Deposita* <https://doi.org/10.1007/s00126-019-00910-7>
- Stephen J. Barnes, S.J., Fiorentini, M.L. 2012.** Komatiite Magmas and Sulfide Nickel Deposits: A Comparison of Variably Endowed Archean Terranes. *Economic Geology* 107, 755-780.
- Tsoukalas, L.H., Uhrig, R.E. 1997.** Fuzzy and Neural Approaches in Engineering. John Wiley & Sons, New York, p. 606.
- UBC-GIF 2005.** Grav3D Version 3.0. A Program Library for Forward Modelling and Inversion of Gravity Data over 3D Structures. UBC-Geophysical Inversion Facility, Department of Earth and Ocean Sciences, University of British Columbia, Vancouver, British Columbia, May 2005.
- Väisänen, M. 2002.** Structural features in the central Lapland greenstone belt, northern Finland. Geological Survey of Finland, archive report K 21.42/2002/3. 20 p., 16 apps.
- Vuollo, J. & Huhma, H. 2005.** Paleoproterozoic mafic dikes in NE Finland. In: Lehtinen, M., Nurmi, P. A. & Rämö, O. T. (eds) Precambrian Geology of Finland – Key to the Evolution of the Fennoscandian Shield. *Developments in Precambrian Geology* 14. Amsterdam: Elsevier, 195–236.
- Ward, P., Härkönen, I., Nurmi, P. & Pankka, H. S. 1989.** Structural studies in the Lapland Greenstone belt, northern Finland and their application to gold mineralization. In: Autio, S. (ed.) Current Research, Geological Survey of Finland, Special Paper 10, 71-77.
- Williams, N. C. 2006.** Applying UBC-GIF potential field inversions in greenfields or brownfields exploration. Australian Earth Sciences Convention, ASEG/GSA, Abstracts, 2006, Melbourne, Australia.
- Williams, N. C. 2008.** Geologically-controlled UBC-GIF gravity and magnetic inversions with examples from the Agnew-Wiluna greenstone belt, Western Australia. Unpub. Ph.D. Thesis, The University of British Columbia.
- Wyche, N. L., Eilu, P., Koppström, K., Kortelainen, V. J., Niiranen, T & Välimaa, J. 2015.** The Suurikuusikko gold deposit (Kittilä Mine), northern Finland. In: Maier, W., O'Brien, H., Lahtinen, R. (eds.), Mineral Deposits of Finland. Elsevier, Amsterdam, 411–433.